

Jordan Journal of Mechanical and Industrial Engineering (JJMIE)

JJMIE is a high-quality scientific journal devoted to fields of Mechanical and Industrial Engineering. It is published by Hashemite University in corporation with the Jordanian Scientific Research Support Fund.

EDITORIAL BOARD

Editor-in-Chief

Prof. Ahmed M. Al-Ghandoor

Editorial board

Prof. **Mohammad Ahmad Hamdan**
University of Jordan

Prof. **Naseem Sawaqed**
Mutah University

Prof. **Amin Al Robaidi**
Al Balqa Applied University

Prof. **Naser Al-Huniti**
University of Jordan

Prof. **Mohammad Hayajneh**
Jordan University of Science and Technology

Prof. **Suhil Kiwan**
Jordan University of Science and Technology

THE INTERNATIONAL ADVISORY BOARD

Abu-Qudais, Mohammad
Jordan University of Science & Technology, Jordan

Abu-Mulaweh, Hosni
Purdue University at Fort Wayne, USA

Afaneh Abdul-Hafiz
Robert Bosch Corporation, USA

Afonso, Maria Dina
Institute Superior Tecnico, Portugal

Badiru, Adedji B.
The University of Tennessee, USA

Bejan, Adrian
Duke University, USA

Chalhoub, Nabil G.
Wayne State University, USA

Cho, Kyu-Kab
Pusan National University, South Korea

Dincer, Ibrahim
University of Ontario Institute of Technology,
Canada

Douglas, Roy
Queen's University, U. K

El Bassam, Nasir
International Research Center for Renewable
Energy, Germany

Haik, Yousef
United Arab Emirates University, UAE

Jaber, Jamal
Al- Balqa Applied University, Jordan

Jubran, Bassam
Ryerson University, Canada

Kakac, Sadik
University of Miami, USA

Khalil, Essam-Eddin
Cairo University, Egypt

Mutoh, Yoshiharu
Nagaoka University of Technology, Japan

Pant, Durbin
Iowa State University, USA

Riffat, Saffa
The University of Nottingham, U. K

Saghir, Ziad
Ryerson University, Canada

Sarkar, MD. Abdur Rashid
Bangladesh University of Engineering &
Technology, Bangladesh

Signer, Dennis
Wichita State University, USA

Sopian, Kamaruzzaman
University Kebangsaan Malaysia, Malaysia

Tzou, Gow-Yi
Yung-Ta Institute of Technology and Commerce,
Taiwan

EDITORIAL BOARD SUPPORT TEAM

Language Editor

Dr. Qusai Al-Debyan

Publishing Layout

Eng. Ali Abu Salimeh

SUBMISSION ADDRESS:

Prof. Ahmed Al-Ghandoor, Editor-in-Chief
Jordan Journal of Mechanical & Industrial Engineering,
Hashemite University,
PO Box 330127, Zarqa, 13133 , Jordan
E-mail: jjmie@hu.edu.jo



Hashemite Kingdom of Jordan



Hashemite University

Jordan Journal of
Mechanical and Industrial Engineering

JJMIE

An International Peer-Reviewed Scientific Journal
Financed by Scientific Research Support Fund

<http://jjmie.hu.edu.jo/>

ISSN 1995-6665

Jordan Journal of Mechanical and Industrial Engineering (JJMIE)

JJMIE is a high-quality scientific journal devoted to fields of Mechanical and Industrial Engineering. It is published by The Jordanian Ministry of Higher Education and Scientific Research in corporation with Hashemite University.

Introduction: The Editorial Board is very committed to build the Journal as one of the leading international journals in mechanical and industrial engineering sciences in the next few years. With the support of the Ministry of Higher Education and Scientific Research and Jordanian Universities, it is expected that a heavy resource to be channeled into the Journal to establish its international reputation. The Journal's reputation will be enhanced from arrangements with several organizers of international conferences in publishing selected best papers of the conference proceedings.

Aims and Scope: *Jordan Journal of Mechanical and Industrial Engineering* (JJMIE) is a refereed international journal to be of interest and use to all those concerned with research in various fields of, or closely related to, mechanical and industrial engineering disciplines. *Jordan Journal of Mechanical and Industrial Engineering* aims to provide a highly readable and valuable addition to the literature which will serve as an indispensable reference tool for years to come. The coverage of the journal includes all new theoretical and experimental findings in the fields of mechanical and industrial engineering or any closely related fields (Materials, Manufacturing, Management, Design, Thermal and Fluid, Energy, Control, Mechatronics, and Biomedical). The journal also encourages the submission of critical review articles covering advances in recent research of such fields as well as technical notes.

Guide for Authors

Manuscript Submission:

High-quality submissions to this new journal are welcome now and manuscripts may be either submitted online or email.

Online: For online and email submission upload one copy of the full paper including graphics and all figures at the online submission site, accessed via <http://jjmie.hu.edu.jo>. The manuscript must be written in MS Word 2010 Format. All correspondence, including notification of the Editor's decision and requests for revision, takes place by e-mail and via the Author's homepage, removing the need for a hard-copy paper trail.

Submission address and contact:

Prof. Ahmed Al-Ghandoor
Editor-in-Chief
Jordan Journal of Mechanical & Industrial Engineering,
Hashemite University,
PO Box 330127, Zarqa, 13115, Jordan
E-mail: jjmie@hu.edu.jo

Types of contributions: Original research papers and Technical reports

Corresponding author: Clearly indicate who is responsible for correspondence at all stages of refereeing and publication, including post-publication. Ensure that telephone and fax numbers (with country and area code) are provided in addition to the e-mail address and the complete postal address. Full postal addresses must be given for all co-authors.

Original material: Submission of an article implies that the work described has not been published previously (except in the form of an abstract or as part of a published lecture or academic thesis), that it is not under consideration for publication elsewhere, that its publication is approved by all authors and that, if accepted, it will not be published elsewhere in the same form, in English or in any other language, without the written consent of the Publisher. Authors found to be deliberately contravening the submission guidelines on originality and exclusivity shall not be considered for future publication in this journal.

Withdrawing: If the author chooses to withdraw his article after it has been assessed, he shall reimburse JJMIE with the cost of reviewing the paper.

Manuscript Preparation:

General: Editors reserve the right to adjust style to certain standards of uniformity. Original manuscripts are discarded after publication unless the Publisher is asked to return original material after use. Please use MS Word 2010 for the text of your manuscript.

Structure: Follow this order when typing manuscripts: Title, Authors, Authors title, Affiliations, Abstract, Keywords, Introduction, Main text, Conclusions, Acknowledgements, Appendix, References, Figure Captions, Figures and then Tables. Please supply figures imported into the text AND also separately as original graphics files. Collate acknowledgements in a separate section at the end of the article and do not include them on the title page, as a footnote to the title or otherwise.

Text Layout: Use 1.5 line spacing and wide (3 cm) margins. Ensure that each new paragraph is clearly indicated. Present tables and figure legends on separate pages at the end of the manuscript. If possible, consult a recent issue of the journal to become familiar with layout and conventions. All footnotes (except for table and corresponding author footnotes) should be identified with superscript Arabic numbers. To conserve space, authors are requested to mark the less important parts of the paper (such as records of experimental results) for printing in smaller type. For long papers (more than 4000 words) sections which could be deleted without destroying either the sense or the continuity of the paper should be indicated as a guide for the editor. Nomenclature should conform to that most frequently used in the scientific field concerned. Number all pages consecutively; use 12 or 10 pt font size and standard fonts.

Corresponding author: Clearly indicate who is responsible for correspondence at all stages of refereeing and publication, including post-publication. The corresponding author should be identified with an asterisk and footnote. Ensure that telephone and fax numbers (with country and area code) are provided in addition to the e-mail address and the complete postal address. Full postal addresses must be given for all co-authors. Please consult a recent journal paper for style if possible.

Abstract: A self-contained abstract outlining in a single paragraph the aims, scope and conclusions of the paper must be supplied.

Keywords: Immediately after the abstract, provide a maximum of six keywords (avoid, for example, 'and', 'of'). Be sparing with abbreviations: only abbreviations firmly established in the field may be eligible.

Symbols: All Greek letters and unusual symbols should be identified by name in the margin, the first time they are used.

Units: Follow internationally accepted rules and conventions: use the international system of units (SI). If other quantities are mentioned, give their equivalent in SI.

Maths: Number consecutively any equations that have to be displayed separately from the text (if referred to explicitly in the text).

References: All publications cited in the text should be presented in a list of references following the text of the manuscript.

Text: Indicate references by number(s) in square brackets in line with the text. The actual authors can be referred to, but the reference number(s) must always be given.

List: Number the references (numbers in square brackets) in the list in the order in which they appear in the text.

Examples:

Reference to a journal publication:

[1] M.S. Mohsen, B.A. Akash, "Evaluation of domestic solar water heating system in Jordan using analytic hierarchy process". Energy Conversion & Management, Vol. 38 (1997) No. 9, 1815-1822.

Reference to a book:

[2] Strunk Jr W, White EB. The elements of style. 3rd ed. New York: Macmillan; 1979.

Reference to a conference proceeding:

[3] B. Akash, S. Odeh, S. Nijmeh, "Modeling of solar-assisted double-tube evaporator heat pump system under local climate conditions". 5th Jordanian International Mechanical Engineering Conference, Amman, Jordan, 2004.

Reference to a chapter in an edited book:

[4] Mettam GR, Adams LB. How to prepare an electronic version of your article. In: Jones BS, Smith RZ, editors. Introduction to the electronic age, New York: E-Publishing Inc; 1999, p. 281-304

Free Online Color : If, together with your accepted article, you submit usable color and black/white figures then the journal will ensure that these figures will appear in color on the journal website electronic version.

Tables: Tables should be numbered consecutively and given suitable captions and each table should begin on a new page. No vertical rules should be used. Tables should not unnecessarily duplicate results presented elsewhere in the manuscript (for example, in graphs). Footnotes to tables should be typed below the table and should be referred to by superscript lowercase letters.

Notification: Authors will be notified of the acceptance of their paper by the editor. The Publisher will also send a notification of receipt of the paper in production.

Copyright: All authors must sign the Transfer of Copyright agreement before the article can be published. This transfer agreement enables Jordan Journal of Mechanical and Industrial Engineering to protect the copyrighted material for the authors, but does not relinquish the authors' proprietary rights. The copyright transfer covers the exclusive rights to reproduce and distribute the article, including reprints, photographic reproductions, microfilm or any other reproductions of similar nature and translations.

Proof Reading: One set of page proofs in MS Word 2010 format will be sent by e-mail to the corresponding author, to be checked for typesetting/editing. The corrections should be returned within **48 hours**. No changes in, or additions to, the accepted (and subsequently edited) manuscript will be allowed at this stage. Proofreading is solely the author's responsibility. Any queries should be answered in full. Please correct factual errors only, or errors introduced by typesetting. Please note that once your paper has been proofed we publish the identical paper online as in print.

Author Benefits:

No page charges: Publication in this journal is free of charge.

Free offprints: One journal issues of which the article appears will be supplied free of charge to the corresponding author and additional offprint for each co-author. Corresponding authors will be given the choice to buy extra offprints before printing of the article.

PAGES**PAPERS**

1 - 11

Performance Assessment and Theoretical Simulation of Adsorption Refrigeration System Driven by Flat Plate Solar Collector*Raed Al-Rbaihat , Ahmad Sakhrieh, Jamil Al-Asfar , Ali Alahmer , Osama Ayadi , Ahmed Al-Salaymeh , Zayed Al_hamamre , Abeer Al-bawwab , Mohammed Hamdan .*

13 - 19

Surface Hardening by Turning without Chip Formation.*Nikolay Zubkov, Victor Poptsov, Sergey Vasiliev*

21– 26

Optimal Scheduling and Sequencing of Operating Room Under Emergency Cases*Abbas Al-Refaie , Mays Judeh , Ming-Hsien Li*

27– 33

Bits Reduction in the Electrodeposition Process of a Pickup Truck: a Case Study.*A. R. Nabiilah, Z. Hamedon, M. T. Faiz*

35– 40

Numerical and Theoretical Analysis of a Straight Bevel Gear Made from Orthotropic Materials*Haidar Fadhil AL-Qrimli , Ahmed M. Abdelrhman , Karam S. Khiled*

41– 49

Chemical Reaction Effect on Unsteady MHD Flow Past an Impulsively Started Inclined Plate with Variable Temperature and Mass Diffusion in the Presence of Hall Current.*U. S. Rajput , Gaurav Kumar .*

51– 59

Energy Savings in the Jordanian Residential Sector.*Hasan Jarad , “Moh’d Sami” Ashhab*

61– 66

Performance and Effective Method of Experimenting Micromixer Using Finished smooth glasses and Cohesive Tape.*C. T. Lee, C. C. Lee , M. L. Liu*

Performance Assessment and Theoretical Simulation of Adsorption Refrigeration System Driven by Flat Plate Solar Collector

Raed Al-Rbaihat ^a, Ahmad Sakhrieh ^{b,c,*}, Jamil Al-Asfar ^{c,d}, Ali Alahmer ^a, Osama Ayadi ^c, Ahmed Al-Salaymeh ^c, Zayed Al_hamamre ^e, Abeer Al-bawwab ^f, Mohammed Hamdan ^c

^a Department of Mechanical Engineering, Al-Tafila Technical University, P. O. Box 179, 66110 Al-Tafila, Jordan

^b Department of Mechanical and Industrial Engineering, American University of Ras Al Khaimah, 10021 UAE

^c Mechanical Engineering Department, The University of Jordan, Amman 11942, Jordan

^d Department of Mechanical Engineering, Al-Zaytoonah University of Jordan, Amman 11733 Jordan

^e Chemical Engineering Department, The University of Jordan, Amman 11942, Jordan

^f Department of Chemistry, The University of Jordan, Amman 11942, Jordan

Received JUNE, 20, 2016

Accepted OCT, 10, 2016

Abstract

The performance of an 8.0 kW Solar Adsorption Refrigeration System (SARS) under Jordanian climate conditions was evaluated experimentally and theoretically. The solar cooling system under study consists of four subsystems, namely silica gel/water adsorption chiller, solar thermal collector, cooling tower and fan coil unit. The ambient temperature, global solar radiation, relative humidity, wind speed and the temperatures of the solar adsorption system at different locations of experimental setup were measured.

Simulation of the solar adsorption system was carried out using the TRAnsientSYstem Simulation software (TRNSYS). The solar adsorption system is based on adsorption chiller operated by hot water produced by flat plate solar collectors with a total surface area of 41m².

The obtained results revealed chilling power and thermal COP of 4.5 kW and 0.34, respectively when the average chilled water outlet temperature, cooling water inlet temperature, and hot water inlet temperatures were 16.8 °C, 28.1°C and 80.2 °C, respectively.

© 2017 Jordan Journal of Mechanical and Industrial Engineering. All rights reserved

Keywords: Adsorption system, solar, Silica gel/water, COP, TRNSYS simulation.

Nomenclatures			CFC	Chlorofluorocarbons
			F	Fraction of adsorption chiller rated value
			Q _{HW}	Hot water energy kW
			Q _{CHW}	Chilled water energy kW
			Q _{CW}	Cooling water energy kW
			Rated	Adsorption chiller rated value
			DEI	Rated (design) chiller thermal energy input
			DC	Rated (design) chiller chilling capacity
			C _p	Specific heat capacity kJ/kg.k
			COP	Coefficient of performance
			CCHP	Combined cooling heating power
			Q _{Elec}	Total electrical power consumed kW
			Q	Thermal power kW
			V̇	Volume flow rate m ³ /s
			N	Number of data
			COPE	Total coefficient of performance
			u _y	Total uncertainty %
			TRN	TRNSYS simulation value
			Exp	Experimentally determined value
			Time	Time of day Hour
			ABS-PD	Absolute average percent %
Notation	Description	Unit		
THW-in	Temperature of the hot water at the chiller inlet	°C		
TCW-in	Temperature of the cooling water at the chiller inlet	°C		
TCHW-in	Temperature of the chilled water at the chiller inlet	°C		
THW-out	Temperature of the hot water at the chiller outlet	°C		
TCW-out	Temperature of the cooling water at the chiller outlet	°C		
TCHW-out	Temperature of the chilled water at the chiller outlet	°C		
ṁ	Water flow rate	kg/s		
SARS	Solar adsorption refrigeration system			
HMCSR	Hamdi Mango Center for Scientific Research			
TRNSYS	TRAnsientSYstem Simulation software			
HCFC	Hydrchlorofluorocarbon			

* Corresponding author e-mail: ahmad.sakhrieh@aurak.ac.ae

	deviation	
Mod	Model	
Act	Actual	
Pred	Predicted	
$\Delta\Delta t'$	Adapted characteristic equation method	
s', a, e and r	Parameters	
SS_r	Residual sum of squares	
SS_t	Total sum of squares	
R^2	Coefficient of determination	
RMSE	Root mean square error	
$ \bar{e} $	Mean absolute difference	
CV	Coefficient of variation	%
y_i	Predicted value of the model	
\hat{y}_i	Associated measured value	
\bar{y}_1	Dependent variable mean	
Sec	Second	
Min	Minute	
Δ	Difference	
ρ	Density	kg/m ³
Σ	Summation	

1. Introduction

A high percentage of the electricity produced in Jordan is consumed in refrigeration and air-conditioning sector. The availability of solar radiation in phase with the seasonal and hourly cooling load profiles in most of the buildings in Jordan, in addition to the large share of primary energy consumed for air conditioning applications in buildings create a high motivation for the utilization of solar cooling technology for such type of buildings [1]. Renewable energy can be considered an effective solution because it is a clean, environment friendly and inexpensive in the long term [2]. The present study focuses on one of the applications of solar energy, which is using solar energy as a heat source to power Solar Adsorption Refrigeration System (SARS).

A lot of interest has been revolving around the idea of using solar energy as an alternative source of energy at the present time. This is due to the environmental considerations currently arising all around the world [3-5]. Solar energy can be used as the main source to operate SARS, which can be driven by low-potential thermal power. This includes, but is not limited to solar energy, geothermal energy and wasted heat. Moreover, the working fluids of this system are environmentally friendly [6].

The use of the heat operated refrigeration system helps in reducing the environmental problems related to the use of HCFCs and CFCs as refrigerants, which are considered among the main causes for ozone layer depletion. Additionally, they directly contribute to the greenhouse effect [7]. Furthermore, the consumption of primary energy and the emission of greenhouse gases associated with electricity generation from fossil fuels lead to considerable environmental consequences and great economic costs.

Many research studies related to air conditioning by thermal driven solar cooling have been accomplished. Li and Wu [8] constructed a novel micro Combined Cooling, Heating and Power (CCHP) system, based on a two bed silica gel/water adsorption chiller. A comparison between simulation results and experimental data was conducted in order to propose a new model with an improved performance. Zhang *et al.* [9] presented a model of silica

gel/water adsorption chiller powered by solar energy. Matlab-Simulink was used to simulate the operating conditions of the chiller. Rabhi *et al.* [10] carried out a simulation work on a solar adsorption chiller using silica gel as adsorbent and water as adsorbent. Also, the finite volume method was used to solve the system numerically. Effects of the average radius of the silica gel grain ranging from 0.6 mm to 0.9 mm and of the temperature regeneration ranging from 77°C to 107°C were studied. Wang *et al.* [11] showed that a silica gel acts as a key role in adsorption refrigeration systems. It was found out that the silica gel/water adsorption refrigeration system is greatly influenced by the adsorption deterioration. Rezk *et al.* [12] used an empirical lumped analytical simulation model to study an adsorption cooling system with 450 kW two bed silica gel/water adsorption chillers. The results showed that the enhancement in the cooling capacity and System COP increased to reach maximum of 25% and 10%, respectively, upon increasing the fin spacing ratio of 2. Fafous *et al.* [13] theoretically investigated the potential of utilizing a solar cooling system at The University of Jordan in Amman to improve the indoor air quality. They showed that proposed solar collectors of 40-m² areas could offer solar heat for an 8 kW solar air conditioning system. Solar heating (approx. 15–25% solar fraction) and domestic hot water (solar fraction up to 100%) could be also provided, with the solar air conditioning system. Lu *et al.* [14] used micro-porous silica gel–water and compound adsorbent of macro-porous silica gel/LiCl-methanol as working pairs in two adsorption cooling systems. The results indicated that the cooling capacity and COP are 1.0 kW and 0.13 respectively. Ali, *et al.* [15] developed a new adsorption air conditioning system driven by solar energy using silica gel/water adsorption chiller, heat exchanger, rotary desiccant and humidifier.

In Jordan, the application of the concept of solar cooling is not new. The review article of Ayadi *et al.* [16] mentioned three solar cooling systems utilizing concentrating collectors that were applied in Jordan; the first was by Hammad *et al.* who tested a prototype absorption chiller for air-conditioning by coupling the chiller to a prototype flat plate collector with a PTC collector in 1991 [17]; later, in 2000, a prototype PTC with an absorption chiller for refrigeration purpose in desert areas was tested [18]. In 2010, a 146 m² Parabolic trough collector was installed at the Dead sea hotel to supply the required heat for a 13 kW absorption chiller [16].

The first adsorption chiller installed in Jordan was a part of the Aqaba Residence Energy Efficiency (AREE) project funded by the EU-MED-ENEC program; it was installed and launched in June 2009 in a “green home”. The solar cooling project is based on a thermally driven adsorption chiller, integrated in a cooling tower (water cooled system). Heat is supplied to the chiller by evacuated tube collectors. Based on above, and since the adsorption chillers require a lower supply temperature to the generator that can be easily produced by flat plate collector, flat plate solar collectors were used in this study to supply heat to the SARS which was installed at Hamdi Mango center for scientific research HMCSR–University of Jordan in Amman.

2. Theoretical Background

Solar cooling technology can be divided into three main categories: solar thermal cooling, solar electrical cooling and solar combined power and cooling. Thermal energy produced from the solar energy can be used in useful heating and cooling in the solar thermal cooling systems by thermo-physical or thermo-chemical processes. Solar thermal cooling is divided mainly into thermo-mechanical solar cooling and sorption technology [19].

Sorption refrigeration technology can be classified mainly into open sorption cycle and closed sorption cycle [20]. Open sorption cycle is classified into liquid or solid desiccant systems that are used for either humidification or dehumidification. Basically, there are two processes to transfer moisture from one air stream to another in the desiccant systems: desorption or regeneration process and sorption process. Liquid and solid desiccants behave under the same principle and hence their water vapor pressure is a function of moisture content and temperature.

Based on the sorption material, closed sorption cycles are divided mainly into liquid sorption and solid sorption. The liquid sorption refers to the absorption, while the solid sorption refers the adsorption. Absorption involves a liquid or solid sorbent that absorbs refrigerant molecules into its inside and changes either chemically and/or physically throughout the process. The most widely used working pairs in the absorption processes are lithium chloride-water, water-ammonia and lithium bromide-water. Adsorption, on the other hand, refers to a solid sorption process which a solid sorbent attracts refrigerant molecules onto its surface by chemical or physical force and without changing its form in the process [21]. Adsorption refrigeration process is achieved using a combination of adsorbent and adsorbate. Activated carbon-ammonia, activated carbon-methanol, activated carbon-ethanol, silica gel-water and zeolite-water are the most widely used working pairs in the adsorption processes.

The adsorption refrigeration cycle consists of two sorption chambers (Desorber and Adsorber), a condenser and an evaporator, as illustrated in Figure 1. The adsorption cycle achieves a COP ranging between 0.3 to 0.7, depending upon the driving heat temperature, which in turn ranges between 55°C and 90°C. The adsorption chiller cycle consists of the following steps:

- In the desorber chamber, the refrigerant vapor is released by regenerating the solid sorbent which means desorb the refrigerant that cohesive on the surface by sorbent porous through applying the heat that is previously received from the heating source.
- The desorbed refrigerant is cooled and condensed to liquid in the condenser. Rejecting the heat through the cooling water supplied from a cooling tower does this.
- The cold refrigerant is vaporized under low partial pressure and low temperature in the evaporator while the useful cooling is produced.
- The refrigerant vapor then enters to the adsorber chamber from the evaporator and will be absorbed by the solid sorbent.
- The functions of two sorption chambers are reversed by alternating the opening of the butterfly valves and the direction of the heating and cooling refrigerants. In this

way, the chilling refrigerant is obtained continuously. The cycle then repeats.

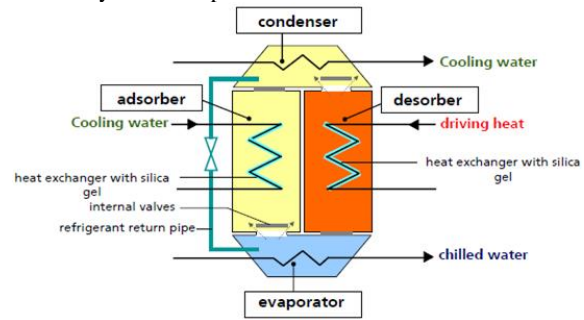


Figure 1. Schematic of adsorption cycle solar cooling system

The adsorption system operates under three temperature levels: high temperature used to supply the heat to the desorber, intermediate temperature used to reject heat in the condenser and adsorber, in addition to low temperature used in producing the coldness. Also there are two pressure levels in this system: high pressure at the condenser and low pressure at the evaporator.

There are many refrigerants that are used in adsorption refrigeration systems. Natural refrigerants include water (the most commonly used one) in addition to Ammonia. However, the most commonly applied refrigerants are methanol, ethanol, ammonia and water.

The thermal power of a chiller (Q) may be calculated from equation 1.

$$\dot{Q} = \dot{m} \cdot C_p \cdot \Delta T = \rho \cdot \dot{V} \cdot C_p \cdot \Delta T \quad (1)$$

where \dot{m} (kg/s) is the mass flow rate of water, ρ (kg/m³) is the density of water, \dot{V} (m³/s) is the volume flow rate of water, C_p (kJ/kg.°C) is the specific heat capacity of water, and ΔT (°C) is the temperature difference of water stream.

The thermal instantaneous COP of the solar adsorption system of the solar adsorption system was calculated according to equation 2:

$$\text{COP} = Q_{\text{CHW}}/Q_{\text{HW}} \quad (2)$$

where COP is the thermal coefficient of performance, Q_{CHW} (kW) is the chilling power, and Q_{HW} (kW) is the heating power.

The total COP (COP_e) of the solar adsorption system is the ratio of the chilling power of the system to the heating power and the total electrical power consumed, Q_{Elec} of the system and was calculated according to equation 3:

$$\text{COP}_e = Q_{\text{CHW}}/(Q_{\text{HW}} + Q_{\text{Elec}}) \quad (3)$$

The instantaneous Solar Fraction Cooling (SFC) of the solar adsorption is the ratio of the total chilling power of the system to the total cooling requirement and was calculated according to equation 4:

$$\text{SFC} = Q_{\text{CHW,Total}}/Q_{\text{L,Total}} \quad (4)$$

where $Q_{\text{CHW,Total}}$ (kW) is the total chilling power of the system and $Q_{\text{L,Total}}$ (kW) is the total cooling requirement.

The absolute average percent deviation (ABS-PD) was also calculated according to equation 4:

$$\text{ABS-PD} = \frac{1}{N_{\text{data}}} \sum_{i=0}^{N_{\text{data}}} \frac{|\text{Pred value} - \text{calculated ac}|}{\text{Exp value}} \cdot 100\% \quad (5)$$

where N is the number of data, predvalue is the predicted value, and expvalue is the experimental value.

The chilling capacity, Q_{CHW} , of the adsorption chiller at the prevailing conditions of inlet hot and cooling water

temperatures, and the heat energy input, Q_{HW} , from hot water storage tank to the adsorption chiller were computed using equations 5 and 6.

$$Q_{CHW} = F_{DC} (Q_{CHWrated}) \quad (5)$$

$$Q_{HW} = F_{DEI} (Q_{HWrated}) \quad (6)$$

where F_{DC} is the design chilling capacity and F_{DEI} is the design energy input of the adsorption chiller model.

3. System Description

Silica gel/water SARS is installed to air condition in two connected laboratories in the ground floor of HMCSR building at The University of Jordan in Amman. HMCSR building consists of a ground floor and a basement with a total floor area of 2040 m².

The required cooling load of the two laboratories is 8 kW (2.27 ton refrigeration). The building envelope has no shading or double glassing [13]. Figure 2 shows the schematic diagram of the solar powered adsorption chiller.

Silica gel/water SARS basically consists of four subsystems, namely silica gel/water adsorption chiller, solar water heating unit, cooling tower and fan coil unit. There are some auxiliary components including; pipes, fittings, valves, pumps, expansion vessels and control unit(s).

An adsorption chiller with a nominal cooling capacity of 8 kW [22] was selected. The chiller has cold water storage tank with a capacity of 2000 L, cooling tower, fan coil unit, and some auxiliary components such as pipes, pumps and control unit(s) that were installed to supply the cold air to the two connected laboratories.

The solar adsorption system includes some components that contribute to the electricity consumption of the system, including; cooling tower, pumps and adsorption chiller. However, adsorption chiller as a thermally driven chiller consumes very low electrical power compared to a conventional vapor compression chiller. The total maximum electrical consumption of the whole system is 1616 W. The maximum electrical consumption of the six pumps, the cooling tower, and the adsorption chiller are 1069 W, 540 W, and 7.0 W, respectively. However, the electrical power consumption of the six pumps in the

whole system (1069 W) is relatively high. This is attributed to the high pressure drop in circulation the thermal fluid inside the pipes of system, adsorption chiller, and collector absorber.

Flat plate solar collectors are the heat source of the system. Collectors are connected with a hot water storage tank through pipes and single speed pump within a closed circuit. The hot water storage tank was also connected with an adsorption chiller through pipes and single speed pump.

The cooling water unit consists of a flat plate heat exchanger and a cooling tower. Additionally, the flat plate heat exchanger was used to reduce the variation of the cooling water inlet temperature. In addition, the cooling tower was used to reduce the cooling water temperature by controlling the airflow rate. The flat plate heat exchanger, the cooling tower and the adsorption chiller were connected together using pipes and two single speed pumps within a closed circuit.

The Cold-water storage tank was connected to an adsorption chiller using pipes and single speed pump within a closed circuit in order to provide an infinitive cooling load to the adsorption chiller. The storage tank was also connected with a fan coil unit through pipes and single speed pump within a closed circuit in order to provide cold air to the two connected laboratories in HMCSR building. Some auxiliary components, including pipes, fittings, valves, expansion vessels and control unit(s) were installed to support the operation of the solar adsorption system.

The water inlet and outlet temperatures were measured by seven PT1000 platinum resistors. The temperatures of the working fluids were obtained under a steady state of operating conditions in which the solar adsorption system was operating under. The hot water, chilled water, and cooling water flow rate were measured using an ultrasonic flowmeter. Global solar radiation, ambient temperature, wet bulb temperature, relative humidity, and wind speed were measured using different sensors. Under these circumstances, data were recorded every two minutes. The technical specifications of sensors used for measuring of the performance of the solar adsorption system are displayed in table 1.

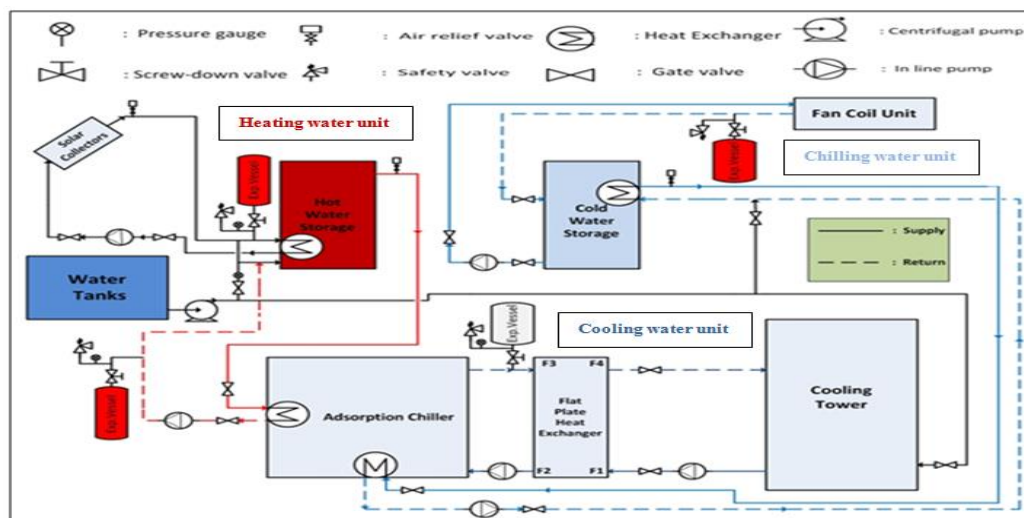


Figure 2. Schematic diagram of the solar powered adsorption chiller

Table 1. Technical specifications of sensors used for measuring of the performance of the solar adsorption system

Sensor type	Model	Specifications	
Flow rate	Ultrasonic flow meter	Flow range	Velocity: 0.1 – 9 m/s (0.3 – 30 ft/s)
		Accuracy	± 2% full scale
		Temperature	Electronics: -28 to 140 °F (-20 to 60 °C) Transducer: -40 to 180 °F (-40 to 82 °C)
Temperature	PT-1000	Accuracy	At 0 °C, 0.3 °C and at 100 °C, 0.8 °C.
Global radiation	SOLRAD – Integrator (SOLRAD radiation indicator - Data logger)	Analogue inputs	1
		AD conversion resolution	1:10.000 bits
		Inaccuracy	< 0.1 %
		Operational temperature range	-10 to 40 °C
		Temperature accuracy, RMS	2 x 16 characters °C
		Power supply	9 Volt battery
		Communication interface	RS-232
	Pyranometer PMA 2144	Response time	18 seconds (95%)
		Sensitivity change/year	< 1%
		Display resolution	1[W/m ²], 0.1[mW/cm ²]
		Operating environment	-40 to 175 °F (-40 to 80 °C), outdoor
		Angular response	2% for angels < 70°
Temperature RH Wet Bulb Wind speed	Datalogging / Printing Anemometer + Psychrometer Model: 451181	Accuracy	Temperature: ±1°F / °C RH: ±3% Wet Bulb: - Wind speed: ±3% rdg
		Range	Temperature: -4 to 144°F / -20 to 60 °C RH: 0 to 100%RH Wet Bulb: -7.6 to 158°F/-22 to 70°C Wind speed: 0.4 to 25 m/s
		Resolution	Temperature:0.1°F/°C RH:0.1% Wet Bulb: 0.1°C Wind speed: 0.1 m/s

4. Simulation

A TRNSYS simulation studio environment project was used to theoretically predict the performance of the whole solar adsorption system as shown in Figure 3. The black solid lines show the flow of system energy information. On the other hand, yellow solid lines show the flow of weather data information, while the green solid lines show the flow of the output information and the brown dotted lines show the flow of control strategy information.

The main components in the TRNSYS simulation

project are: Type 4a – Hot water storage tank, Type 3b – Pump, Type 73 – Theoretical flat plat solar, Type 51b – Wet cooling tower and Type 107 – Absorption chiller that were used to predict the thermal performance of the whole solar adsorption system for different periods of the year. However, an inbuilt Type 107 was used as an adsorption chiller component. A more detailed control strategy was used in this case to replicate the real operation of the solar adsorption system.

A summary of the characteristics and key inputs for the different TRNSYS components used in the simulation of solar adsorption system are listed in table 2.

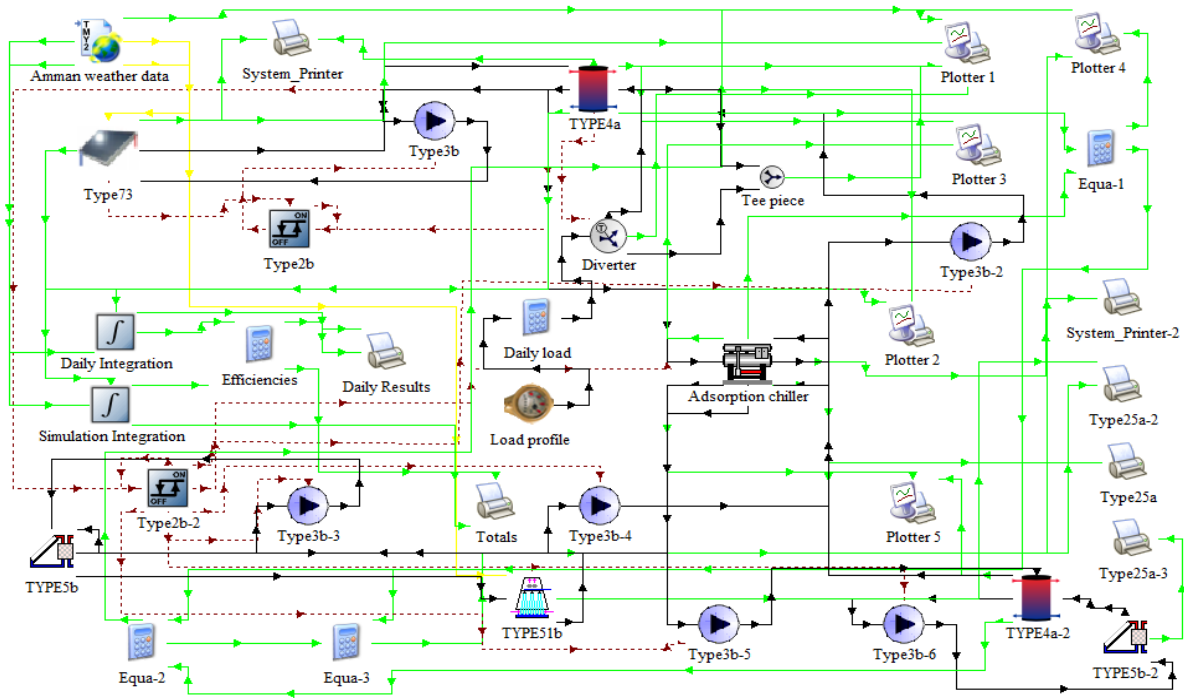


Figure 3. TRNSYS project for simulation of the solar adsorption system

Table 2. Parameters and key inputs of TRNSYS model

TRNSYS type	Key input	Value	Unit
Type 4a – Hot water storage tank	Fluid specific heat	4.19	kJ/kg.k
	Fluid density	1000	kg/m ³
	Loss coefficient	1.0	kJ/hr.m ² .k
	Tank volume	2000	Liters
	Number of temperature levels (Nodes)	8	-
Type 3b – pump:(1,2), (3) and (4)	Maximum flow	(1600), (3700) and (2000)	kg/hr
	Maximum power	882	kJ/hr
	Conversion coefficient	0.0	-
	Fluid specific heat	4.19	kJ/kg.k
	Power coefficient	0.5	-
	Number in series	8	-
Type 73 – Theoretical flat plat solar collector	Fluid specific heat	4.19	kJ/kg.k
	Incidence angle	45	degrees
	Collector area	59.064	m ²
	Rated COP	0.60	-
Type 107 – Modified Adsorption chiller	Rated chilling capacity	28800	kJ/hr
	Fluid specific heat capacity	4.19	kJ/kg.k
	Chiller on and off signal	1 or 0	-
	Auxiliary electrical power	25.2	kJ/hr
	Number of temperature levels (Nodes)	1	-
Type 4a – Cold water storage tank	Fluid specific heat	4.19	kJ/kg.k
	Fluid density	1000	kg/m ³
	Loss coefficient	1	kJ/hr.m ² .k
	Tank volume	2000	Liters
	Number of temperature levels (Nodes)	1	-
Type 51b – Wet cooling tower	Fan maximum power	1836	kJ/hr
	Maximum air flow rate	81.60	m ³ /hr
	Number of tower cells	1	-
	Mass transfer coefficient	2.3	-
	Mass transfer exponent	-0.72	-
Type 5b – Heat exchanger	Specific heat of hot side fluid	4.19	kJ/kg.k
	Specific heat of cod side fluid	4.19	kJ/kg.k

5. Experimental Setup

Experimental results and measurements of system performance were carried out during the months of May and June at the University of Jordan. Eight different days were selected to study the performance of the solar adsorption system. Clear sky and partly cloudy are the prevalent weather conditions at the location of the experimental setup. Figure 4 shows the solar adsorption system that was installed at HMCSR. The hot water, the chilled water and the cooling water systems were adopted as three water supply systems of solar adsorption system. Different sensors were installed in each water supply system. The baseline parameters of the solar adsorption system in -different locations of experimental setup are given in Table 3. It can be seen that the functions of two sorption chambers are reversed by alternating the opening

of the butterfly valves and the direction of the heating and cooling refrigerants through increasing temperature in one sorption chamber and decreasing temperature in the other sorption chamber at the same time.



Figure 4. Solar adsorption system

Table 3. Measured data of the solar adsorption system

Time [min]	G.S.R [W/m ²]	R.H [%]	Wind [m/s]	T amb [°C]	T A OUT [°C]	T D OUT [°C]	T LT IN [°C]	T LT OUT [°C]	T MT OUT [°C]	T LT Ext [°C]	T HT Ext [°C]	T1 OUT [°C]	dQ LT [kW]
00:00	1051	19.0	0.6	31.7	37.3	80.2	23.7	20.8	36.9	23.5	80.0	96	4.3
02:00	1046	19.3	0.9	31.1	33.2	80.9	23.6	20.7	32.8	23.4	80.1	96	4.3
04:00	1049	19.2	0.5	31.5	29.6	82.1	23.6	21.5	30.1	23.3	80.1	96	4.3
06:00	1053	19.8	0.6	31.4	61.7	58.3	23.6	20.8	38.1	23.3	80.0	96	4.2
08:00	1048	19.9	0.4	31.2	80.9	36.3	23.4	21.2	36.2	23.3	79.7	96	4.2
10:00	1060	20.7	0.6	30.9	83.3	31.5	23.4	20.0	31.1	23.1	79.5	96	4.2
12:00	1041	21.1	0.5	30.8	84.1	28.7	23.3	20.1	29.1	23.1	79.5	96	4.1
14:00	1067	19.9	0.5	31.5	36.6	82.3	23.3	20.1	36.1	23.0	79.5	96	4.1
16:00	1046	20.2	0.6	30.8	33.8	84.6	23.3	20.5	32.9	23.0	79.2	97	4.1
18:00	1051	20.5	0.4	30.6	30.9	87.7	23.2	21.6	30.5	23.0	79.5	97	4.1
20:00	1062	21.4	0.5	30.7	61.5	51.3	23.2	21.2	33.0	22.9	79.9	97	4.5
22:00	1090	20.6	1.1	30.3	85.8	37.0	23.1	20.7	36.6	22.7	80.2	98	4.5
24:00	1039	19.5	0.8	30.6	88.3	32.4	23.0	21.6	31.2	22.7	80.4	98	4.5
26:00	1061	20.3	0.8	31.2	51.3	62.1	23.0	21.7	38.0	22.6	80.6	98	4.1
28:00	1047	19.3	0.5	31.3	35.1	83.0	22.8	20.6	34.9	22.5	80.8	98	4.1
30:00	1087	18.8	2.1	31.0	32.3	83.9	22.7	20.9	31.9	22.5	81.0	98	4.1
G.S.R: Global solar radiation [W/m ²] R.H: Relative humidity [%] T amb: Ambient temperature [°C] T A OUT: Temperature of the adsorber chamber at the adsorption chiller [°C]				T D OUT: Temperature of the desorber chamber at the adsorption chiller [°C] T LT IN: Temperature of the chilled water at the chiller inlet [°C] T LT OUT: Temperature of the chilled water at the chiller outlet [°C] T MT OUT: Temperature of the cooling water at the chiller outlet [°C]				T LT Ext: Water temperature of the cold water storage tank [°C] T HT Ext: Water temperature of the hot water storage tank [°C] T1: Collectors outlet temperature [°C] dQ LT: Chilling capacity [kW]					

5.1. Uncertainties Measurement

The variable y is measured indirectly by measuring the independent variables, $x_1, x_2, x_3, \dots, x_m$, where y is a function of independent variables as $y = f(x_1, x_2, x_3, \dots, x_m)$. The uncertainties $u_1, u_2, u_3, \dots, u_m$ in $x_1, x_2, x_3, \dots, x_m$, respectively, are used to give the total uncertainty in y, u_y according to equation 7.

$$u_y = \sqrt{\sum_{j=1}^m \left(\frac{\partial y}{\partial x_j}\right)^2 u_j} \quad (7)$$

Equation 1 and equation 7 are used to give the relative uncertainty in the instantaneous thermal power, Q, measured according to equation 8. The sum of the uncertainties in the instantaneous powers was calculated to give the total uncertainty [23]:

$$\frac{u_Q}{Q} = \sqrt{\left(\frac{u_p}{\rho}\right)^2 + \left(\frac{u_v}{V}\right)^2 + \left(\frac{u_{Cp}}{C_p}\right)^2 + \frac{u_{T_1}^2 + u_{T_2}^2}{(T_2 - T_1)^2}} \quad (8)$$

where $u_Q, u_p, u_v, u_{Cp}, u_{T_1}$ and u_{T_2} are the uncertainties in the thermal power measured, water density, volume flow rate, water specific heat, lower and upper temperatures of the water, respectively.

Figure 5 shows the results of measurements of the thermal power measured. The figure contains error bars indicating the extents of uncertainties. It is observed that the measurements of chilling power, heating power and cooling power have high values of uncertainty at an average between 5.3% and 9.1%.

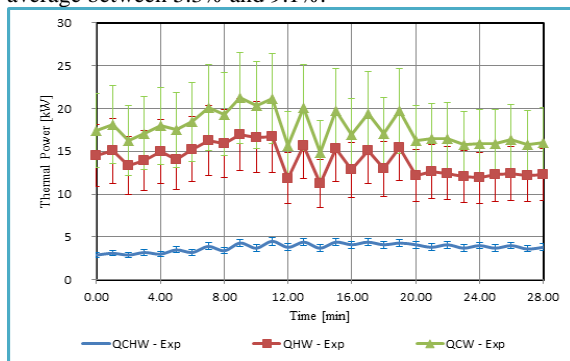


Figure 5. Chiller thermal powers and measurement uncertainties

6. Results and Analysis

Theoretical simulation was basically carried out using TRNSYS simulation software. Figure 6 shows the predicted thermal power of the flat plate solar collectors with respect to the collector slopes on May 20th.



Figure 6. Collector thermal gain for different collector tilts (Simulations on May 20th)

Figure 7 displays the different values of the total thermal power collected at different collector tilts during the months of May and June. From Figure 5, it is evident that the 15° collector slope performs better than all the other collector tilts on 20th, May. Precisely, the optimum tilt angle during this period is observed from Figure 7 to be 15°. However, it is also clear that the difference in the total thermal power collected between the tilts of 0.0° to 35° is very minute, and therefore, any convenient tilt with in this range gives an adequate performance during this period.

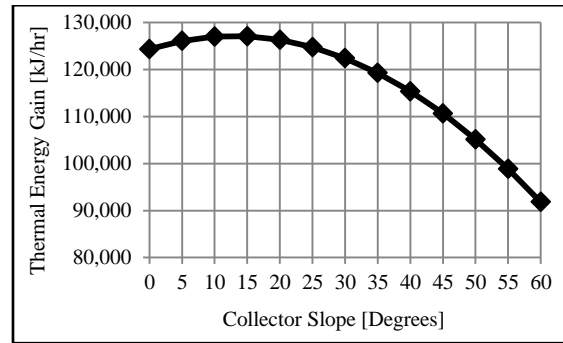


Figure 7. Thermal power gain for more different collector tilts

The simulation model was validated for further simulation campaigns aiming at defining the best operating points of the solar adsorption system and tracing a path towards the plant performance improvement.

Operating temperatures of heating, cooling and chilled water influence the chiller performance. The flow rate of heated, cooled and chilled water is also one of the operating parameters that influence the chiller performance. Therefore the effect of operating conditions on the performance of simulated chiller is important to determine the conditions that can increase the output of the chiller. The chiller performance at the design operating conditions will be used as the baseline for comparison and these listed in Table 4.

Table 4. Adsorption chiller reference operating conditions at design operation

Operating Condition	Value	Unit
Heating water inlet temperature	80	°C
Cooling water inlet temperature	27	°C
Chilled water inlet temperature	18	°C
Heating water flow rate	1531.5	l/h
Cooling water flow rate	3475.5	l/h
Chilled water flow rate	1896.1	l/h

Figure 8 compares the predicted heated, cooled and chilled water outlet temperatures and their actual analogous values, which were supplied by the manufacturer based on the same average inlet conditions. Table 5 presents the absolute average percent deviation (ABS-PD) for heated, cooled and chilled water outlet temperatures for the test results shown in Figure 8. The deviation between the predicted COP, heating power and chilling capacity are also presented. It is known that the predicted values of thermal simulation models can be accepted if the ABS-PD is below 30% [21]. Table 5 and Figure 8 indicate clearly the good agreement between the model and experimental results.

Table 5. Simulation model deviation analysis ($\dot{m}_{HW} = 1600$ l/h, $\dot{m}_{CW} = 3700$ l/h, $\dot{m}_{CHW} = 2000$ l/h)

Term	ABS-PD [%]	Term	ABS-PD [%]
T_{HWout}	2.8	Q_{HW}	11.5
T_{CWout}	3.9	Q_{CHW}	14.8
T_{CHWout}	17.4	COP	3.7

Table 6 presents the ABS-PD for average heating, cooling and chilled water outlet temperature in addition to heating power, chilling capacity and COP for different experimental runs. It can be seen that the maximum absolute percent deviation calculated based on steady state cycle is 19.3%.

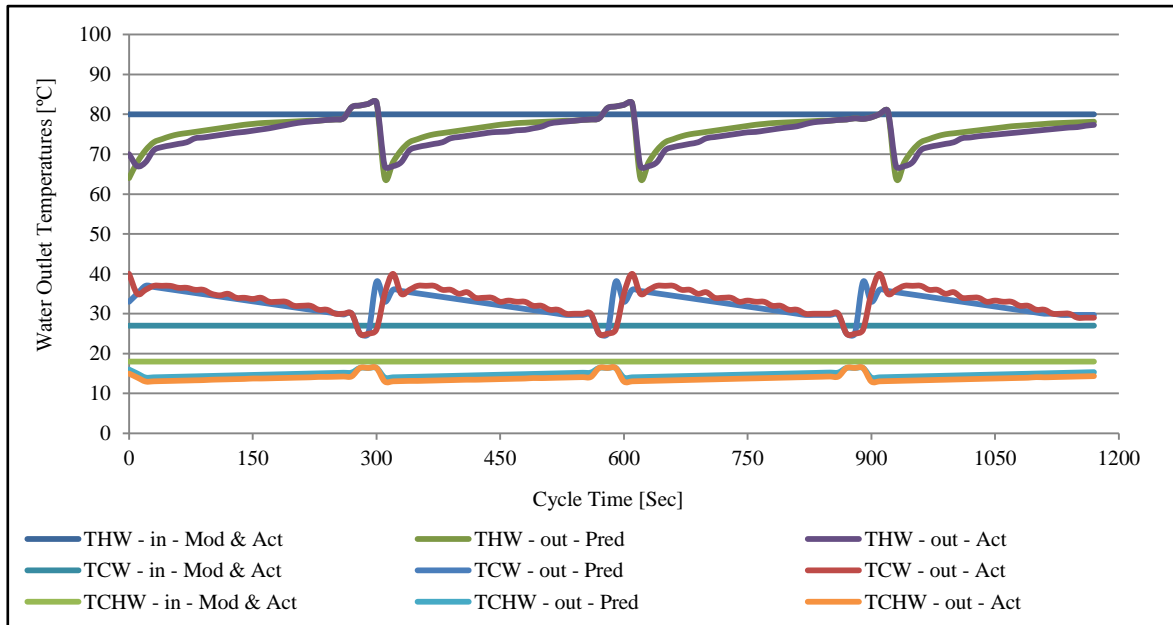


Figure 8. Comparison between predicted data and actual data

Table 6. Simulation model deviation analysis at one steady state cycle

Term	RUN-1	RUN-2	RUN-3	RUN-4	Unit				
\dot{m}_{HW}	1531.5	1531.5	1531.5	1531.5	l/h				
\dot{m}_{CW}	3475.5	3475.5	3475.5	3475.5	l/h				
\dot{m}_{CHW}	1896.1	1896.1	1896.1	1896.1	l/h				
$T_{HWin,avg}$	80.5	79.8	80.2	80.3	°C				
$T_{CWin,avg}$	27.5	27.4	27.2	27.6	°C				
$T_{CHWin,avg}$	18.1	18.1	18.1	18.2	°C				
Deviation analysis (actual temperature & ABS-PD)									
T_{HWout}	74	1.1	73	1.9	73.2	1.4	73.8	1.7	°C & %
T_{CWout}	32.3	0.8	32.1	1.2	31.9	1.1	32.4	0.5	°C & %
T_{CHWout}	16.4	13.7	16.3	13.4	16.2	12.7	16.5	14.1	°C & %
Q_{HW}	12	11.1	12.7	11.4	13.1	11.5	12	10.9	°C & %
Q_{CHW}	4	15.1	4.2	15.8	4.5	19.3	4	15.3	°C & %
COP	0.33	4.1	0.33	4.3	0.34	8.1	0.33	4.2	°C & %

Cooling and heating water inlet temperature influences adsorption chiller performance. Decreasing cooling water inlet temperature not only increases chilling capacity, but also enhances the COP adsorption chiller, due to the significant increase in adsorption rate. Increasing heating water temperature also enhances chiller chilling capacity due to enhance desorption rate. However, it negatively influences the chiller COP depending on the cooling water inlet temperature. As a result, the generation temperature lift, defined as the difference between heating and cooling water inlet temperatures, was calculated and used in the investigation. It is noteworthy to mention that the chilled water inlet temperature depends mainly on the application and hence it was kept constant at its design value.

Figure 9 shows the change in chiller chilling capacity versus generation temperature lift at various cooling water inlet temperatures. Other operating conditions, such as cycle time and secondary fluid flow rate, remained constant at their design values. As the generation temperature lift increases the chiller chilling capacity increases for all cooling water inlet temperatures. In Figure 8, the experimental results at the operating conditions as shown in Table 6 are presented with good agreement with the model.

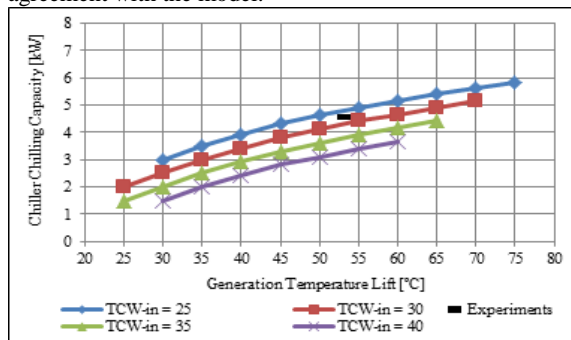


Figure 9. Generation temperature lift influence on chiller performance

Figure 10 depicts the variation in the chiller COP with generation temperature lift. It is observed that at low cooling water temperature, the chiller COP decreased with increasing the generation temperature lift within the tested range. However, at a higher temperature for cooling water (TCW>30°C), the chiller' COP initially increased to a certain point and then remained relatively constant with the increase in the generation temperature lift. The decrease in chiller COP at low generation temperature lift and high cooling water temperature is due to the insufficient refrigerant circulation required to generate the cooling power. On the other hand, the decrease in chiller COP at high temperature lift is due to the increase in heat losses.

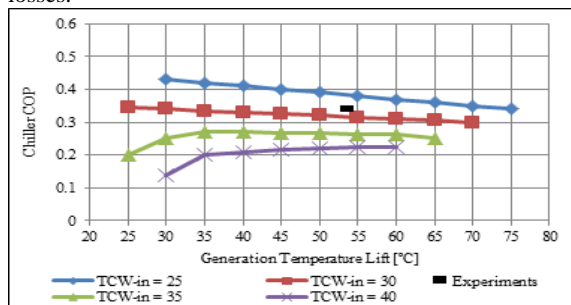


Figure 10. The influence of generation temperature lift on chiller COP

The variation of chiller COP with the generation temperature lift can be used as a load control tool. For example, at cooling water temperature of 35°C, the chiller chilling capacity increased almost linearly (from 2.9 to 4.4kW) with increasing the generation temperature lift (from 40°C to 65°C). The reduction in chiller COP (from 0.27 to 0.25) is relatively small.

7. Conclusions

In the present work, the performance of solar adsorption system under Jordanian climate conditions was simulated using TRNSYS and simulation results were validated against experimental results. The experimental investigation for an 8.0 kW solar adsorption refrigeration system installed at the roof of Hamdi Mango center at the University of Jordan in Amman shows that the Coefficient of Performance (COP) was in the range from 0.14 to 0.34 which is less than the designed theoretical value of 0.55. The measured parameters include the ambient temperature, global solar radiation, relative humidity, wind speed and the temperatures of the solar adsorption system at different locations. The collected data were carried out during two months, which are May and June, and further measurements were needed to measure the system performance during summer time in July and August in addition to the system performance during the whole year. Also, further investigations for system performance will be carried out for different values of the average chilled water outlet temperature, cooling water inlet temperature, and hot water inlet temperature.

Also, simulation of the solar adsorption system has been carried out using the TRAnSientSystem Simulation software (TRNSYS). All in all, it was found that the actual measurements indicate that a chilling power of solar adsorption system is on the average of 65% lower than the theoretical simulation predictions. This is attributed to a number of key reasons such as; high level of uncertainty in the hot water energy and cooling water energy measurements due to the temperature measuring sensors having a low accuracy, and the difference between theoretical and actual tank loss coefficient. The simulation model was validated for further simulation campaigns aiming at defining the best operating conditions of the solar adsorption system and tracing a path towards the plant performance improvement. The chilling capacity has a maximum absolute percent deviation calculated based on steady state cycle of 19.3%.

In general, it was found that the simulation results under predicts the actual ones. This is attributed to a number of key errors faced throughout the research, such as heat losses in the whole system, water leakage in the cooling tower and solar collectors, and high pressure drop in circulation the thermal fluid inside the pipes of system, adsorption chiller, and collector absorber. Therefore, the measured data for solar cooling system needs to be collected continuously for longer periods and for different hot and cold water temperatures in addition to the reduction of the key errors mentioned above and then the measured data can be compared again with the simulated results to get more agreement results.

Acknowledgements

The authors of this paper would like to thank the deanship of scientific research in The University of Jordan for their support in conducting this research work.

References

- [1] Ayadi. O, Mauro. A, Aprile. M, Motta. M, 2012, Performance assessment for solar heating and cooling system for office building in Italy. *Energy Procedia* Volume30, 2012, Pages 490–494.
- [2] Sembatya M. Performance evaluation of a solar cooling system in UAE - Ras Al Khaimah by both experiment and simulation, M.S. thesis, University of Gävle, Sweden, 2013.
- [3] Chen C. J., Wang R. Z., Xia Z. Z., Kiplagat J. K., Lu Z. S. Study on a compact silica gel-water adsorption chiller without vacuum valves: Design and experimental study. *App. Energy* 2010; 87 (1): 2673-81.
- [4] Ahmad Sakhrieh, Waleed Shreim, Hatem Fakhruideen, Hasan Hasan, Ahmed Al-Salaymeh, Combined Solar-Geothermal Power Generation using Organic Rankine Cycle, *Jordan Journal of Mechanical and Industrial Engineering*, Volume 10 (1), pp. 1-9, 2016.
- [5] Bashar K. Hammad, Shaher M. Rababeh, Mohammad A. Al-Abed and Ahmed M. Al-Ghandoor, Performance Study of On-Grid Thin-Film Photovoltaic Solar Station as a Pilot Project for Architectural Use, *Jordan Journal of Mechanical and Industrial Engineering*, Volume 7 (1), pp 1-9, 2013.
- [6] Al-Ghouti A., Yousef I., Ahmad R., Ghrair A. M., Al-Maaitah A. Characterization of diethyl ether adsorption on activated carbon using a novel adsorption refrigerator. *Chem. Eng. Journal* 2010; 162 (1): 234-41.
- [7] Baiju V., Muraleedharan C. Performance study of a two stage solar adsorption refrigeration system. *Inter. Journal of Eng. Science and Tech.* 2011; 3 (7): 5754-64.
- [8] Li S., Wu J. Y. Theoretical research of a silica gel-water adsorption chiller in a micro combined cooling, heating and power (CCHP) system. *App. Energy* 2009; 86 (6): 958-67.
- [9] Zhang G., Wang D. C., Zhang J. P., Han Y. P., Sun W. Simulation of operating characteristics of the silica gel-water adsorption chiller powered by solar energy. *Sol. Energy* 2011; 85 (7): 1469-78.
- [10] Rabhi K., Ali C., Ben Bacha H. Numerical study of combined heat and mass transfer in the silica gel-water adsorption chiller. *Inter. Review of Mech. Eng.* 2012; 6 (6).
- [11] Wang D., Zhang J., Xia Y., Han Y., Wang S. Investigation of adsorption performance deterioration in silica gel-water adsorption refrigeration. *Energy Conv. and Manag.* 2012; 58: 157-62.
- [12] Rezk A., Al-Dadah R. K., Mahmoud S., Elsayed A. Effects of contact resistance and metal additives in finned-tube adsorbent beds on the performance of silica gel/water adsorption chiller. *App. Thermal Eng.* 2013; 53 (2): 278-84.
- [13] Fafous A., Asfar J., Al-Salaymeh A., Sakhrieh A., Al-hamamre Z., Al-bawwab A., Hamdan M. Potential of utilizing solar cooling in The University of Jordan. *Energy Conv. and Manag.* 2013; 65: 729-35.
- [14] Lu Z., Wang R., Xia Z., Gong L. Experimental investigation adsorption chillers using micro-porous silica gel-water and compound adsorbent-methanol. *Energy Conv. and Manag.* 2013; 65: 430-7.
- [15] Ali C., Rabhi K., Nciri R., Nasri F., Ben Bacha H. New adsorption air conditioning system powered by solar energy; operation principals and winter mode modelling and simulation. *Inter. Review of Mech. Eng.* 2013; 7 (1).
- [16] Ayadi O., Aprile. M, Motta. M. Solar cooling systems utilizing concentrating solar collectors -An overview. *Energy Procedia* 2012; 64(3).
- [17] Hammad M., Audi M. Performance of a solar LiBr-water absorption refrigeration system. *Renewable Energy* 1992; 2(3).
- [18] Hammad M and Habali S. Design and performance study of a solar energy powered vaccine cabinet. *Applied Thermal Engineering* 2000; 20(18).
- [19] Hwang Y., Radermacher R., Al Alili A., Kubo I. Review of solar cooling technologies. *HVAC&R Research* 2008; 14 (3): 507-28.
- [20] Saudagar R. T., Ingole P. R., Mohod T. R., Choube A. M. A review of emerging technologies for solar air conditioner, *International Journal of Innovative Research in Science, Eng. and Tech.* 2013; 2 (6).
- [21] Al-Fafous A. Investigation of the performance of the adsorption solar air conditioning systems under Jordanian climate conditions. M.S. thesis, Department of mechanical Engineering, The University of Jordan, Jordan, 2012.
- [22] Daßler I., Mittelbach W. Solar cooling with adsorption chillers. *Energy Procedia* 2012; 30: 921-9.
- [23] Semyon G. Rabinovich. Evaluating measurement accuracy, a practical approach. 4th ed. Springer, USA; 2010.

Surface Hardening by Turning without Chip Formation

Nikolay Zubkov, Victor Poptsov* and Sergey Vasiliev

Department of Cutting tools and technology, Bauman Moscow State Technical University, 2nd Baumanskaya str. 5, Moscow, Russia 105005

Received MARCH, 14, 2016

Accepted DEC, 16, 2016

Abstract

The present study describes the basic principles, specific features in the implementation and technological capabilities of a new method of quench surface turning without separation of chip. The underlying process of this method is process of Deformational Cutting (DC) which is based on undercutting and deformation of the surface layers that remain on the workpiece. The energy released in the area of deformational cutting is used to heat the undercut layer up to the temperatures of structural and phase changes of the material being processed. As a result of processing, a hardened structure is formed on the surface which consists of inclined, thin undercut layers tightly fitted to each other. Options are available where the undercut layer is fully hardened in its thickness or only partially hardened. Options are presented which show structures generated on steels. Samples hardened by DC method showed a higher wear resistance compared to samples with volumetric hardening.

© 2017 Jordan Journal of Mechanical and Industrial Engineering. All rights reserved

Keywords: *Hardening, composite, wear resistance, deformational cutting.*

1. Introduction

Surface hardening is the most efficient and economical way of increasing wear resistance of machine parts [1]. This is a real challenge for machines and mechanisms operating under high bearing pressure and abrasive wear. Currently, there have been dozens of surface hardening technologies, most of which require specialized thermal equipment to achieve thermo physical impact needed for structural and phase transformations during quenching of steels [2]. A relatively new method of surface hardening is hardening directly on metal-working machines: temperatures required for hardening are reached in the cutting process thanks to plastic deformation and friction in the contact area of tool and workpiece. The combined effect of severe deformation, high local temperatures, and rapid quenching rates causes the machined surface to undergo both physical and metallurgical changes [3].

2. State of Art

2.1. Quench Hardening with the Use of Cutting Process

Quench hardening during mechanical machining can be realized both by using edge tools and abrasive processing. The effect of increasing surface hardness during lathe machining is described in [4]. To [5] enhance friction of workpiece and tool, turning with a zero back clearance angle was used at work. Hardening of surface was observed when cutters with front negative-rake angles [6] were used for turning.

The maximum hardness of the hardened layer generated by machining hardening/grind-hardening is 50...65 HRC while the maximum penetration depth is 2 mm [3, 7].

Quench grinding of steels with a carbon content of more than 0.3% is based on the use of forced grinding modes and has a number of advantages compared to hardening based on quench turning. The thickness of the hardened layer in consideration of the removed defective layer is 0.3...0.5 mm. The heat-affected zone is up to 2 mm, hardness on the part surface is up to 50...60 HRC. Depth of cut when grinding is 0.2...1.2 mm subject to longitudinal feed of the grinding wheel 0.3...1.2 m/m. The presence of cooling liquids is not necessary since cooling is achieved by discharging heat to the underlying workpiece layers [8, 9]. Currently, the process of hardening by grinding gained momentum. DMG/Mori Seiki manufactures CNC milling and grinding machining centers which provide for quenching by using a grinding wheel. The throughput of a processing operation is 0.05...0.21 sec/cm². Once quench grinding is completed, the defective surface layer must be removed [10].

In the present article, an application of Deformational Cutting (DC) technology for surface hardening is presented. The main difference of quenching with the use of DC method from other methods of hardening based on the process of cutting is that chips are not separated from the workpiece and remain on the surface thus forming a special reinforced structure. Further differences include consistency, hardness quenched over its thickness and the possibility of generation of a hardened structure of composite material with alternating hardened and less

* Corresponding author e-mail:

solid (more plastic) layers. Method of turning by hardening without separation of chips is protected by RF patent No. 2556897 [11].

2.2. Method of Deformational Cutting

DC technology was invented by Zoubkov (now Nikolay Zubkov) and Ovtchinnikov [12]. A DC tool cuts and plastically deforms the surface layers of the workpiece forming a finned macrostructure since the cut layers are connected to the workpiece material (Figure 1).

The main difference between the traditional cutting process and DC is that the chips become fins and remain as a functional part of the workpiece.

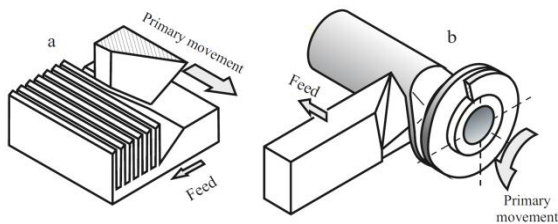


Figure 1. Concept of deformational cutting: shaping of flat surfaces (a), turning of cylindrical surfaces (b)

The DC machining can increase the surface area up to 12 times for copper and up to 6 times for steel. The main limiting factors for DC are workpiece ductility and hardness. A stable DC process can be achieved in materials with hardness smaller than HB220 and elongation larger than 18%.

There are a number of different application areas of DC technology. The main application area is heat exchange intensification [13], for example, finning of tubes for heat exchangers [14] including internal finning [15]. DC can be used for making boiling surfaces and capillary structures for heat pipes [16]. Other DC application areas are electrical joints manufacturing [17, 18].

2.3. Analysis of the Possibility to Use DC Method for Surface Hardening

It is well known that chips when turned may be heated up to the temperatures exceeding the temperatures of phase transformations in steels which may lead to hardening of chips at relevant cooling rates. During turning process by cutting, virtually all the power of the main drive measured in kilowatts is released in the cutting zone which has a volume of several cubic millimetres. Mechanical energy applied externally is localized in the plastic deformation area and in places where tool is touching the chips and workpiece and is converted into heat energy and latent energy of deformation. The material of chips is affected by such factors as shear strain, shear strain rate, high heating rate, high cooling rate and local environmental conditions. For example, when workpiece material is turned: C45E with speed of cut $V=160$ m/min the cutting temperature may be 1030 °C, shear strain may reach 400%, shear strain rate - 10^4 s⁻¹, heating rate - 10^6 °C/s, cooling rate - 10^3

°C/c, average normal stress - 350 MPa, and average shear stress - 250 MPa [19, 20].

When deformational cutting is performed, the cooling rates of the fin material necessary for hardening are achieved thanks to the conductive heat sink through the fin base to a colder workpiece core. A similar method of achieving hardening cooling rates without the use of cooling mediums is used in the following methods of heat treatment: induction and laser hardening.

Figure 2 demonstrates the principle of quench turning by using the method of deformational cutting without chips formation. Photograph of the treatment area and quenched shaft are shown in Figure 3.

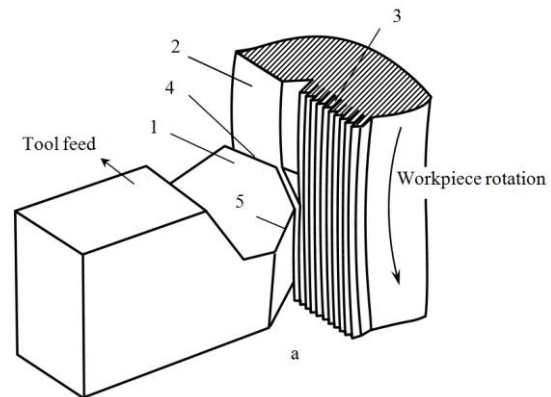


Figure 2. Concept of DC hardening. 1- DC tool, 2-surface to be hardened, 3 – hardened surface, 4 - cutting edge, 5 - deforming edge

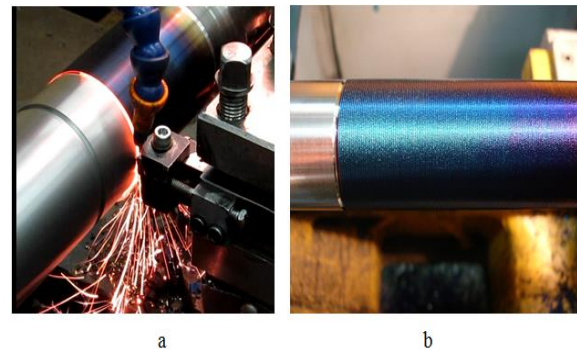


Figure 3. a - Process of DC hardening, b - hardened shaft

When deformational cutting is performed, the undercut layer may remain on the workpiece both with the retained interfin gaps and without gaps, i.e., tightly packed. Let us consider the case when interfin gaps remain at generation of finning. Figure 4 shows the plan view of the DC zone. The initial and final positions of the DC tool within one spindle revolution are marked as *I* and *II*, respectively. The cross-section of the future fin *ABCD* is cut by the cutting edge *BE* and moves on the tool rake surface. The tool deforming edge *BF* determines the final position of the fin marked as *A₁BCC₁D₁*. The slot width *b* depends on the undercutting angle, φ bending angle φ_1 , and axial tool feed per revolution *p*.

$$b = p - a \cdot \sin(\varphi_1) = p \cdot (\sin(\varphi) - \sin(\varphi_1)) \quad (1)$$

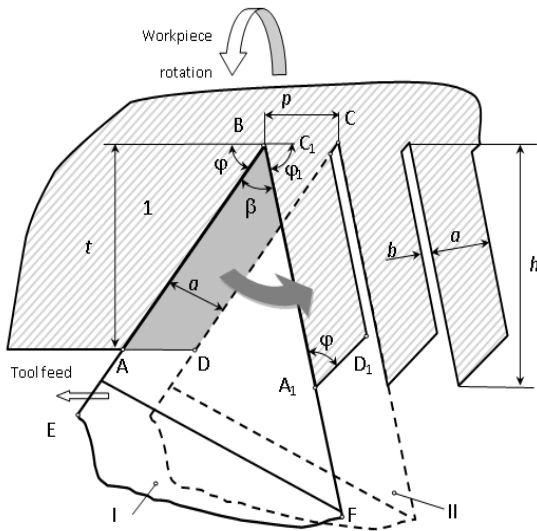


Figure 4. Fin shaping scheme by the deformational cutting method

To analyse the impact of angular parameters of the tool, we must transform (1)

$$b = 2S_o \cdot \sin\left(\frac{\Delta\varphi}{2}\right) \cdot \cos\left(\frac{180^\circ - \beta}{2}\right) \quad (2)$$

where $\Delta\varphi$ - the difference between the angles of bending and undercutting $\Delta\varphi = \varphi_1 - \varphi$, β - tool wedge approach angle $\beta = 180^\circ - (\varphi + \varphi_1)$.

As can be seen from Equation (2), the value of interfin gap, subject to a constant feed p , is affected not only by the difference of angles $\Delta\varphi$, but also by the tool wedge

approach angle β . The more β , the lesser is the interfin gap all other factors held equal.

As can be seen from Equation (1) and (2), if φ and φ_1 are equal, the slot width b will theoretically be zero. This means that the method of deformational cutting allows obtaining a non-porous, densely packed structure without interfin gaps subsequent to treatment.

Since no chips are removed, one may derive a formula for the height h of the obtained finned structure based on the principle of material volume retention:

$$h = t \cdot \frac{\sin \varphi_1}{\sin \varphi} - \frac{p}{2} \cdot \left[\frac{(\sin \varphi_1 - \sin \varphi)^2}{\sin \beta} - \sin \beta \right] \quad (3)$$

For narrow and zero interfin gaps, when ≈ 1 the expression for the microrelief depth will be simplified:

$$h = t + \frac{p \cdot \sin \beta}{2} \quad (4)$$

For quench hardening it is reasonable to use finning with interfin gap equal to zero, i.e., densely packed ribs. Modifications of such structures on different steels and with different pitches are shown in Figure 5.

Plastic deformations and friction of the undercut layer on the tool working surfaces function as sources of heat dissipation in the deformational cutting area. If the temperature of undercut layer exceeds the critical value and the cooling rate is high, the undercut layer undergoes hardening (Figure 6a). The undercut layer has the highest temperature in the area which is touching the tool face. Such uneven heating may be used to obtain a quenched fin partially hardened over its thickness (Figure 6b). Alternation of fully hardened layers and softer interlayers might be interesting from the point of view of enhancing score resistance of the friction knot.

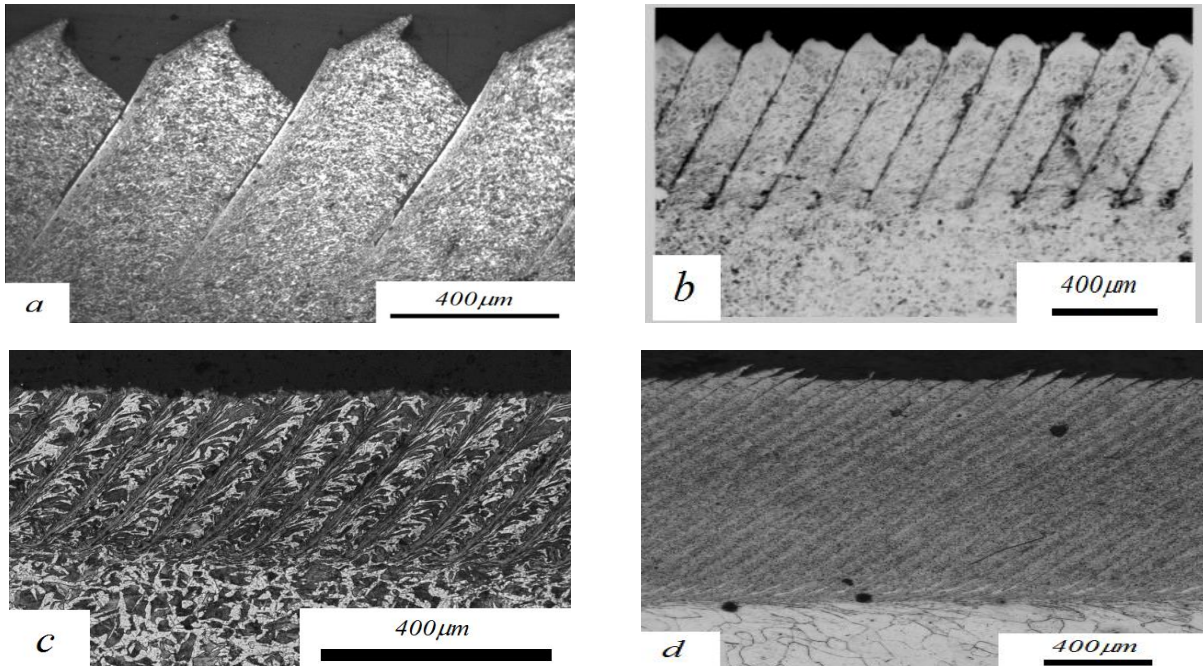


Figure 5. Examples of deformational cutting on steels with a zero interfin. a- steel 30HGSA, $p = 0,4$ mm; b – steel 20KH13, $p = 0,2$ mm; c – steel 35, $p = 0,1$ mm; d - Armco iron, $p = 0,1$ mm.

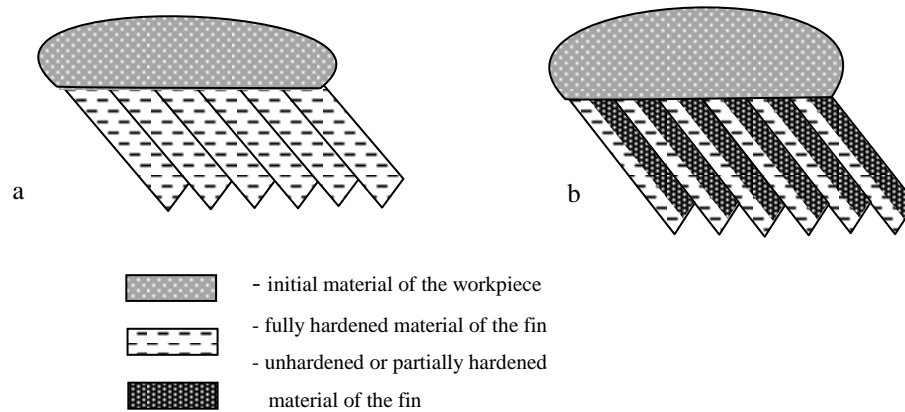


Figure 6. Modifications of structures obtained during quenching deformational cutting: a- fully hardened over the thickness of fin, c - partially hardened over the thickness of fin

3. Experimental Procedure

Cylindrical samples with a diameter of 60...80 mm made of steel after normalization were processed: steel 40H (0.4% C, 1.0% Cr), steel 20, (0.2% C), steel 35, (0.35% C), ShH15 (1.0 % C, 1.5 % Cr).

Screw-cutting lathe 1K62 was used to obtain hardening structures. Tool for deformational cutting was turned using two tooling materials: oxide ceramic of CM332 grade ($Al_2O_3+0.8\% MgO$), cemented carbide T15K6 (79% WC, 15% TiC, 6% Co), SiAlON of CC6060 grade (Sandvik Coromant) and CBN with the major cutting edge angle equal to $\phi=42^\circ$ and rake angle equal to $\gamma=-18^\circ$. The cutting speed V ranged from 3 to 5 m/s, advance of tool per shaft revolution was $S_0=0,05...0,4$ mm/Rev, cutting depth was $t=1,0...2,0$ mm.

The main component of the cutting force was measured by help of Kistler dynamometer, model 9257 (Switzerland), measurement data were displayed on the PC.

The cutting force measurement was carried out with a Kistler three-component piezoelectric dynamometer, type 9257B. The dynamometer was placed under the tool holder and connected to Kistler charge amplifiers, type 5011, with a frequency limit of 200 kHz.

Temperatures in the area of deformational cutting were measured by natural thermocouple method. Temperatures on the surface of the treatment area were measured by IRTIS-2000S thermograph (Russia).

For metallographic studies and microhardness measurement, transverse finning microsections were prepared: they were cut from a hardened shaft by using EDM processing technique. Metallographic analysis was carried out on the Olympus GX51 microscope with 1000x magnification on the polished surface of transverse sections pre-treated with 4% solution of HNO_3 in C_2H_5OH . Microhardness was automatically measured on the hardness tester EMCOTEST DuraScan 70 (Germany) using an indenter in the form of a diamond pyramid of a regular quadrihedral shape with a 100 kg load. The microstructure was examined with the help of an optical metallographic microscope Olimpus GX51 (Japan).

4. Results and Analysis

During machining using oxide cutting ceramics on steels 20, 35 and 40H, samples were obtained with a through hardened fin. The hardness of a fully quenched layer on through-hardened samples on steel 35 for the finning pitch $p=0.05$ mm was $650HV_{0.1}$ (58HRC), for $p=0.15$ mm the hardness is $670HV_{0.1}$ (59HRC), provided that initial hardness HV is $217_{0.1}$ (207HB) (Figure 7a). The hardness on steel 40H was $720..800HV_{0.1}$ (61..64HRC) with finning pitch 0.1 mm and on the average $680HV_{0.1}$ (59HRC) with finning pitch of 0.05 mm. The hardness for low-carbon steel 20 was $438...489HV_{0.1}$ (44...48HRC).

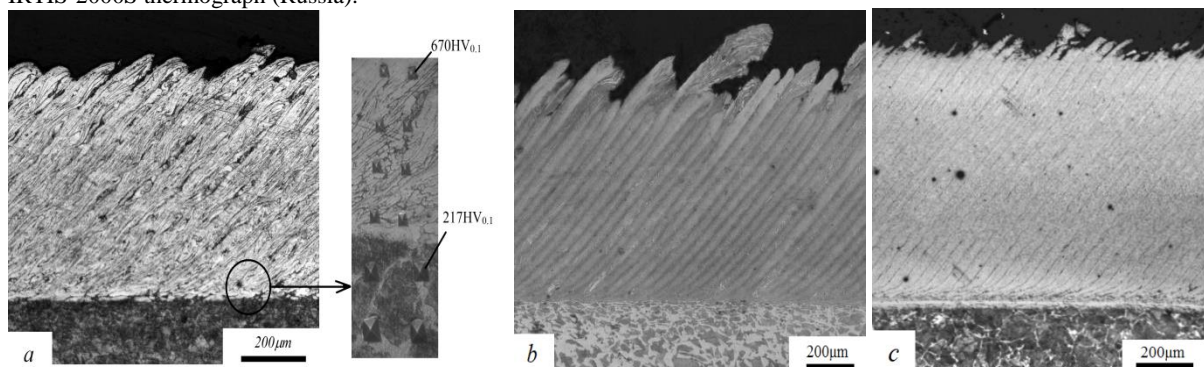


Figure 7. Total hardening over the thickness of fin. a- steel 35, pitch of the structure 0.15 mm, $740HV_{0.1}$, b - steel 35, pitch of the structure 0.05 mm, $650HV_{0.1}$, c - steel 40H, pitch of the structure 0.05 mm, $680HV_{0.1}$.

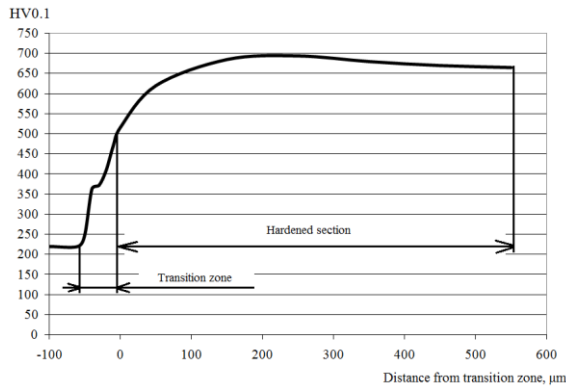


Figure 8. Distribution of microhardness over the thickness of the hardened layer. Steel 35, pitch of the structure $p=0.05$ mm.

If advance of tool per part revolution S is changed, or the cutting speed V and grade of tooling material is modified, one may achieve different ratios between the

thickness of hardening zones and finning interlayers without any structural transformations. The ratios of thickness of fully hardened layer to the total thickness 1:6 (Figure 9a), 1:4 (Figure 9b), 1:2 (Figure 9c) and 1:1 (Figure 9d) were obtained on steel 40H.

The hardness of a fully hardened interlayer on steel 35 was 670 HV0,1 (55...59 HRC). Hardness of partially hardened fin material is about 40 HRC. Increase in hardness can be explained both by partial hardening, and strain-hardening under the influence of high deformations in the course of deformational cutting.

During processing of SHKH15 (ShH15) grade steel with a pitch $p=0.2$ mm layers of fully quenched material were obtained which were 48 \square mm thick and had microhardness of the quenched zone of up to 950HV0.1 (68HRC) considering the initial hardness of the workpiece 220HB.

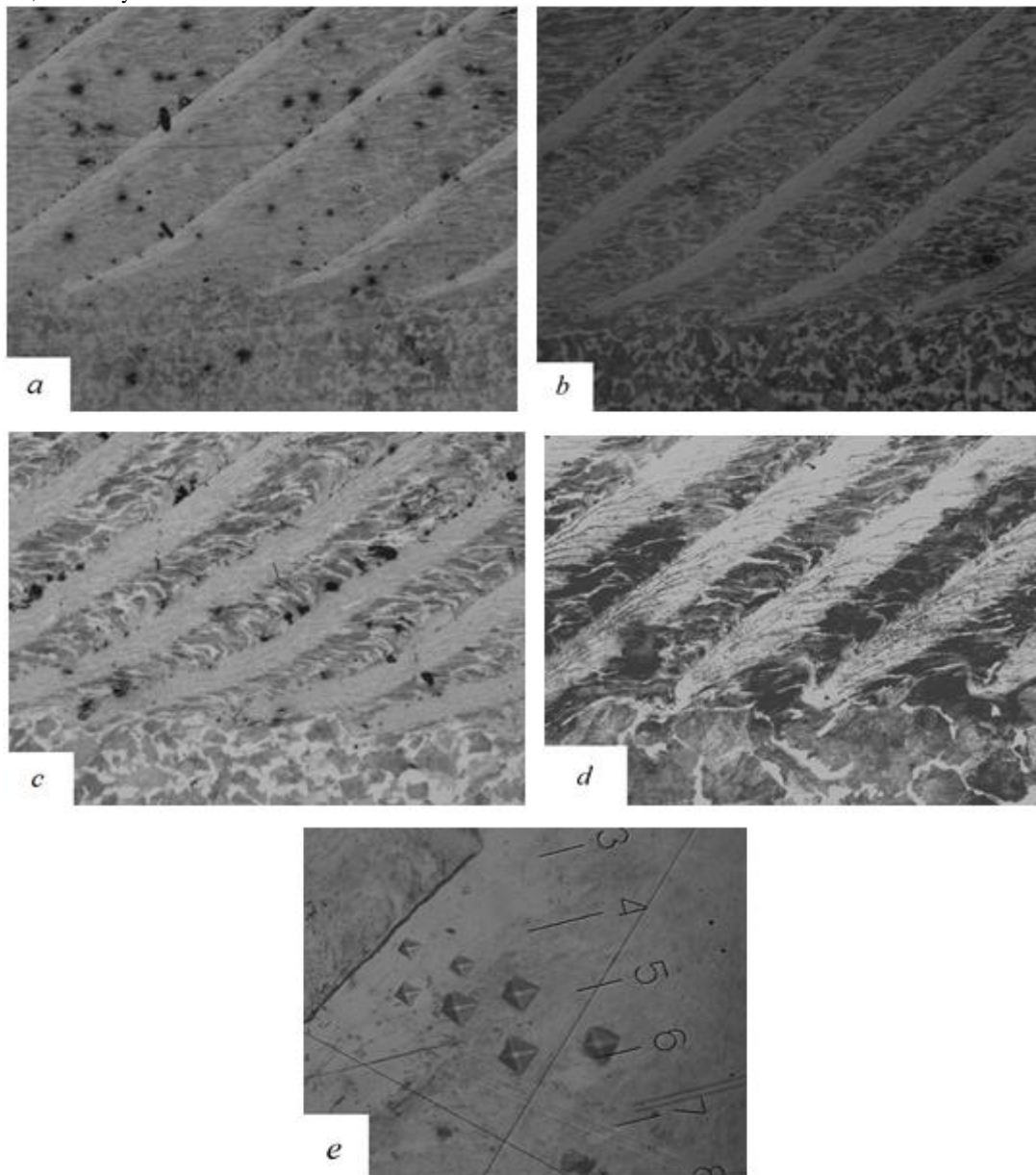


Figure 9. Hardened structures on steel 35 with various ratios of fully hardened and partially hardened material of fin. a - tool material ZM332, $p=0.15$ mm, b - tool material SiAlON, $p=0.1$ mm, c - tool material SiAlON, $p=0.1$ mm, d - tool material CBN, $p=0.1$ mm, e- comparison of dimensions of imprints in fully and partially hardened fin area

The hardness of a fully hardened interlayer on steel 35 was 670 HV_{0.1} (55...59 HRC). Hardness of partially hardened fin material is about 40 HRC. Increase in hardness can be explained both by partial hardening, and strain-hardening under the influence of high deformations in the course of deformational cutting.

During processing of SHKH15 (ShH15) grade steel with a pitch $p=0.2$ mm layers of fully quenched material were obtained which were 48 μ m thick and had microhardness of the quenched zone of up to 950HV_{0.1} (68HRC) considering the initial hardness of the workpiece 220HB.

Tribotechnical tests of samples which were performed with hardening by using the declared method confirmed their operational capability in sliding friction knots. We compared wear intensity and friction coefficient (Figure 6) of samples made of 40H steel with volumetric hardening in water and oil and subsequent low tempering (according to the modes recommended by reference books) to samples which were hardened by deformational cutting method without tempering and with low tempering at a temperature of 200°C within 40 minutes. The tests were carried out on Amsler A135 friction machine according to the friction scheme "disc on disc", with slippage velocity 0.08 m/s and load of 185 N. The material of the counterbody is cemented carbide VK8 (92% WC, 8% Co). As can be seen from the histogram (Fig. 10), samples hardened by the proposed method have a 10 to 40 % higher wear-resistance compared to the samples quenched by volumetric hardening.

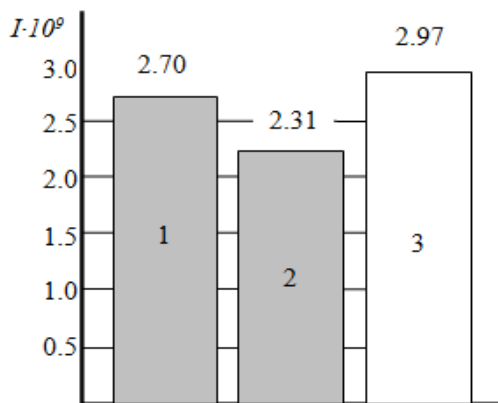


Figure 10. Wear intensity. Steel 40H. 1 – after DC without tempering, 2 – after DC with low-temperature tempering, 3 – after standard volumetric tempering with low-temperature tempering

5. Discussion

Let us analyse the examined option of deformational cutting of a cylindrical workpiece made of 40H steel and with diameter 48 mm, with advance $p=0.1$ mm/Rev, cutting depth $t=1.0$ mm, cutting speed $V=3$ m/s. (rotation speed of lathe spindle $n=1200$ RPM). Measurement of the main component of the cutting force using Kistler dynamometer revealed that $P_z=800$ N. Measurement of the temperature in the cutting zone by using natural thermocouple method showed that $T=1100^\circ\text{C}$.

Volumetric flow of metal q passing through the treatment area will be:

$$q = t \cdot p \cdot V = 0,3 \text{ mm}^3 / \text{s} \quad (5)$$

Mass flowrate of metal passing through the treatment area will be:

$$G = \rho \cdot q = 2,36 \text{ g} / \text{s} \quad (6)$$

where $\rho=7,85 \cdot 10^3$ kg/m³ – is specific weight of 40H steel.

Power which is released in the treatment area will be:

$$N = P_z \cdot V = 2,4 \text{ kV} \quad (7)$$

Assuming that all the heat generated in the treatment area is used for heating of the undercut layer, the fin temperature will be:

$$T = N / (C_p \cdot G) = 1533^\circ \text{C} \quad (8)$$

where $C_p = 663$ J/(kg·K) – is a mean specific heat capacity for the temperature range 20...1500 °C for steel 40H.

The calculated temperature value doesn't coincide with the temperature measured by using natural thermocouple method. This is due to the fact that not all the power generated in the treatment area is used for heating of the undercut layer. Some part of the heat flow passes into the tool, into the surrounding environment thanks to convective heat transfer and radiation, some part of heat flow goes directly into the workpiece, bypassing the undercut layer. When cutting is performed, energy is also consumed for elastic deformations, shattering of grains (increase in interface boundaries between grains), formation of new surfaces, formation of dislocations and their motion [21], and phase transformations.

Time period t during which metal remains in the heating area (in the area of contact with tool face) was estimated over the length of contact between undercut layer and tool face and cutting speed. For processing conditions mentioned, the length of the contact zone is 1.2 mm. Therefore,

$$t = l / V = 4 \cdot 10^{-4} \text{ s} \quad (10)$$

Rate of τ metal heating in the treatment area up to 1100°C will be:

$$V_{heat} = \Delta T / t = 2.7 \cdot 10^6 \text{ K} / \text{s} \quad (11)$$

This value exceeds the heating rates which are typical for laser quenching and are up to 10^6 K/s [22].

Energy to volume ratio Q generated in the treatment area due to plastic deformations, internal and external friction is determined as:

$$Q = N / q = 8.0 \text{ kJ} / \text{cm}^3 \quad (12)$$

Heated layers, as with laser quenching, are cooled down through transfer of heat to the workpiece body. The cooling rate during quenching deformational cutting was assessed based on the temperature difference on the cutting area surface which was 900 °C, and on the temperature of adjacent fin every other revolution of the workpiece. The differential temperature was 450°C. The measurements were carried out by using IRTIS-2000S thermograph. If frequency of rotation of the workpiece is 1200 rpm, 0.05 s is required for one revolution of the workpiece which brings a cooling rate $V_{cool} = 9.0 \cdot 10^3$ °C/c. This is an assessment of the minimum cooling rate since the

thermograph recorded the temperature of outer layers. For layers located closer to the fin bottom, the cooling rate should be even higher. The cooling rate is also higher than the cooling rate during laser quenching which is about 10^3 °C/c. [23].

The authors didn't manage to obtain a defect-free surface of the hardened shaft. As it is seen from the photographs showing transverse sections of hardened surface Figure 7a, the top layer has defects featuring delamination and sagging. This fact is still a substantial disadvantage since the defective layer needs to be removed by hard turning on the same machine which was used for hardening or by a separate grinding operation to remove about 1/4 of the thickness of the hardened layer.

The throughput of the operation for the case considered - where the shaft with diameter of 48 mm is hardened by deformational cutting method - is 0.12 m of the length of the hardened shaft surface per minute and the depth of a hardened layer is up to 1 mm.

6. Conclusion

1. A new method of surface hardening was developed and put to an evaluation test: the subject of method is machining without formation of chips.
2. When deformational cutting is made, heating temperature, heating and cooling rates are sufficient enough to ensure phase transformations of the undercut layer material.
3. Unlike laser quenching, phase transformations occur at higher degrees and rates of deformation.
4. Hardened surface layers showed more uniform hardness over thickness compared to other methods of surface hardening.
5. It has been demonstrated that it is possible to obtain laminated structures with inclined layers and that is also possible to control the ratio of thickness values of hardened and unhardened areas.
6. The adoption of DC hardening method may have economical and higher productivity benefit due to its increased integration level. The new method improves efficiency of the quenching operation, allows abandoning transport operations for heat treatment, reduces energy intensity of quenching, and makes specialized thermal equipment unnecessary.

Acknowledgment

The present study was supported by the Ministry of Education and Science of Russia.

References

- [1] Rajan TV, Sharma CP. Heat treatment: Principles and techniques. 2nd ed. New Delhi: PHI Learning Pvt. Ltd.; 2012.
- [2] Davis JR. Surface Hardening of Steels: Understanding the Basics. USA: ASM International Materials Park; 2002.
- [3] Y.B. Guo, G.M. Janowski, "Microstructural Characterization of White Layers by Hard Turning and Grinding". Transactions of the North American Manufacturing Research Institute of SME (2004), vol. 32, 367–374.
- [4] Y.B. Guo, A.W. Warren, "Microscale Mechanical Behavior of the Subsurface by Finishing Processes". ASME Journal of

- Manufacturing Science Engineering, vol. 127 (2004), 333–338.
- [5] S. Naik, C. Guo, S. Malkin, D.V. Viens, C.M. Pater and S.G. Reder, "Experimental Investigation of Hard Turning". 2nd International Machining and Grinding Conference, Dearborn, Michigan, USA, 1997.
- [6] J. Kundrak, A.G. Mamalis, K. Gyani, V. Bana, "Surface layer microhardness changes with high-speed turning of hardened steels". International Journal of Advanced Manufacturing Technology, vol. 53 (2001), No. 1, 105-112.
- [7] Z.Q. Liu, X. Ai, Z.H. Wang, "A Comparison Study of Surface Hardening by Grinding Versus Machining". Key Engineering Materials, Vols. 304-305 (2006), 156-160.
- [8] Salonitis K. Grind Hardening Process. Berlin: Springer-Verlag GmbH; 2015.
- [9] T. Foeckerer, M.F. Zaeh, O.B. Zhang, "A Three-Dimensional Analytical Model to Predict the Thermo-Metallurgical Effects within the Surface Layer During Grinding and Grind-Hardening". International Journal of Heat and Mass Transfer, vol. 56 (2013), 223-237.
- [10] G. Hyatt, M. Mori, T. Foeckerer, M.F. Zaeh, N. Niemyer, M. Duscha, "Integration of Heat Treatment into the Process Chain of a Mill Turn Center by Enabling External Cylindrical Grind-Hardening". Production Engineering - Research and Development (WGP Annals), vol. 7 (2013), No. 6, 571-584.
- [11] N.N. Zubkov, S.G. Vasiliev, V.V. Poptsov, "The surface quench hardening method by cutting and deforming tools". Patent of RF No. 2556897, IPC C21D 8/00. Application filed on 21.01.2014, published on 22.06.2015.
- [12] N. Zoubkov, A. Ovtchinnikov, "Method and Apparatus of Producing a Surface With Alternating Ridges and Depressions," U.S. Patent No. 5,775,187.5 (1998).
- [13] I. A. Popov, N.N. Zubkov, S.I. Kas'kov, A.V. Shchelchikov, "Heat Transfer during the Boiling of Liquid on Microstructured Surfaces. Part 1: Heat Transfer during the Boiling of Water". Thermal Engineering, Vol. 60 (2013), No. 3, 157–165.
- [14] R. Kukowski, "MDT—Micro Deformation Technology". ASME International Mechanical Engineering Congress and Exposition, Washington D.C., USA, 2013.
- [15] P. Thors, , N. Zoubkov, "Method for Making Enhanced Heat Transfer Surfaces," U.S. Patent No. 8,573,022 (2013).
- [16] A. Yakomaskin, V. Afanasiev, N. Zubkov, D. Morskoy, "Investigation of Heat Transfer in Evaporator of Microchannel Loop Heat Pipe". ASME Journal of Heat Transfer, Vol. 135 (2013), Issue 10, 100-106.
- [17] L. Solovyeva, N. Zubkov, B. Lisowsky, A. Elmoursi, "Novel Electrical Joints Using Deformation Machining Technology—Part I: Computer Modeling". IEEE Transactions on Components, Packaging, and Manufacturing Technology, vol. 2 (2012), Issue 10, 1711–1717.
- [18] L. Solovyeva, N. Zubkov, B. Lisowsky, A. Elmoursi, "Novel Electrical Joints Using Deformation Machining Technology—Part II: Experimental Verification". IEEE Transactions on Components, Packaging, and Manufacturing Technology, Vol. 2 (2012), Issue 10, 1718–1722.
- [19] Klocke F. Manufacturing Processes 1: Cutting. Berlin: Springer-Verlag; 2011.
- [20] S.K. Chou, C.J. Evans, "White layers and thermal modeling of hard turning surfaces". International Journal of Machine Tools & Manufacture, vol. 39 (1999), 1863–1881.
- [21] Davim P. Machining of Hard Materials. London: Springer-Verlag London Limited; 2011.
- [22] Burakowski T, Wierzchon T. Surface Engineering of Metals: Principles, Equipment, Technologies. Boca Raton: CRC Press; 1998.
- [23] Majumdar JD, Manna I. Laser-Assisted Fabrication of Materials. Berlin: Springer-Verlag Berlin Heidelberg; 2013.

Optimal Scheduling and Sequencing of Operating Room Under Emergency Cases

Abbas Al-Refaie ^{a*}, Mays Judeh ^b, Ming-Hsien Li ^c

^a Dept. of Industrial Engineering, University of Jordan, Amman 11942, Jordan.

^b Master student in the dept. of Industrial Engineering, University of Jordan, Amman.

^c Department of Industrial Engineering and Systems Management, Feng Chia University

Received MAY, 15, 2016

Accepted NOV, 20, 2016

Abstract

Preparation is the secret to survive in the emergency events whether they are major accidents, car crashes, bombings or even a war. Operating rooms are the most important resources in any hospital that should always be improved. The present study, therefore, proposes a mathematical model for concurrent optimal patients' scheduling and sequencing in newly opened operating rooms under emergency events. In this model, the objective function is to maximize patient's assignment over the empty available rooms. While, the model constraints include operating room, priority, surgeons, equipment, additional constraints on start time and precedence, and integrality constraints. Data related to patients (operation start time, duration, and due date) operating rooms, and equipment and surgeon availability in each room were collected from a local hospital including availability. The proposed model was then implemented to determine optimal scheduling and sequencing of operating rooms that maximizes the number of survived patients in emergency cases. The patient-to-room assignment and surgery start time are finally obtained for all patients. In conclusions, the proposed model may support hospital administration in obtaining concurrent scheduling and sequencing in emergency cases and increasing the utilization of operating rooms.

© 2017 Jordan Journal of Mechanical and Industrial Engineering. All rights reserved

Keywords: Emergency cases; Optimization; Scheduling, Sequencing; Operating room.

1. Introduction

In order to survive in today's competitive market place, organizations are urged to enhance their performance [1-3]. Operating Rooms are usually considered as bottleneck area in hospitals. Hence, decision makers always aim to obtain better coordination between the available resources in the hospital which stimulate the operating rooms to meet demand increase, improving the productivity and efficiency in addition to increase the number of saved lives.

Recently, scheduling and sequencing the operating rooms have become a real challenge. Scheduling of surgeries is considered as the most suitable tool to improve the performance of ORs with consideration to the related limited constraints [4]. Operating rooms scheduling identifies which surgeries to perform and determines the assigned resources to each surgery. However in order to increase OR efficiency, an accurate expectation of each patient's start time for surgery is needed. Therefore many studies were developed to obtain operating rooms scheduling and sequencing. A two-step methodology was proposed by Jebali *et al.* [5] for a daily operating rooms scheduling where in the first step surgeries were allocated to operating rooms with the objective function of minimizing hospitalization, idle time, and overtime costs while in the second step a mathematical model was used to

sequence the surgeries. Another two models for daily scheduling were formulated by Saadouli *et al.* [6] for elective surgery optimization.

Key elements of surgeries (surgeons, patients and rooms) should be taken into account while scheduling operating rooms. Surgeons and rooms have limited working hours and specialized equipment is not available in all rooms. Surgeon should treat one patient at a time and one patient should be treated in each room at each time. In addition, normally not all operating rooms operate every day in the hospitals; however, some of the rooms, which are scheduled to be closed in some day, can be utilized in emergency events, and this is the case to which scheduling and sequencing is optimized in the present paper.

A smart hospital can react to the unexpected events in real time [7]. Therefore, it is essential to have a proactive plan that aims to save as many patients' lives as possible. In the unexpected events, the demand for medical treatment usually exceeds the actual treatment capacity for the hospital [8]. Thus, methods were developed for optimal scheduling of operating rooms in cases of unexpected events. Lamiri *et al.* [9] developed a stochastic model for operating rooms where capacity is shared between emergency and elective patients with the objective of minimizing costs. Nouaouri *et al.* [10] maximized the number of treated patients for a scheduling problem in disasters based on integer linear programming model that aimed to optimize the operating rooms' scheduling while

* Corresponding author e-mail: abbas.alrefai@ju.edu.jo

maximizing the number of treated patients in the unexpected cases. The objective in the unexpected circumstances is to save as many lives as possible without consideration to the related cost.

Nevertheless, the models proposed in previous studies for scheduling emergency patients did not consider the sequencing in the closed operating rooms. Moreover, even in the normal circumstances, scheduling and sequencing were conducted separately. Concurrent optimization of scheduling and sequencing will result in obtaining the results in one step and thereby save considerable time and effort. In the present study, therefore, a proposed model is formulated to optimize the scheduling and sequencing of each patient's surgery in the newly operating rooms under the unexpected events to maximize the number of treated patients while taking into consideration the challenging constraints. The remaining part of the present paper including the introduction is outlined as follows. Section 2 presents the proposed optimization model. Section 3 illustrates the proposed model on a real-life application. Section 4 discusses the results of the study. Section 5 presents the conclusions and recommendations for future research.

2. Proposed Optimization Model

When operating rooms are scheduled, few empty rooms are normally decided inoperable on certain days. Those rooms can be utilized to hospitalize the patients in emergency cases. The formulated model utilizes the empty rooms in order to treat the patients injured from the emergency event in addition to determine the start time and the sequence of their surgeries. The model is formulated under the following assumptions: (i) Available operating rooms are the rooms scheduled to be closed on the day of the emergency event, (ii) the total duration of surgery is divided into three parts: the time required for preparation and setup (for both; patient and operating room), the time required for surgery act itself, and cleaning time, (iii) All time durations are considered as deterministic, (iv) number of surgeons is equal to the number of rooms such that each surgeon operates in certain room and he/she is available in this room during working hours, and (v) Due to emergency, regular working hours of rooms includes the maximum permitted overtime. Further, the amount of overtime and idle time are neglected. In order to solve the optimization model, the following information is given and deterministic:

- The disruption time (t_v), number of operating rooms (O), number of emergency patients (I) and number of surgeons (S) in the hospital.
- Time durations for preparation (pt_i), surgical act (st_i) and cleaning (ct_i) for each patient and his/her due day (due_i).
- The start of working time (A_s) and the end of working time (B_s) for each surgeon. In addition, the regular opening time (R_o) for an operating room on the day of emergency event.
- Equipment availability matrix on the day of emergency event (ω_{io} -Matrix) and the matrix of the assigned surgeon to each patient (ρ_{is} -Matrix).

Let i denotes the emergency patient index where $i \in [1, \dots, I]$ and o denotes operating room index where $o \in [1, \dots, O]$. The decision variables are as follows: x_{io} is a binary decision variable which identifies which room o is assigned to emergency patient i , it equals one if patient i is assigned to room o and zero otherwise, τ_i identifies the start time of the surgery of patient i and θ_{ij} , which identifies the precedence of patients' surgeries in operating rooms. The purpose in emergency events is to treat as many patients as possible regardless of the related cost. Therefore the objective function is to maximize patient's assignment over the empty available rooms which can be expressed mathematically as follows:

$$\text{Max} \sum_{o=1}^O \sum_{i=1}^I x_{io} \quad (1)$$

The model constraints are:

2.1. Operating Room Constraints

- Operating room availability; this means that the total of surgery durations for all patients in any day is constrained by the regular working duration of room o . Let R_o denotes the regular working hours of room o on the emergency day (in minutes), pt_i denotes the time duration for preparation, st_i denotes the time duration for surgical act, and ct_i denotes time duration for cleaning. Then, operating room availability is formulated as follows:

$$\sum_{i=1}^I (x_{io} \times (pt_i + st_i + ct_i)) \leq R_o, \quad o \in [1, \dots, O] \quad (2)$$

- In each operating room at each time, one patient only should be treated. Therefore, when patient i precedes patient j in room o , the start time of patient j should be greater than the whole time required for the surgery of patient i , which includes the time required for preparation, the surgery itself and the time required for cleaning as expressed by constraint (3).

$$\tau_j \geq \tau_i + pt_i + st_i + ct_i - M(3 - \theta_{ij} - x_{io} - x_{jo}), \quad (3)$$

$$\forall o \in [1, \dots, O], i \in [1, \dots, I], j \in [1, \dots, I] / i \neq j$$

2.2. Priority Constraints

- Some patients should be operated in the same day of the emergency in such case the due date equals the same day of disruption. Let U_{io} be a binary variable that reflects the urgent assignment of patient i in room o . Eq. (4) ensures that patients in urgent need for surgery are assigned on the same day of emergency event, where due_i denotes due date of emergency patient i .

$$\sum_{o=1}^O U_{io} = 1, \quad \forall i \in [1, \dots, I] / due_i = 0 \quad (4)$$

- Other patients, who are not in urgent need of surgery their due date, are treated as second priority as expressed in Inequality (5).

$$\sum_{o=1}^O U_{io} \leq 1, \quad \forall i \in [1, \dots, I] / due_i > 0 \quad (5)$$

2.3. Surgeons Constraints

- Surgeon's availability which means that the total of durations of the surgeries scheduled for surgeon s is limited by the availability of this surgeon in hospital as stated in Eq. (6). Let A_s and B_s denote the beginning and the end of surgeon s working hours on emergency day (in minutes), respectively. Let p_{is} denotes a binary variable that presents the assignment of patient i to surgeon s. Then,

$$\sum_{i=1}^I \sum_{o=1}^O (x_{io} \times (pt_i + st_i + ct_i) \times \rho_{is}) \leq (B_s - A_s), \quad (6)$$

$$\forall s \in [1, \dots, S]$$

- Each surgeon should complete his/her assigned surgeries before the end of his/her working time as expressed in Inequality (7).

$$\tau_i + pt_i + st_i - M(2 - \rho_{is} - \sum_{o=1}^O x_{io}) \leq B_s, \quad (7)$$

$$\forall i \in [1, \dots, I], s \in [1, \dots, S]$$

- Further, the surgeries assigned to surgeon s should start after the beginning of his/her working time as expressed in Inequality (8).

$$\tau_i + pt_i \geq \rho_{is} \times A_s - M(1 - \sum_{o=1}^O x_{io}), \quad (8)$$

$$\forall i \in [1, \dots, I], s \in [1, \dots, S]$$

- Each surgeon should operate on one patient at a time. Thus, when patients i and j are assigned to the same surgeon such that patient i precede patient j, the preparation of patient j surgery are completed once the surgery of patient i is finished or after that. Mathematically,

$$\tau_j + pt_j \geq (\tau_i + pt_i + st_i) - M(5 - \theta_{ij} - \rho_{is} - \rho_{js} - \sum_{o=1}^O x_{io} - \sum_{o=1}^O x_{jo}), \quad (9)$$

$$\forall i \in [1, \dots, I], s \in [1, \dots, S], j \in [1, \dots, I] / i \neq j$$

2.4. Equipment Constraints

- Equipment availability is another constraint that should be taken into consideration such that the needed equipment for patient's surgery should be available in the assigned room as expressed in Inequality (10) where ω_{io} denotes the availability of the equipment required for patient i in room o on emergency day.

$$x_{io} \leq \omega_{io}, \quad \forall i \in [1, \dots, I], o \in [1, \dots, O] \quad (10)$$

2.5. Additional Constraints on Start Time and Precedence

- All surgeries should start after disruption time as formulated in Inequality (11):

$$\tau_i \geq t_v, \quad \forall i \in [1, \dots, I] \quad (11)$$

- When the surgery of patient i starts in precedence to the surgery of patient j, the start time of patient j should be before the start time of patient i as expressed in Inequality (12):

$$\tau_j \geq \tau_i - M(1 - \theta_{ij}), \quad (12)$$

$$\forall i \in [1, \dots, I], j \in [1, \dots, I] / i \neq j$$

- Surgery precedence is determined between patients who are chosen to be treated on the disruption day, as presented in Eq. (13).

$$\theta_{ij} + \theta_{ji} = \sum_{o=1}^O x_{io} \times \sum_{o=1}^O x_{jo}, \quad (13)$$

$$\forall i \in [1, \dots, I], j \in [1, \dots, I] / i > j$$

2.6. Integrality Constraints

- The integrality constraints are expressed as follows:

$$x_{io} \in \{0, 1\} \quad (14)$$

$$\theta_{ij} \in \{0, 1\} \quad (15)$$

Merging the objective function and constraints will formulate Model I as follows which is used to assign the emergency patients to the empty available operating rooms and determine the start time of each patient surgery.

$$\text{Max} \sum_{o=1}^O \sum_{i=1}^I x_{io}$$

Subject to:

$\sum_{i=1}^I (x_{io} \times (pt_i + st_i + ct_i)) \leq R_o, \quad \forall o \in [1, \dots, O]$	[Room availability]
$\tau_j \geq \tau_i + pt_i + st_i + ct_i - M(3 - \theta_{ij} - x_{io} - x_{jo}),$ $\forall o \in [1, \dots, O], i \in [1, \dots, I], j \in [1, \dots, I] / i \neq j$	[Room is occupied by one patient at a time]
$\sum_{o=1}^O U_{io} = 1, \quad \forall i \in [1, \dots, I] / due_i = 0$	[Assignment of urgent patients]
$\sum_{o=1}^O U_{io} \leq 1, \quad \forall i \in [1, \dots, I] / due_i > 0$	[Potential assignment of not urgent patients]
$\sum_{i=1}^I \sum_{o=1}^O (x_{io} \times (pt_i + st_i + ct_i) \times \rho_{is}) \leq (B_s - A_s), \quad \forall s \in [1, \dots, S]$	[Surgeon availability]
$\tau_i + pt_i + st_i - M(2 - \rho_{is} - \sum_{o=1}^O x_{io}) \leq B_s, \quad \forall i \in [1, \dots, I], \forall s \in [1, \dots, S]$	[Surgeries to be within surgeon working time]
$\tau_i + pt_i \geq \rho_{is} \times A_s - M(1 - \sum_{o=1}^O x_{io}), \quad \forall i \in [1, \dots, I], \forall s \in [1, \dots, S]$	[Surgeries to be within surgeon working time]
$\tau_j + pt_j \geq (\tau_i + pt_i + st_i) - M(5 - \theta_{ij} - \rho_{is} - \rho_{js} - \sum_{o=1}^O x_{io} - \sum_{o=1}^O x_{jo}),$ $\forall s, i, j \in [1, \dots, I] / i \neq j$	[Surgeon performs one surgery at a time]
$x_{io} \leq \omega_{io}, \quad \forall i \in [1, \dots, I], \forall o \in [1, \dots, O]$	[Equipment availability]
$\tau_i \geq t_v, \quad \forall i \in [1, \dots, I]$	[Surgeries to start after disruption time]
$\tau_j \geq \tau_i - M(1 - \theta_{ij}), \quad \forall i \in [1, \dots, I], j \in [1, \dots, I] / i \neq j$	[Respecting patient precedence in room]
$\theta_{ij} + \theta_{ji} = \sum_{o=1}^O x_{io} \times \sum_{o=1}^O x_{jo}, \quad \forall i \in [1, \dots, I], j \in [1, \dots, I] / i > j$	[Surgery precedence]
$x_{io} \in \{0, 1\}$	[Binary Variable]
$\theta_{ij} \in \{0, 1\}$	[Binary Variable]

3. Illustrations

The scheduling and sequencing model was implemented in one of the leading private hospitals in Jordan. The data were obtained with the assistance of the hospital where physician and medical-staff interviews were conducted to gather the relevant information. Assuming that at 9:20 am, a traffic accident occurs and the casualties in urgent need of surgical intervention were transferred to the nearest hospital. The twenty casualties in need of surgery were admitted around 9:30 am and the hospital opened the three operating rooms that were scheduled to be closed on that day. One surgeon will take

over each room of the newly-opened operating rooms. The opening duration for each room (R_o) is 480 minutes and the time of disruption (t_v) is 9:30 am. All surgeons start their working hours at 8:00 am ($A_s = 0$) and their working hours end at 4:00 ($B_s = 480$). Patient-related variables, Equipment Availability Matrix and Patient-Surgeon Assignment Matrix are presented in Table 1. Priority was given to the most urgent cases by stating their latest start time (due_i) is equal to zero. Since each surgeon works in a certain room that is appropriate for surgeon's specialty and patient needed surgery, Equipment Availability Matrix and Patient-Surgeon Assignment Matrix will be the same.

Table 1. Patient-related variables and equipment availability

Patient (i)	Time durations			Due _i (day)	Equipment availability (ω _{io}) And Surgeon Availability (ρ _{is}) in each room		
	p _{t_i}	s _{t_i}	c _{t_i}		1	2	3
1	15	60	10	1	0	1	0
2	10	30	5	1	1	0	0
3	10	50	4	0	0	0	1
4	15	90	15	0	0	1	0
5	7	25	3	0	1	0	0
6	4	30	4	1	1	0	0
7	15	40	10	1	0	0	1
8	5	30	5	0	0	1	0
9	10	50	5	1	0	1	0
10	20	80	10	0	1	0	0
11	17	35	7	1	0	0	1
12	5	20	5	1	0	1	0
13	15	40	10	1	1	0	0
14	5	25	5	0	0	0	1
15	10	50	5	0	0	0	1
16	15	60	10	0	0	0	1
17	7	40	5	0	1	0	0
18	6	25	5	1	0	1	0
19	15	40	10	1	0	0	1
20	5	30	5	0	1	0	0

Table 2. Patients' assignment

Patient (i)	Room	Patient (i)	Room
1	2	11	3
2	1	12	2
3	3	13	1
4	2	14	3
5	1	15	3
6	1	16	3
7	3	17	1
8	2	18	2
9	2	19	3
10	1	20	1

Table 3. Patient's surgery start times

Patient (i)	τ _i	Patient (i)	τ _i
1	90	11	345
2	128	12	213
3	420	13	265
4	308	14	310
5	345	15	243
6	90	16	90
7	-	17	213
8	428	18	177
9	243	19	178
10	380	20	173

Solving the complete model by using LINGO, 19 patients out of 20 were scheduled in the three newly opened operating rooms. Patients' assignment is presented in Table 2. Patient's surgery start times were obtained as well and are presented in Table 3.

4. Results

The proposed model efficiently scheduled and sequenced patients to newly opened operating rooms. Patients' assignment, sequence and start times are illustrated in Fig. 1. It is clear that the proposed model efficiently assigned the patients to operating rooms and determines the start time for each operation. It is observed in Fig. 1 that all patients; except patient 7, are assigned operation's start time to meet the stated model objectives.

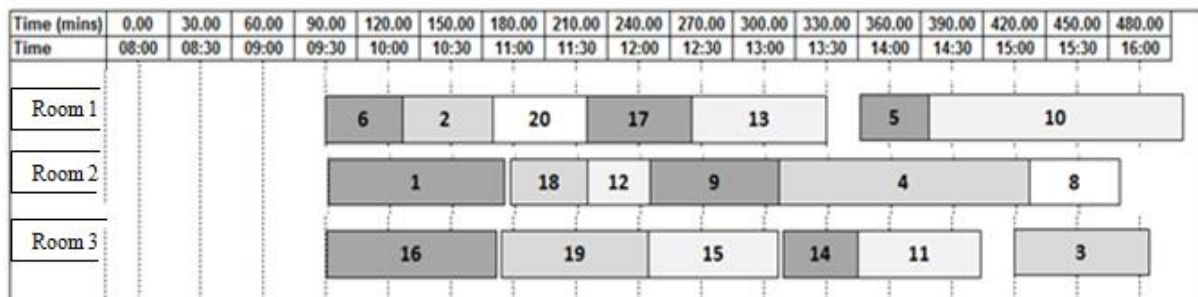


Figure 1. Illustration of Patients' assignment, sequence and start times

The model is a good approach for concurrent scheduling and sequencing, because it takes into account the availability of surgeons and equipment distribution in operating rooms, effectively utilizes the closed operating rooms and saves considerable time and effort in obtaining results. Such advantages are highly beneficial especially in emergency cases in which patients' accommodation plan must be determined as soon as possible.

5. Conclusion

The present study developed an optimization model for concurrent scheduling and sequencing operating rooms during emergency events. Data for twenty casualties in need of surgery were collected from a local hospital. The proposed was then utilized for obtaining the optimal number of patients to be treated, patient-to-room assignment matrix, and operation start times. The obtained results revealed that the proposed model is efficient in maximizing the number of treated patients and improving the utilization of operating rooms in emergency cases. In conclusions, the developed model provides a proactive model to maximize number of treated patients in case of emergency events and to increase the utilization of hospital's available resources, and thereby reduces administration time and effort. This model can be further extended to include additional constraints, such as nurses' availability and their working time. Moreover, surgeons' utilization can be studied as well by a detailed study of patients' assignment to surgeons.

References

- [1] A. Al-Refaie, N. Bata, D. Eteivi, I. Jalham, " Examining Factors that Affect Passenger's Overall Satisfaction and Loyalty: Evidence from Jordan Airport, " *Jordan Journal of Industrial and Mechanical Engineering* Vol. 8, No. 2, pp. 94-101, 2014.
- [2] A. Al-Refaie A., R. ENajdawi, R. SY, " Using DEA window analysis to measure efficiencies of blowing machines in plastics industry, " *Jordan Journal of Mechanical and Industrial Engineering*, Vol. 10, No. 1, pp. 27-38, 2016.
- [3] A. Al-Refaie, O. Ghnaimat, M.H. Li, " Effects of ISO 9001 certification and KAAE on performance of Jordanian firms, " *Jordan Journal of Mechanical and Industrial Engineering*, Vol. 6, No. 1, pp. 45-53, 2012.
- [4] M. Souki, "Operating Theatre Scheduling with Fuzzy Durations," *Journal of Applied Operational Research*, Vol. 3, No. 3, pp. 177–191, 2011.
- [5] A. Jebali, A.B.H. Alouane, and P. Ladet, "Operating Rooms Scheduling," *International Journal of Production Economics*, Vol. 99, pp. 52–62, 2006.
- [6] H. Saadouli, B. Jerbi, A. Dammak, L.Masmoudi, and A. Bouaziz, "A Stochastic Optimization and Simulation Approach for Scheduling Operating Rooms and Recovery Beds in an Orthopedic Surgery Department," *Computers & Industrial Engineering*, Vol. 80, pp. 72–79, 2015.
- [7] A. Al-Refaie, T. Chen, and M. Judeh, "Optimal Operating Room Scheduling for Normal and Unexpected Events in a Smart Hospital," *Operations Research International Journal*, online, 2016.
- [8] I. Nouaouri, J.-C. Nicolas and D. Jolly, "Operating Room Scheduling Under Unexpected Events: The Case of a Disaster," *Journal of Applied Operational Research*, Vol. 3, No. 3, pp. 163–176, 2011.
- [9] M. Lamiri, X. Xie, A. Dolgui, and F. Grimaud, "A Stochastic Model for Operating Room Planning with Elective and Emergency Demand for Surgery," *European Journal of Operational Research*, Vol. 185, pp. 1026–1037, 2008.
- [10] I. Nouaouri , J.C. Nicolas, and D. Jolly , "Scheduling of Stabilization Surgical Cares in Case of a Disaster," *The IEEE International Conference on Industrial Engineering and Engineering Management (IEEM)*, Hong Kong, 2009.

Bits Reduction in the Electrodeposition Process of a Pickup Truck: a Case Study

A. R. Nabiilah ^{* a}, Z. Hamedon ^{a,b}, M. T. Faiz ^a

^a Faculty of Manufacturing Engineering, University Malaysia Pahang, Pekan 26600, Malaysia

^b Automotive Excellence Center, University Malaysia Pahang, Pekan 26600, Malaysia

Received MARCH, 13, 2016

Accepted APRIL, 1, 2017

Abstract

Painting process is critical in the manufacturing process of commercial vehicle to provide both protection and decorative elements. Good quality coating is important to reduce cost and concurrently achieve customer satisfaction. A systematic approach and applications of the basics and advanced management tools and techniques are used to improve the quality of the coated body. One of the proposed approach is to utilise the PDCA-cycle to reduce the defects on the electrodeposited body. In the present study, the bits defect on the electrodeposited automobile bodies is investigated. Within the multilayer coating on bodies, the iron filing leads to the bits defect that appears on the electrodeposited coating surface. The iron filings arised from the metal assembly process carried out in the bodyshop, remained on the body during the painting process in paint shop. The defected surface can be removed through the process of sanding which is high in cost and requires extensive production time. Therefore, the best method to prevent the bits defects is by removing or reducing the iron filing through filtration, magnetic separation and surface adjustment process. The implementation of filtration system, magnetic separation and surface adjustment process improved 36% of bits and reduced 42% of sanding man hour with a total saving of RM40.00 per unit.

© 2017 Jordan Journal of Mechanical and Industrial Engineering. All rights reserved

Keywords: *electrodeposition, defect, quality improvement, PDCA.*

1. Introduction

The goal of the painting process in the commercial vehicle assembly is to provide a uniform coating for protection and decorative purposes. Therefore, to successfully achieve the goal of painting, the process is segmented into a number of parts. These parts, or 'layers', are applied in a specific order and although the function of each 'layers' are unique, somehow there is interaction between the parts to achieve the desired balance of properties [1]. The multilayer coatings in the current technology include pre-treatment, electrodeposition (ED) primer, primer surfacer and wet on wet technology of top coat that consists of both base coat and clear coat. The functions of multi layers coatings are corrosion protection for primers, smoothness and chip resistances for primer surfacers, and colour and weather resistances for the final top coat.

The processes that carried out in the paint shop are pre-treatment and ED, sealing, ED sanding, primer coating, primer sanding and top coating. The pre-treatment of car bodies manufactured using differen metals critically require the state of the art corrosion protection and also provides the best adhesion for electrodeposition coating.

The ED process is a special coating method where the ED paint that is dispersed in water is electrically deposited on the surface of substrate to form a uniform and water-insoluble film. The primary process for ED is electrolysis [2], [3]. The fundamental aspect of ED is reported by Beck [4], whereby the ED process forms a uniform coating on the bodies for protection of corrosion. There are two types of electrodeposition processes, namely anodic and cathodic electrodeposition. The anodic ED relies on carboxyl groups, while the cathodic relies on amine groups. The disadvantages of anodic system is that it induces some dissolution to the metal ions of the parts that being coated. As a result, the resistance towards corrosion obtained coatings is limited and discoloration can occur due to the presence of the iron in the anodic films. On the other hand, cathodic ED was developed back in 1970s with several advantages, including high throwing power, superior corrosion protection, and virtually no absence of dissolution of metal occurring on the coated articles [5].

The ED process started with pre-treatment stage, namely are pre-cleaning, pre-degreasing, degreasing, water rinsing, surface conditioning, phosphating, final water rinsing and deionized water rinsing. After the pre-treatment stage, the ED process takes place; it includes ED, ultrafiltration and final deionized water rinsing. After

* Corresponding author e-mail: nabiilah.abraham@gmail.com.

the ED process, the coated unit is dried through oven baking process.

1.1. Quality improvement

A poorly cleaned body contributes negatively to the quality of the electrodeposited body. It is commonly known in the automobile industry that, many surface defects arise from the poorly cleaned surface after the ED process. As a solution, the defected surface on the body is required to be removed by sanding process before proceeding to next coating process which is the primer coating. Since the process of sanding is costly, it is very important to provide a good quality surface of the electrodeposited body. The good quality surface can be achieved by reducing the defects during the ED process. The common defects of the electrodeposited surface are bits, pinhole, cissing, sludge, grind mark and line mark. Due to the criticalness of having the defects, many studies have been conducted on the applications of reducing defects in automotive painting process.

One of the major defect from ED process is the bits. Accumulation of remaining particles within dipping tank is the root cause for producing the bits. Removal of these particles is possible by utilizing a set of a micro hydro cyclons combined with pressurised paper band filters and magnetic separation [6]. The commonly used method in the industry for the filtration system of pre-treatment and ED is by inserting the filter bag inserted into the filter housing for the particle removal. Standard filter types is the bag filters with particle retention ability of up to 25 or 50 μm . The polypropylene material in a needle is the common filter material. The filter bags are normally placed in a stainless steel basket, followed by placing this basket in a stainless steel filter vessels where the numbers of baskets could be between two and eight within a vessel. Thereafter the paint flows from top to bottom under pressure, however maintained as low as possible for best filtering effect. For best results, the filters are flushed and cleaned every week. Any damage filter can be identified by monitoring the pressure differences between the input and the output of the filter cartridges. The operation of the filter bag must stopped in the case of the presence of heavy particles and consequently the filter bags have to be replaced. The filter bags should be replaced to the coarser mesh-size that is $> 100\mu\text{m}$. The performance of the bag filter can be enhanced significantly by innovatively applying magnetism concept through the magnetic pre-filters [7]. An innovative novel filter is introduced due the inefficiency of the filter bag [8]. In the case of improving the defect that is occurring from the characteristic of the structure, the optimal location of supporting bonnet structure of automobile bodies was studied [9]. The quality problems frequently occurred due to accumulated dirt that supposed to be cleaned with cleaning agents. As a solution, the implementation of ON/OFF confirmation logic control based spray was carried out to ensure that the body passes through proper cleaning process [10].

The PDCA-cycle is a dynamic model and an intergral part of the process management which is designed to be used as a dynamic model because one cycle represents one complete step of improvement [11]. In order to coordinate the continuous improvement effort, the PDCA-cycle is

utilized. In the plan-stage the problem is identified using Pareto-chart and subsequently the root cause is analysed through cause and effect diagram. The Pareto-chart a special type of bar charts in which the categories of responses are listed on the X-axis, the frequencies of responses (listed from largest to smallest frequency) are shown on the left side Y-axis, and the cumulative percentages of responses are shown on the right side of Y-axis. The cause and effect diagram is a tool used to organize the possible factors that could be negatively impact the stability, centre, spread, and shape of a critical to quality (CTQ) characteristics measure [14]. A brainstorming session is conductor to identify the main rootcause item [13]. Following to that, in the do-stage the implementation of the filtration and magnetic separation, there will be measurement on the effect of the implementation in the check-stage. Finally in the act-stage, the results of the implementation is interpreted and the PDCA-cycle is restarted again to sustain and improve process further.

2. Problem Analysis

In the plan-stage the major problems are analysed based on the collected data on defects occurred after the ED process, where these defects are detected on the coated surface after the baking process through visual inspection. In more details, the bright lights and the associate reflections measured through visual inspection are used for locating and evaluating any defects. Some of the defects found are bits, grind mark, rough surface, line mark, sludge, pinhole, mapping mark and sanding mark. As a method to identify the main problem, the defects are plotted in a chart as depicted in Figure 1. Based on the chart, it can be observed that the main problem is the bits that accounts for 93 % of the overall defects.

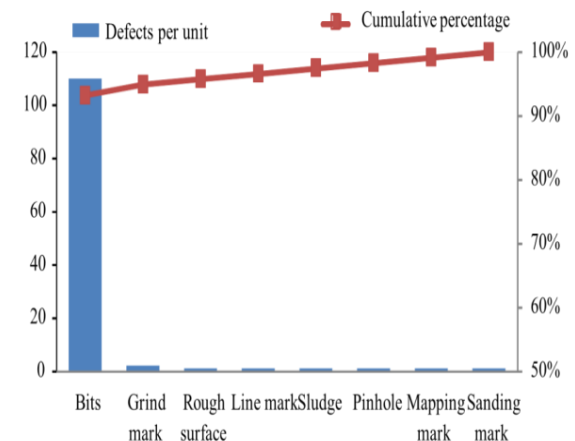


Figure 1. The electrodeposition defects

Therefore, bits are selected as the main defects that critically requires a solution. Bits are basically foreign materials that are found to be sticking on the coated surface. By using microscope, the bits can be observed to be iron filing, phosphate bits and electrodeposition paint bits. In terms of characteristics, the shining and rusty particles are the iron filings and the whitish and powdery particles are both the phosphate bits and ED bits as depicted in Figure 2.

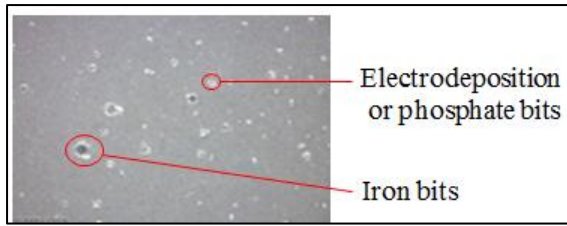


Figure 2. Depiction of bits

Defects categorizations based on percentile are shown in Figure 3 where the highly occurring bit defect is iron filing with up to 55% of occurrence bit.

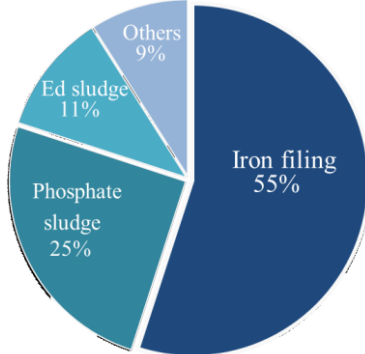


Figure 3. Bits categorization chart

The iron filings originate from the body assembly process at the Body shop, where the process consists of spot welding, welding, grinding, and sanding process of the assembly of the metal part. The actual iron filings found on the body in white is shown in Figure 4.

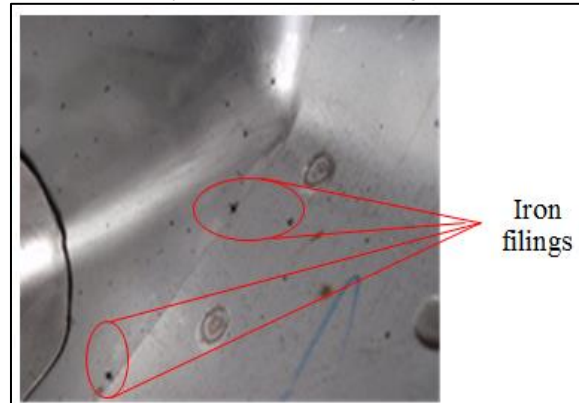


Figure 4. Iron filings on body in white

The root cause of bits is analysed by using Ishikawa diagram as shown in Figure 5. The analysis is divided into four main factors, namely man, method, machine and material.

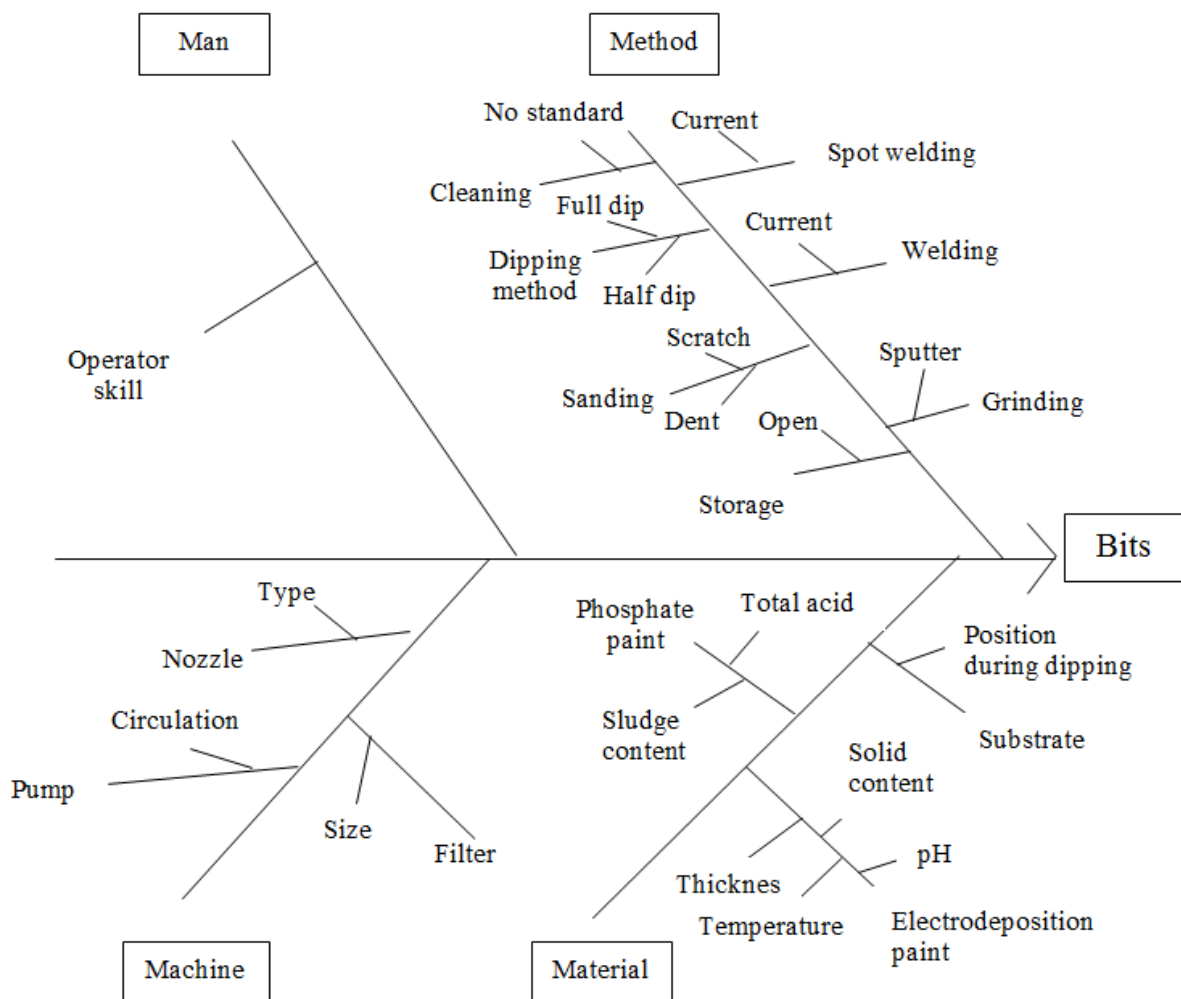


Figure 5. Bits rootcause analysis

2.1. Rootcause through Man

In terms of the man factor, an operator's skill towards spot welding, welding, grinding, and sanding process directly influence the defect volume of the iron filing. The operator's skill is controlled by a skill chart and is evaluated each month. However, specially for the welding operation, only a certified skilled operator is allowed to perform the welding process.

2.2. Rootcause through Method

The processing methods in a Body shop that produces the iron filings are spot welding, welding, sanding and grinding. The spot welding and welding processes are the steps taken to assemble the metal parts to build a complete body. Additionally, during the assembly process both spot welding gun and welding machine are used and followed by grinding process through portable hand grinder to grind the sputter that are produced during the spot welding process. Finally, in order to

produce a smooth and good surface for the subsequent painting process, defects including dent and scratches on unit are smoothed by using the sanding machine. The methodologies for removing iron filings in every processes are discussed. In the case of iron filing reduction in spot welding process and welding process is conducted by periodical checking of the current parameter once in every three months. For the sanding and grinding processes, the defects including sputter, dent, and scratch are controlled. Furthermore, a cleaning method is established to clean the body to clear off the iron filings before delivery to paint shop. The body is then vacuumed with high pressure vacuum and cleaned with sew rag and subsequently stored at the White Body Storage (WBS) area. In order to prevent the accumulation of iron filing inside body during storage in WBS, the buffer quantity at WBS is controlled. However, there are still iron filings remaining on the body which are carried over to the paint shop. Some of the remaining iron filings on the body may settle inside the dipping tanks during the pre-treatment and ED processes. The dipping methods are half dip or full dip. Therefore, it is very important to note that minimising the iron filings at the body shop stage itself is critical to reduce any accumulated defetcs that are carried over to the paint shop.

2.3. Rootcause through Machine

Some of the the machine used in the processes are inclusive of filter, pump and nozzle. The iron filings removal inside a tank depended on the filter size and number. The left over foreign materials must be reduced through this filtration system. In the case of the pump, the

workabilities of spraying pump and circulation pump are involved. The spraying nozzle type determined the spraying efficiency on the body whereas the spraying angle ensured the nozzle is sprayed at the correct angle to remove the iron filings on the body.

2.4. Rootcause through Material

The substrate, ED paint and phosphate paint are material factors that contribute to the bits. The paint formula, bath paint and pigment particle size within ED paint that leads to the generation of bits. The paint formula is the paint formulation that include resin composition, ash content and additive. For bath paint, the contents that contribute to defect are solid content, pH and bath temperature. These parameters are unequivocally controlled according to the standard specifications provided by the paint supplier. Furthermore, the paint supplier would provide weekly reports of the parameters control. The grinding condition affect the pigment particle size where the phosphate paint factors are in the form of sludge and crystal sized. The phosphate sludge is generated after the chemical reaction with body and is filtered through filtration system. Besides, the substrate position during the dipping also influenced the bits count on units.

For initial countermeasure, it is proposed to remove the iron filings inside the dipping tank by filtration system and magnetic separation. In filtration system, smaller sized filter is used to trap the iron filing, while magnet bar utilized in magnetic separation to attract the iron filings. By applying these two countermeasures, the amount of iron filings inside the dipping tank is expected to be reduced.

3. Experimental condition

In the first cycle of do-stage cycle, a filtration system is installed in the dipping tank to trap the iron filings within the dipping tank itself. There are ten dipping tanks for the Pre-treatment and ED processes. The filters are installed in the Pre-treatment tanks that consist of both circulation and spraying systems. The circulation system is used for the liquid circulation inside tank where the body is dipped into, where else, the spraying system is located in upper portion of the spraying tank to rinse the body after the dipping process. The size and quantity of the filters installed in the tanks are described in Table 1. The filter bags are placed in the stainless steel basket and together positioned inside the stainless steel filter vessel. In the filter bag, there are magnets with 9000 gauss strength to capture the iron filing through magnetic separation method.

Table 1. Filter quantity and size for according to tank functional areas

Tank No and Name	Spraying filter		Circulation filter	
	Quantity (unit)	Filter size (micron)	Quantity (unit)	Filter size (micron)
1- Pre degreasing	2	25	8	50
2- Degreasing	2	25	8	50
3- Water Rinse 1	2	25	3	50
4- Surface Conditioning	2	25	3	50
6- Water Rinsing 2	2	25	3	50

The material of the filter is based on the nylon, which can be washed and re-used for repeatable filtrations. The complete filtration system is shown in Figure 6.

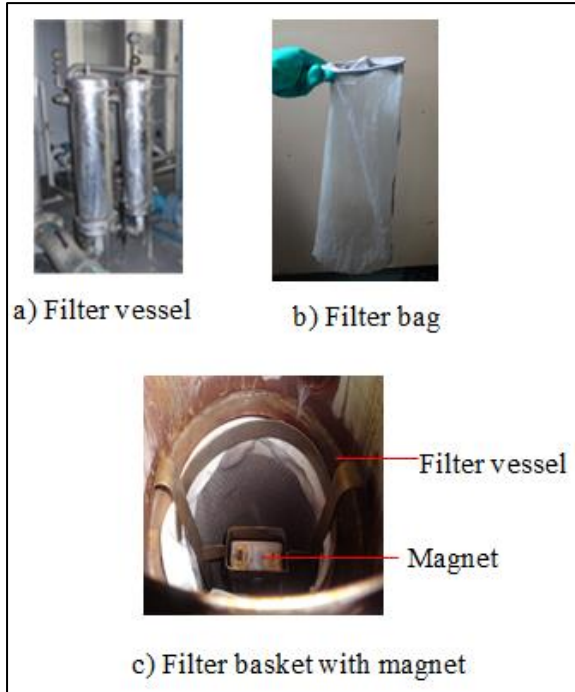


Figure 6. Filtration system with filter bag and magnet

In the second cycle of do-stage, the position of the bonnet is changed by modifying the bonnet stand, where the bonnet stand is designed to hold the bonnet during the ED process. The specification of the bonnet stand is modified from 315 mm to 730 mm in length, while its position is adjusted from 25° to the highest, 70°. Figure 7 (a) shows the position prior to the bonnet adjustment and Figure 7 (b) shows the bonnet position after the adjustment. Finally, the bits count on the bonnet area is measured after the oven baking process.

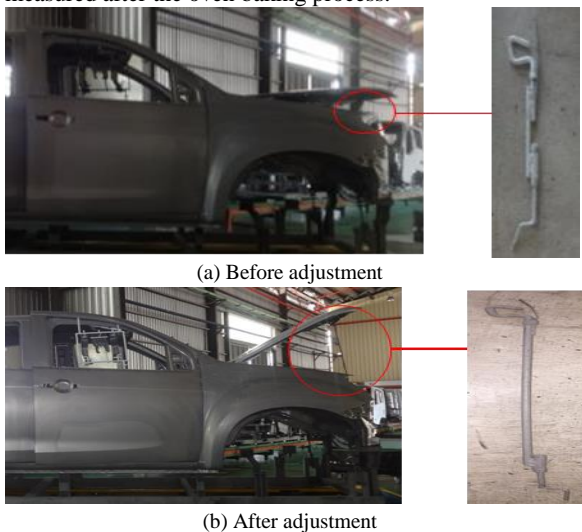


Figure 7. Repositioning of the bonnet

4. Results and Discussion

The iron filings are trapped inside the filter after the installation of the filtration system. The trapped iron filing inside filter bag is shown in Figure 8.



Figure 8. Iron collection inside the filter bag

The quantity of the bits on the coated surface is shown in Figure 9. The amount of bits that can be seen and felt by hand are counted in a 100 millimetres square outside of the coated body. The measurement is taken at the three surface areas, namely roof surface, bonnet surface and door surface. The bits count before the experiment are recorded and presented as depicted in Figure 10. The bits counts on the roof surface, bonnet surface and door surface are 58, 45, and 7, respectively. Most of the bits are accumulated on the roof area as compared to door and bonnet due to the difference in the surface orientation. The roof is in horizontal orientation, while the bonnet is 25° and the door is in vertical orientations.

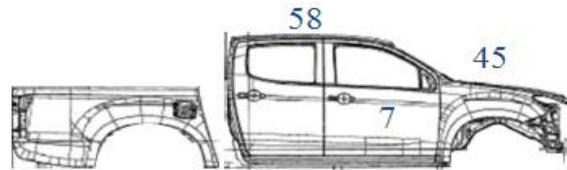


Figure 9. Bits counts on the unit before the experiment

The bits counts are improved 25%, 27%, and 29% at the roof, bonnet and door surfaces, respectively, after the filtration system and magnetic separation. Details of bits counts comparison before and after the installation of filtration and magnetic separation methods are illustrated in Figure 10.

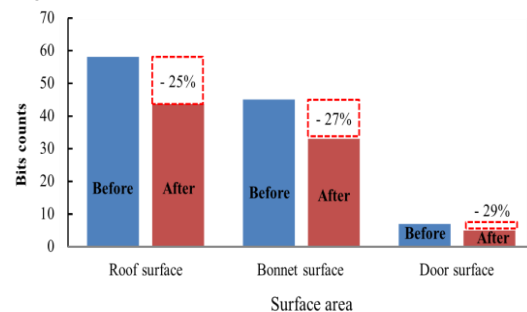


Figure 10. Comparison of bits counts before and after filtration and magnetic separation

Before the application of the filter, iron filing size in the range of more than 125 μm was found on the coated surface. However, with the filter application, the size of iron filing detected on the surface area became much smaller to only 56 μm . The filter is effective in trapping the iron filing that is size bigger than 56 μm . The iron filings that sized more than 125 μm escaped and less than 56 μm remained and stucked onto the unit. The size of the bits is identified by microscope as shown in Figure 11.



a) Before (125 μm) b) After (56 μm)

Figure 11. Bits size on the unit

Since the bits count on the vertical area is very low, the PDCA cycle two is conducted and implemented by slanting the vertically positioned bonnet. To reduce the bits on the bonnet surface, the bonnet position was shifted from 25° to 70°. The adjustment of the bonnet position improved the bits counts on the bonnet surface by 34% as illustrated in Figure 12.

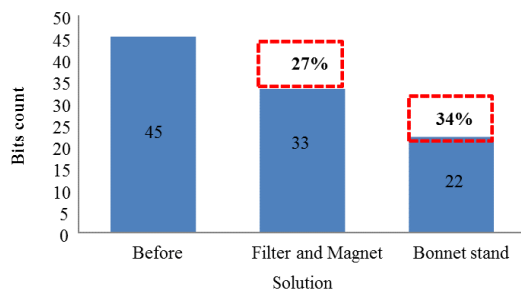


Figure 12. Bits count on unit after bonnet adjustment

By the implementation of the new bonnet stand, another quality problem related to the ED process was improved, which is the air pocket issue. The air pocket is formed due to the air trapped at the inner part during the coating process. The surface area with air pocket exposes the surface area to corrosion due to not having ED paint on that surface area. There is no formation of air pocket found after changing the bonnet position. The bonnet's inner surface area with the air pocket formation is shown in Figure 13 (a) and the bonnet inner surface area without the air pocket formation is shown in Figure 13 (b)

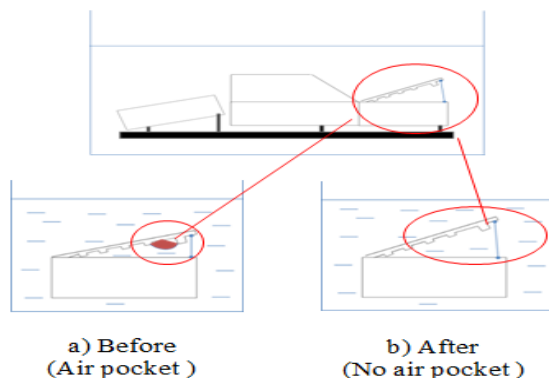


Figure 13. Bonnet's inner surface comparisons after bonnet adjustment

By applying the filtration and magnetic separation methods into the dipping tank, the rework activity of sanding on the surface area was reduced. Therefore, the man hour, manpower and sanding disc consumption are reduced. The reduced items are illustrated in Table 2. The man hour is reduced from 0.45 to 0.26, while the manpower is reduced from 8 persons to 6 persons. The sanding disc consumption for sanding activity is also reduced from 8 to 5 pieces per unit. By translating these figures into cost, this activity contributes to the saving of RM 3.00 on sanding disc consumption and RM 37.00 on man hour cost.

Table 2. The reduced items before and after the countermeasures

Item	Before	After
Manpower	8 persons	6 persons
Man hour	0.45	0.26
Sanding disc consumption	8 pieces	5 pieces

5. Conclusion

The main defect of the electrodeposited surface was the generation of bits. The major contribution of the bits was iron filing that was generated from welding, sanding, grinding, and spot welding processes at body shop during the metal assembly process. The iron filings were carried over to paint shop and accumulated inside the dipping tank. By introducing the filtration and magnetic separation methods into the pre-treatment system resulted in being successfully reducing the iron filing inside the tank. Through the proposed method, the number of bits improved by reducing up to 25%, 27%, and 25% on roof surface, bonnet surface and door surface, respectively. The number of bits is further reduces by 34% after the adjustment of the bonnet stand. The average number of bits reduced was by 36%. In the perspective of the operational expenditure, the sanding man hour used to improve the electrodeposited surface is reduced by 42% with a total saving of RM40.00 per unit.

Acknowledgement

The authors would like to thank Automotive Excellence Center, University Malaysia Pahang for providing the research grant to conduct the present study successfully. This research is funded by University Research Grant RDU1403128 through Automotive Excellence Center, UMP.

References

- [1] D. A. Ansdell, Automotive paints. In: R Lambourne, T A Strivens, editors. Paint and Surface Coatings: Theory and Practice, Woodhead Publishing ; 1999, p. 411-491
- [2] Y. Oyabu, N. Furuno, Y. Hirasawa, and H.Omori, "Electrodeposition coating process for automobile bodies". Transaction. Iron Steel Inst. Japan, Vol. 23, No. 994,1983, 994-1008.
- [3] K. Bewilogua, G. Brauer, A. Dietz, J.Gabler, G. Goch, B. Karpuschewski, and B.Szyska, "Surface technology for automotive engineering". CIRP Annall - Manufacturing Technology, Vol. 58, 2009, 608-627.

- [4] F. Beck, "Fundamental aspects of electrodeposition of paint". Progress Organic Coatings, Vol. 4, 1976, 1–60.
- [5] I. Krylova, "Painting by electrodeposition on the eve of the 21st century". Progress Organic Coatings, Vol. 42, 2001, 119–131.
- [6] H. J. Streitberger and K. F. Dossel. Automotive Paints and Coatings. 2nd ed Weinheim: Wiley VCH; 2008.
- [7] A. Bennett, "Automotive: Innovative filtration applications in the auto industry". Filtration Separation, Vol. 47, No. 1, 2001, 28–31.
- [8] P. Paul, "Filtration System Improves Performance of Pre-Treatment and Electrodeposition Stages of an Automotive Assembly Plant". SAE Tech. Paper, 2007.
- [9] J. Kim, E. Yim, C. Jeon, C. Jung, and B. Han, "Prediction and minimization of micro deformation on automobile hood after dipping process". International Journal of Automotive Technology, Vol. 16, No. 2, 2015, 293–300.
- [10] M. P. N. Shinde, "Interlock in Software in CED Paint Shop for Cost and Quality Improvement". International Journal of Engineering Research Technology, Vol. 4, No. 02, 2015, 719–725.
- [11] M. Soković, J. Jovanović, Z. Krivokapić, and A. Vujović, "Basic quality tools in continuous improvement process". Strojniski Vestnik/Journal Mechanical Engineering, Vol. 55, 2009, 1–9.
- [12] R. H. Fouad and A. Mukattash, "Statistical Process Control Tools: A Practical guide for Jordanian Industrial Organizations". Jordan Journal of Mechanical and Industrial Engineering, Vol. 4, No. 6, 2010, 693–700.
- [13] N. Mandahawi, R. H. Fouad, and S. Obeidat, "An application of customized lean six sigma to enhance productivity at a paper manufacturing company". Jordan Journal of Mechanical and Industrial Engineering, Vol. 6, No. 1, 2012, 103–109.

Numerical and Theoretical Analysis of a Straight Bevel Gear Made from Orthotropic Materials

Haidar Fadhil AL-Qrimli ^{*a}, Ahmed M. Abdelrhman ^a, Karam S. Khiled ^b

^a Department of Mechanical Engineering, Curtin University of Technology, Miri, Sarawak, CDT 250, 98009, Malaysia

^b Department of Mechanical Engineering, Ibra College of Technology, Ibra, Sultanate Oman

Received MARCH, 19, 2016

Accepted NOV, 10, 2016

Abstract

The purpose of the present study is to present a clear fundamental thought for designing and investigating straight bevel gear made of composite material. Application of composites in modern engineering includes gear-drive components, such as robotic arms, and this is especially evident when metallic gears are incapable of coping with the vigorous requirements of the machines. The presentwork demonstrates an actual form of the straight bevel gear that is made out into a set of equation rearranged and derived from the classical theory of gearing. The gear is then modeled using CAD commercial software in order to generate the whole gear in three dimension coordinates. This analytical calculation was constructed to allow us to calculate the straight bevel gear profile points, which are crucial for modeling and fabricating the composite gear model and to numerically analyze this model using finite element method. The results were extensively compared. This comparison attempted to study the composite bevel gear teeth problem. The focus in this work is on how much the divergence in behavior between orthotropic material and isotropic material such as steel can be reduced. The results prove the capability or potential for composite materials to be used as component materials in power transmission gearing in robotic arms applications.

© 2017 Jordan Journal of Mechanical and Industrial Engineering. All rights reserved

Keywords: Orthotropic Materials; Composite; Gear; Torque.

1. Introduction

Many researchers have studied and discussed the behavior of composite gears as a polymer matrix and glasses or graphite fiber, which named a Polymer Matrix Composite (PMC) used in engineering applications as gear due to their medium level strength and low density. Nozawa [1] studied the tribology of a metal spur gear and a hybrid gear, in order to reduce noise with greaseless metal gear and plastic gear with smaller rate of tooth failure. The test was at rotation speeds of 1000 rpm, and a torque range of 13–8 Nm. They discovered that the noise is suddenly amplified when a single polymer sheet was spontaneously removed from the gear's surface; this is probably due to its low adhesive strength against a shear. Kozo [2] investigated the effect of different types of composite material on the strength of plastic gears. They used glass and carbon fibers in the gear tooth surfaces as reinforcement in order to improve bending strength, epoxy resin as the matrix material. Experimental static and dynamic tests were carried out to evaluate the effect of fiber reinforcements, and it shows the reinforcement is effective in improving the strength of plastic gears.

Ezhil and Paul [3] reported on the corrosion characteristics of Al 7075/ basalt short fiber metal matrix composites as a function of percentage of reinforcement. The matrix Composites Al 7075 alloy demonstrated a

higher corrosion rate compared to MMCs under the corrosive atmosphere. Al-Shhyab and Ahmet Kahraman [4] studied the torsional dynamic behavior of a multi-mesh gear train and reported that, the torsional stiffness of the shaft is influencing the modal characteristics of the system and the nonlinear response.

In 2007, Melick [5] examined the effect of steel and plastic gear transmission with numerical and analytical methods by studying the influence of the stiffness of the gear material on the bending of the gear teeth, the consequences on contact path, load sharing, stresses and kinematics. Mao [6] carried out experimental investigations and modeled polymer composite (glass fiber reinforced nylon with PTFE). The design method is based on the relationship between polymer composite gears wear rate and surface temperature. A similar test was conducted on non-lubricated metal gears, and it was discovered that the polymer gear wear rate dramatically increased when the load reaches a critical rate for a specific geometry. Furthermore, Zhu and Li in 2011 [7] established a finite element model on a straight bevel gear by drilling holes in gears to reduce its weight. Nevertheless, they concluded that straight bevel gears with holes would weaken the mesh impact beneath the vibration compared to the normal straight bevel gear under the same loading and environment conditions [8]. Simon [9] presents an optimal tooth modification for a spiral bevel gear that improves

* Corresponding author e-mail: haidar.fa@curtin.edu.my.

load distribution and decreases the maximum tooth contact pressure.

Fiber reinforcement results in high specific strength and stiffness compared to metal matrix composite, depending on different types of fiber and their arrangement in the matrix when acting as laminates, which are mostly used in weight-sensitive industry gear applications, offering the highest specific strength and stiffness. Pihtili [10] investigated the wear resistance and behavior of woven glass fiber and composite materials under different loads, speeds and sliding distances. Antonio and Marcos [11] used a polyethylene terephthalate to replace a spur gear. The module of the spur gear equals to 2 mm/tooth, with a pitch diameter 34mm, and a pressure angle of 20° and the width of 18 mm. Enormous efforts have been made by previous investigators to relate tensile fillet stresses observed in statically and dynamically loaded gear teeth to the geometric appearance of the tooth. There is a number of approaches used in the past to verify the stresses and deflection in the gear's teeth, Wilfred Lewis made where the first effort to find the tooth root stresses. He based his analysis on a cantilever beam, and assumed that failure will occur at the weakest point of the beam, with him assuming it to be at the cross-section at the base of the gear. At the same time, Heinrich Hertz researched the contact pressures of the teeth, and his study was based on the elastic contact of two cylindrical bodies that determines the contact pressure between a gear and a pinion. With this tendency and experimental studies on bending stress analysis for the gears, the American Gear Manufacturers Association (AGMA) published their own standards based on Lewis's equation [12-15]. It is more accurate, and calculates all the geometrical factors, which are important in calculating the bending stresses for the gears. These geometrical factors take into account the loading position and the fillet radius tooth of the tip and base. Hasan [16] analytically studied the elastic-plastic stress analysis on an orthotropic rotating annular disc. The disc is made from metal matrix curvilinear reinforced steel fibers, and they used different angular velocities to enable them to see the separation of the plastic region. The results showed that the radial displacements and the plastic flow at the inner surface have higher values than those at the outer surface. Huali and Ahmet [17] proposed two dynamic models in order to study the interaction between a gear's surfaces wear and its dynamic response. Arafa and Megahed [18] constructed an FEA model of a spur gear to gather more information on the gear's mesh stiffness. The analysis involves quasi-static meshing conditions, where its compliance is evaluated at discrete meshing positions; with it assumed to be homogeneously isotropic. However, there are very few studies reported on a straight bevel gear by using different types of orthotropic material. In the present study, the theoretical and numerical methodologies are discussed. The theoretical results are compared to the numerical results. In the numerical stage we used finite element method to solve the gear tooth problem.

2. Methodology and Procedures

2.1. Theoretical procedure (Analytical Calculation)

The development of designing gear teeth is a bit arbitrary as far as the specific applications in which the gear is used to determine several design parameters. As stated in previously the basis for the bending stress analysis of gears was founded by Wilfred Lewis using his own formulation. His formulation for the bending stress started with the basis that a gear can be as basic as a beam which is subjected to tension and compression effects. However, this equation was not applicable to nearly all types of gears and not accurate because he didn't include the relevant geometrical parameters which influence the bending stress. As a result we used the AGMA standard 2005-D03, Design Manual for Bevel Gear Teeth. It is a design standard that illustrates all aspects of bevel gear tooth design, starting from the preliminary design standards and moving towards to complete the design and to be ready for analysis.

The torque application to a bevel gear mesh brings on tangential, radial, and separating loads on the bevel gear teeth. To make it easy, these loads are assumed to operate as point loads applied at the middle of the width gear tooth face, while only the tangential load is to be considered. The radial and separating loads are dependent upon the direction of rotation, pressure angle and pitch angle. The tangential loads (W_t), radial loads (W_r) and the separating loads (W_s) are defined as,

$$W_t = 2T / dp - F \sin \gamma \quad (1)$$

$$W_r = W_t (\tan \phi \sin \gamma) \quad (2)$$

$$W_s = W_t (\tan \phi \cos \gamma) \quad (3)$$

where dp is considered as the pitch diameter, T is the torque, F is the face width, γ is the pitch angle, and ϕ is the pressure angle. In the present study, we use a straight bevel gear with a ratio of 1:1 so the pitch diameter and the pitch angle are the same for the gear and the pinion. To calculate the pitch angle, we apply the equation: $\tan \gamma = \sin \epsilon / (1/i + \cos \epsilon)$ where; $\epsilon = 90^\circ$ for the straight bevel gear. Table 1 shows the gear parameters.

Design for pitting resistance is mainly administered by a failure form of fatigue on the gear teeth surface because of the influence of the contact stress between the mating gears. Design for bending strength ability is based on a failure form of breakage in the gear teeth caused by bending fatigue. Pitting resistance is allied to Hertzian contact (compressive) stresses flanked by the two mating gear teeth surfaces. The formulas were developed based on Hertzian theory of the contact pressure between two curved surfaces and load sharing between adjacent gear teeth as well as load concentration that might be a consequence from uncertainties in the built-up procedure. The contact stress is generally a function of the square root of the applied tooth load. The equation to calculate the compressive stress (pitting resistance) in a straight bevel gear tooth is given by:

$$\sigma_c = C_p \sqrt{Wt K_o K_v K_s \frac{K_m C_f}{d_p F I}} \quad (4)$$

where C_p is the elastic coefficient, Wt is the lateral tooth load, K_o is the overload factor, K_v is the speed factor, K_s size factor, F is gear face width, d_p pitch diameter, K_m load distribution factor, and I is the geometry factor. C_f is the surface condition factor has not been evaluated and it's always equal to 1. The elastic coefficient can be calculated by using the equation below:

$$C_p = \left[\frac{1}{\pi \left(\left(\frac{(1 - \nu_g^2)}{E_g} \right) + \left(\frac{(1 - \nu_p^2)}{E_p} \right) \right)} \right]^{\frac{1}{2}} \quad (5)$$

where E and ν stands for the Young's modulus and Poisson's ratio of the material correspondingly.

Bending strength capacity ratings in bevel gear teeth are developed using a simplified approach to cantilever beam theory. This method accounts for a variety of factors including: the compressive stresses at the tooth roots caused by the radial component of the tooth load; stress concentration at the tooth root fillet; load sharing between adjacent contacting teeth; and lack of smoothness due to low contact ratio. Calculating the bending strength rating determines the acceptable load rating at which tooth root fillet fracture should not occur during the entirety of the life of the gear teeth under normal operation. The basic equation for bending stress in a bevel gear is given by:

$$\sigma_b = Wt P K_v K_o K_m \frac{K_s}{F J} \quad (6)$$

Wt is the tangential load applied on the tooth as discussed previously, F symbolizes for the face width, K_s symbolizes for the size factor, K_m is the load distribution factor, and J is the geometry factor. P stands for the diametric pitch and can be calculated from equation (7):

$$P = \frac{\text{Number of teeth}}{\text{Pitch Diameter}} \quad (7)$$

The dynamic factor or velocity factor K_v , used in the calculation of the pitting resistance factor, accounts for quality of gear teeth while working at a particular speed and load conditions. It is typically influenced by design effects, manufacturing effects, transmission error, dynamic response, and resonance. In a broader sense, the velocity factor makes allowance for high-accuracy gearing, which requires low-accuracy gearing and, at the same time, makes allowance for heavily loaded gearing, which requires less derating than lightly loaded gearing. When gearing is manufactured using very harsh processes and controls, resulting in very accurate gearing, typical values of K_v between 1.0 and 1.5 are used. For our industrial gear application, K_v value of 1.3 is used. This value based on AGMA equations. The overload factor, K_o , accounts for quick peak loads that are much higher than the normal operating conditions. The overload factor (K_o) and load distribution factor are extremely qualitative in nature. For the load distribution factor, K_m , is a function of the rigidity of the mounting and reflects the degree of misalignment under load. It modifies the rating formulas in order to capture the non-standardized distribution of the load along the length of the gear tooth. The amount of the non-

uniformity of the load distribution (K_m) is a function of the gear tooth manufacturing accuracy, tooth contact and spacing, alignment of the gear in its mounting, bearing clearances, and face width of the gear teeth, and therefore all are considerations which affect the load distribution factor. Therefore, based on this current study for the straight bevel gear is supported by two ball bearings. The size factor (K_s) is a reflection of non-uniformity of material properties and is a function of the strength of the material. In addition to material properties, it depends primarily on tooth size, diameter of the part, face width, and ratio of tooth size to diameter of the part. The size factor can be quickly calculated using:

$$K_s = \frac{1}{p^{0.25}} \quad (8)$$

The geometry factor for resistance to pitting, I , evaluates the effects that the geometry of the gear tooth has on the stresses applied to the gear tooth. More in particular, it evaluates the relative radius of curvature of the mating tooth surfaces and the load sharing between adjacent pairs of teeth at the point on the tooth surfaces where the calculated contact pressure will reach its maximum value. The geometry factor may be calculated from. Successful minimization of this distance will result in the smoothest stress distribution across the gear tooth:

$$I = \frac{1}{r_1} + \frac{1}{r_2} \quad (9)$$

where r_1 and r_2 symbolized for the radius of the tooth surfaces curvature at the contact point and in the present study r_1 equals r_2 .

$$r = \frac{d_p \sin \phi}{2} \quad (10)$$

The geometry factor for bending strength (J) is also concerned with gear tooth geometry but it gives more consideration to the tooth shape and the concentration of the stress due to the root fillet geometric shape.

Table 1. Standard gear parameter

NO.	Design Parameter	Value	Options
1.	Pressure angle	20°	Material model
2.	Module	6	
3.	Face width	28.5m	Glasses/Epoxy
4.	Addendum	1m	Carbon/Epoxy
5.	Dedendum	1.25m	Jute/Epoxy
6.	Shaft angle	90°	Steel
7.	Root fillet radius	0.3m	
8.	Number of teeth	24	

2.2. Numerical Procedure (FEA)

The boundary conditions of any finite element problem need to be determined, and in the present work, the boundary conditions that we used are similar to what we do in the experimental phase. A torque is applied on one side of the gear, while all the points along the second gear are fixed in all the directions and have zero degrees of freedom. All the points and displacement in the first gear can move in the circumferential direction, which is the X-axis that we fixed the translation onto and make it rotate around while fixed in the radial directions (Y-axis=0, Z-

axis=0) in order to have five-degrees of freedom. The pinion is fixed in all six directions (DoF=0), while the load condition looks to be an external torque applied on the gear. The magnitude of the applied torque is (17640 N.m), which is used in the present work, and is equal to the tangential force of the gear's tooth surface (245N). The damping ratio in the gears does not seriously affect the dynamic stress, so it is considered to be 0.004, based on literature. The liner bulk viscosity and the quadratic bulk viscosity are taken as default, with values of 0.06 and 1.2, respectively. All the discussions are built on the standard parameter for a straight bevel gear shown in Table 1.

3. Results and Discussion

3.1. AGMA

The analysis begins with calculation of the gear loads generated by the bevel mesh. Using Equation 1, Equation 2, and Equation 3, the tangential load (W_t), radial loads (W_r), and separating load (W_s), are calculated. After solving the three equations, the values of the gear tooth loads are shown in Table 2. Once the design of the gear is verified and calculating the applied load of the teeth is carried out, the Hertz stresses calculation is performed in order to gauge the ability of the gear teeth to resist pitting.

Table 2. Calculated bevel gear tooth load

W_t (N)	245
W_r (N)	63.05
W_s (N)	63.05

Equation 9 is employed to calculate the geometry factor for pitting resistance (I), which is then used to find the value for compressive stress acting on the gear teeth. Calculation of the geometry factor involves solving Equation 10 to find the curvature tooth surfaces radius at the contact point. Once the geometry factor calculated, the other factors required to calculate the Hertz stresses could also be finalized. After calculating all the factors based on the AGMA standard, AGMA 2005-D03, Design Manual for Bevel Gears, the value of the Hertz stresses in the gear teeth were calculated using Equation 4 and the values are shown in Table 3.

3.2. Comparison between FEA model and Analytical Calculation

Static analysis calculates the effects of steady loading conditions on a structure can be determined using static analysis. It is still effective even if the dynamic effects

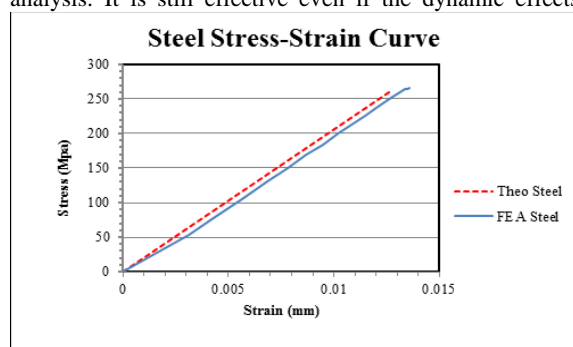


Figure 1. FEA and theoretical Stress Strain curve of straight bevel gear made from steel

caused by time and inertia are ignored. It is a simple analysis, wherein the effect of an immediate change in the model is calculated without taking into account the longer-term response of the model to that change. The main advantage of static analysis is the fact that it can discover initial errors in the material, which saves time and effort due to the fact that beginning dynamic analysis directly takes time and a considerable amount of skills. The static analysis is only the first step in solving a finite element problem, with the next step being the dynamic analysis. In FEA, static analysis means fixed and ignoring runtime environment, while dynamic means action and change. The dynamic analysis involves the testing and evaluation of a straight bevel gear, and we applied static analysis to determine the stress and strain of the tooth's surface of the straight bevel gear. 245N was applied on the tooth's surface of the gear to satisfy the static loading condition. The FEA results, obtained from the present study, are compared to the analytical calculation, along with the static behavior and stress strain curves. The stress-strain curves of the theoretical calculation and the finite element is drawn in the same Figure, in order to compare it to the Figures below. From the Figures below, it is clear that the curves have similar trends. The major reason is that we used the same gear dimensions and boundary conditions. The analytical calculation and the finite element results of the straight bevel gear, and the results between the two stages show a good match. The theoretical results show a linear behavior, while the finite element model of the steel shows nonlinearity. The values of the results are very close to each other, and we concluded that the FEA model is correct, and can be used for further simulation.

For the composite material model, we used engineering constrains in order to add the orthotropic mechanical properties for the glass/epoxy, carbon/epoxy and jute/epoxy. The parameters and conditions applied on the steel model used for the orthotropic models are similar, and it is assumed that the direction of the material is one direction in the finite element model. After running the simulation in the ABAQUS solver stage, the stress-strain behavior of the models was compared to the analytical calculation shown in the Figures below (Figure 2 to Figure 4), and the behavior of all the models shows good match with the theoretical phase. The results of the glass fiber are almost the same, and it is very near to the transverse direction results, similar for jute fiber, but the results of the carbon fiber model shows lower values than the analytical calculation. Its behavior, however, is the same.

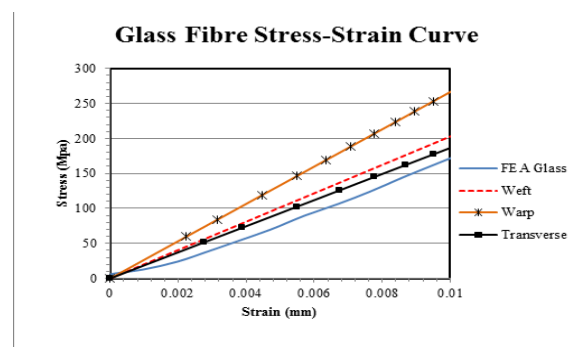


Figure 2. FEA and theoretical Stress Strain curve of straight bevel gear made from glass fiber

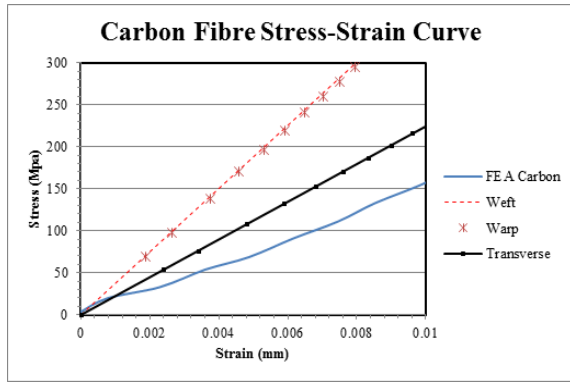


Figure 3. FEA and theoretical Stress Strain curve of straight bevel gear made from carbon fiber

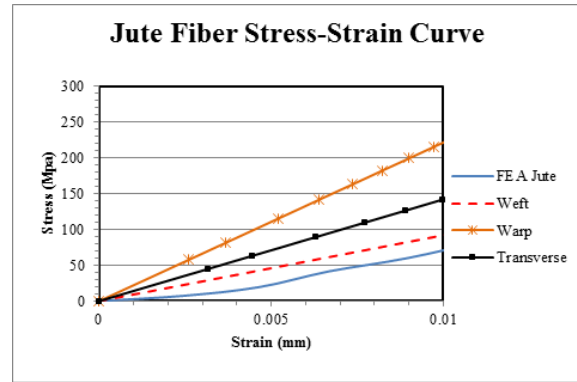


Figure 4. FEA and theoretical Stress Strain curve of straight bevel gear made from jute fiber

Table 3. Numerical and analytical results of the straight bevel gear for different type of materials

Stress/Material	Steel		Glass/Epoxy		Carbon/Epoxy		Jute/Epoxy	
	FEA	AGMA	FEA	AGMA	FEA	AGMA	FEA	AGMA
σ_1 (Mpa)	236.497	263.34	347.367	261.652	361.712	358.219	233.809	184.025
σ_2 (Mpa)				295.527		343.125		285.516
σ_3 (Mpa)				253.991		266.981		221.724

4. Conclusions

We derived an analytical model based on the AGMA standard, as has been discussed. We studied the standard straight bevel gear made of different type of materials (glasses/epoxy, Carbon/Epoxy, Jute/Epoxy and Mild steel) analytically by conventional approach. It considers the tooth as cyclic symmetry sector. We analyzed the stresses and deflection in a single point in the midpoint of the gear tooth surface where it is useful to verify the stresses and deflections that we determined and measured the present work. We studied the model numerically by running the straight bevel gear generation built using a commercial software to create points that describe the whole gear body, these points with composite mechanical properties are the input data for ABAQUS program to draw the bevel gear domain and contour the principle stresses inhabited in its teeth made of composite material, and draw the mode shape present due to the same load conditions. The validity of the FEM achieved by comparing its results (ABAQUS) for (steel, glass/epoxy, carbon/epoxy, jute/epoxy) with one analytical calculation load applied at the midpoint of the gear tooth surface. The comparison shows that there is a good agreement; therefore, the validity of the FEM is satisfied. Static stress analysis of these glass/epoxy, carbon/epoxy, jute/epoxy and mild steel materials gears are performed and their normal stresses in X, Y, Z directions are obtained. The same load of 245.25 N per mm length of face width of gear tooth was applied in all the cases.

Acknowledgments

The researchers would like to thank the Curtin University Sarawak for their financial support for the present work.

References

- [1] Jun-ichi Nozawa, Tadashi Komoto, Takahiko Kawai, Hiroyuki Kumehara, Tribological properties of polymer-sheet-adhered metal hybrid gear, *Wear*, Vol. 266, (2009). No.9, 893–897
- [2] Kozo Ikegami, Kenji Kikushima and Eiryō Shiratorit, Effects of Material Constitutions on the Strength of Fiber Reinforced Plastic Gears, *Composites Science and Technology*, Vol.27 (1986). No 1 .43-61
- [3] Ezhil Vannan, Paul Vizhian, Corrosion Characteristics of Basalt Short Fiber Reinforced with Al-7075 Metal Matrix Composites, *Jordan Journal of Mechanical and Industrial Engineering*, Vol. 9 (2015), No 2, 121-128.
- [4] Al-Shhyab and Ahmet Kahraman, A Nonlinear Torsional Dynamic Model of Multi-Mesh Gear Trains Having Flexible Shafts, *Jordan Journal of Mechanical and Industrial Engineering*, Vol 1 (2007), No 1, 31 – 41.
- [5] Dr. Ir H.G. H. van Melick, Tooth-Bending Effects in Plastic Spur Gears Influence on Load Sharing, Stresses and Wear, Studied by FEA, *Journal Gear Technology*, Vol.58 (2007). No. 10 .58- 66.
- [6] K. Mao, A new approach for polymer composite gear design, *Journal Elsevier B.V. Wear*, Vol. 262 (2007). No. 3. 432–441.
- [7] Hayrettin Duzcukoglu, Study on development of polyamide gears for improvement of load-carrying capacity, *Tribology International*, Vol. 42 (2009). No. 8. 1146–1153.
- [8] Xiaoyuan, Zhu, Fang Zongde, and Li Wei. "Research on vibration reduction performance of holey straight bevel gear." *Consumer Electronics, Communications and Networks (CECNet)*, International Conference on. IEEE, Xianning, China, 2011.
- [9] Vilmos Simon, Head-cutter for optimal tooth modifications in spiral bevel gears, *Mechanism and Machine Theory*, Vol. 44 (2009). No 7. 1420 – 1435.
- [10] Hasim Pihtili, An experimental investigation of wear of glass fibre–epoxy resin and glass fibre–polyester resin composite materials, *European Polymer Journal*, Vol. 45 (2009). No 1. 149–154,

- [11] Antonio F. A Vila and Marcos V. Duarte, A mechanical analysis on recycled PET/HDPE composites, *Polymer Degradation and Stability*, Vol. 80 (2003). No 2. 373–382.
- [12] Maitra, Gitin M. *Handbook of gear design*. 2nd ed Tata McGraw: Hill Education, 1994.
- [13] Eugene A. Avallone and Theodore Baumeister III, *Marks' Standard Handbook for Mechanical Engineers*, 10 th ed. MCGRAW-HILL: 1996.
- [14] T.A. Stolarsk. *Tribology in Machine Design*, 1 rst ed. Butterworth-Heinemann, 1990.
- [15] Peter Childs, *Mechanical Design*, 2nd ed, Elsevier Butterworth: Heinemann. 2004.
- [16] Hasan Callog lu, Muzaffer Topcu, Ali Rıza Tarakçılar, Elastic–plastic stress analysis of an orthotropic rotating disc, *International Journal of Mechanical Sciences*, Vol. 48 (2006). No 9. 985–990,
- [17] Huali Ding and Ahmet Kahraman, Interactions between nonlinear spur gear dynamics and surface wear, *Journal of Sound and Vibration*, Vol. 307 (2007).No 3. 662–679.
- [18] M H Arafa and M M Megahed, Evaluation of spur gear mesh compliance using the finite element method, *Journal of Mechanical Engineering Science, Part C*, Vol. 213 (1999). No 6. 569-579.

Chemical Reaction Effect on Unsteady MHD Flow Past an Impulsively Started Inclined Plate with Variable Temperature and Mass Diffusion in the Presence of Hall Current

U. S. Rajput * , Gaurav Kumar

Department of Mathematics and Astronomy, University of Lucknow, Lucknow, U.P, India.

Received JAN, 21, 2016

Accepted MAY, 7, 2017

Abstract

The present study is carried out to examine the combined effects of Hall current and chemical reaction on flow model. The model consists of unsteady flow of a viscous, incompressible and electrically conducting fluid. The flow is along an impulsively started inclined plate with variable wall temperature and mass diffusion. The magnetic field of uniform strength is applied perpendicular to the flow. The model contains equations of motion, diffusion equation and equation of energy. The Governing equations involved in the present analysis are solved by the Laplace-transform technique. The velocity profile is discussed with the help of graphs drawn for different parameters, like thermal Grashof number, mass Grashof number, Prandtl number, chemical reaction parameter, Hall parameter, the magnetic field parameter and Schmidt number. The numerical values obtained for skin-friction were tabulated. We found that the values obtained for velocity, concentration and temperature are in concurrence with the actual flow of the fluid.

© 2017 Jordan Journal of Mechanical and Industrial Engineering. All rights reserved

Keywords:

1. Introduction

MHD flow problems associated with heat and mass transfer plays important roles in different areas of science and technology, like chemical engineering, mechanical engineering, biological science, petroleum engineering and biomechanics. Such problems frequently occur in petrochemical industry, chemical vapor deposition on surfaces, cooling of nuclear reactors, heat exchanger design, forest fire dynamics and geophysics. The influence of magnetic field on viscous, incompressible and electrically conducting fluid is of great importance in many applications such as magnetic material processing, glass manufacturing control processes and purification of crude oil. Attia along with Ahmed [1] studied the Hall effect on unsteady MHD Couette flow and heat transfer of a Bingham fluid with suction and injection. Further, Attia [2] considered the effect of variable properties on the unsteady Hartmann flow with heat transfer considering the Hall effect. Effect of mass transfer on flow past an impulsively started infinite vertical plate with constant heat flux and chemical reaction was investigated by Deka *et al.* [3]. Chemically reacting MHD boundary layer flow of heat and mass transfer over a moving vertical plate with suction was investigated by Ibrahim and Makinde [4]. The effect of Hall current on the magneto hydrodynamic boundary layer flow past a semi-infinite fast plate was

studied by Katagiri [5]. Muthucumarswamy [6] considered effect of chemical reaction on a moving isothermal vertical surface with suction. Further, Muthucumarswamy along with Ganesan [7] investigated first order chemical reaction on flow past an impulsively started vertical plate with uniform heat and mass flux. Maripala and Naikoti [8] analyzed Hall effect on unsteady MHD free convection flow over a stretching sheet with variable viscosity and viscous dissipation. MHD oscillatory channel flow, heat and mass transfer in a physiological fluid in the presence of chemical reaction was developed by Misra and Adhikary [9]. Pop [10] investigated the effect of Hall current on hydromagnetic flow near an accelerated plate. Pop and Watanabe [11] further studied Hall effect on MHD boundary layer flow over a continuous moving flat plate. Viscous flow over a non-linearly stretching sheet in the presence of a chemical reaction and magnetic field was studied by Raptis and Perdakis [12]. Raptis and Kafousias [13] studied flow of a viscous fluid through a porous medium bounded by a vertical surface. The study of MHD flow past an impulsively started vertical plate with variable temperature and mass diffusion was done by Rajput and Kumar [14]. Further, Rajput and kumar [15] worked on effect of chemical reaction on free convection MHD flow through a porous medium bounded by vertical surface. Ziyauddin and Kumar [16] investigated MHD heat and mass transfer free convection flow near the lower stagnation point of an isothermal cylinder imbedded in

* Corresponding author e-mail: rajputgauravlko@gmail.com.

porous domain with the presence of radiation. Combined effects of radiation and Hall current on MHD flow past an exponentially accelerated vertical plate in the presence of rotation was studied by Thamizhsudar and Pandurangan [17]. Tripathy *et al.* [18] analyzed chemical reaction effect on MHD free convective surface over a moving vertical plate through porous medium. Earlier, we [19] studied unsteady MHD flow past an impulsively started inclined plate with variable temperature and mass diffusion in the presence of Hall current. The main purpose of the present investigation is to study the effects of chemical reaction on unsteady MHD flow past an impulsively started inclined plate with variable wall temperature and mass diffusion in the presence of Hall current. The results are shown with the help of graphs and table.

2. Mathematical Analysis

The geometrical model of the problem is shown in figure-A

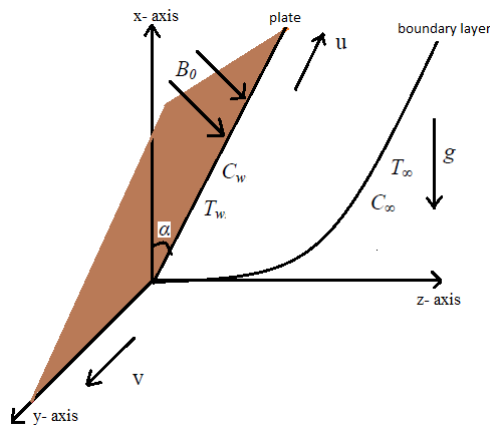


Figure A. Physical model

The x axis is taken along the vertical plane and z normal to it. Thus the z axis lies in the horizontal plane. The plate is inclined at an angle α from vertical. A transverse magnetic field B_0 of uniform strength is applied on the flow. The viscous dissipation and induced magnetic field was neglected due to its small effect. Initially it has been assumed that the plate and the fluid are at the same temperature T_∞ . Further, the species concentration is C_∞ everywhere in the fluid in stationary condition. At time $t > 0$, the plate starts moving with a velocity u_0 in its own plane and temperature of the plate is raised to T_w ; also the concentration level near the plate is raised linearly with respect to time. Due to the Hall effect there will be two components of the momentum equation. The flow model is as under:

3. Equations of motion

$$\frac{\partial u}{\partial t} = \nu \frac{\partial^2 u}{\partial z^2} + g\beta \cos \alpha (T - T_\infty) + g\beta^* \cos \alpha (C - C_\infty) - \frac{\sigma B_0^2 (u + mv)}{\rho(1+m^2)} \quad (1)$$

$$\frac{\partial v}{\partial t} = \nu \frac{\partial^2 v}{\partial z^2} + \frac{\sigma B_0^2 (mu - v)}{\rho(1+m^2)} \quad (2)$$

Diffusion equation

$$\frac{\partial C}{\partial t} = D \frac{\partial^2 C}{\partial z^2} - K_c (C - C_\infty) \quad (3)$$

Equation of energy

$$\rho C_p \frac{\partial T}{\partial t} = k \frac{\partial^2 T}{\partial z^2} \quad (4)$$

The initial and boundary conditions are

$$\left. \begin{aligned} t \leq 0 : u = 0, v = 0, T = T_\infty, C = C_\infty, \text{ for every } z, \\ t > 0 : u = u_0, v = 0, \\ T = T_\infty + (T_w - T_\infty) \frac{u_0^2 t}{\nu}, \text{ at } z=0, \\ C = C_\infty + (C_w - C_\infty) \frac{u_0^2 t}{\nu}, \\ u \rightarrow 0, v \rightarrow 0, T \rightarrow T_\infty, C \rightarrow C_\infty \text{ as } z \rightarrow \infty, \end{aligned} \right\} (5)$$

where u is the primary velocity, v - the secondary velocity, g - the acceleration due to gravity, β - volumetric coefficient of thermal expansion, t - time, m - Hall parameter, T - temperature of the fluid, β^* - volumetric coefficient of concentration expansion, C - species concentration in the fluid, ν - the kinematic viscosity, ρ - the density, C_p - the specific heat at constant pressure, k - thermal conductivity of the fluid, D - the mass diffusion coefficient, T_w - temperature of the plate at $z = 0$, C_w - species concentration at the plate $z = 0$, B_0 - the uniform magnetic field, K_c - chemical reaction and σ is electrical conductivity. Here $m = \omega_e \tau_e$ with ω_e - cyclotron frequency of electrons and τ_e - electron collision time.

The following non-dimensional quantities are introduced to transform equations (1), (2), (3) and (4) into dimensionless form:

$$\left. \begin{aligned} \bar{z} = \frac{z u_0}{\nu}, \bar{u} = \frac{u}{u_0}, \bar{v} = \frac{v}{u_0}, S_c = \frac{\nu}{D}, \mu = \rho \nu, \\ M = \frac{\sigma B_0^2 \nu}{\rho u_0^2}, \bar{C} = \frac{(C - C_\infty)}{(C_w - C_\infty)}, P_r = \frac{\mu C_p}{k}, \\ G_r = \frac{g \beta \nu (T_w - T_\infty)}{u_0^3}, K_0 = \frac{\nu K_c}{u_0^2}, \bar{t} = \frac{t u_0^2}{\nu}, \\ G_m = \frac{g \beta^* \nu (C_w - C_\infty)}{u_0^3}, \theta = \frac{(T - T_\infty)}{(T_w - T_\infty)} \end{aligned} \right\} (6)$$

The symbols in dimensionless form are as under:

\bar{u} - the primary velocity, \bar{v} - the secondary velocity, \bar{t} - time, θ - the temperature, \bar{C} - the concentration, G_r - thermal Grashof number, G_m - mass Grashof number, μ - the coefficient of viscosity, K_0 - the chemical reaction

parameter, P_r - the Prandtl number, S_c - the Schmidt number, M - the magnetic parameter.

The flow model in dimensionless form is

$$\frac{\partial \bar{u}}{\partial \bar{t}} = \frac{\partial^2 \bar{u}}{\partial \bar{z}^2} + G_r \cos \alpha \theta + G_m \cos \alpha \bar{C} - \frac{M(\bar{u} + m\bar{v})}{(1+m^2)} \quad (7)$$

$$\frac{\partial \bar{v}}{\partial \bar{t}} = \frac{\partial^2 \bar{u}}{\partial \bar{z}^2} + \frac{M(m\bar{u} - \bar{v})}{(1+m^2)} \quad (8)$$

$$\frac{\partial \bar{C}}{\partial \bar{t}} = \frac{1}{S_c} \frac{\partial^2 \bar{C}}{\partial \bar{z}^2} - K_0 \bar{C} \quad (9)$$

$$\frac{\partial \theta}{\partial \bar{t}} = \frac{1}{P_r} \frac{\partial^2 \theta}{\partial \bar{z}^2} \quad (10)$$

The corresponding boundary conditions (5) become:

$$\left. \begin{aligned} \bar{t} \leq 0 : \bar{u} = 0, \bar{v} = 0, \theta = 0, \bar{C} = 0, \text{ for every } \bar{z}, \\ \bar{t} > 0 : \bar{u} = 1, \bar{v} = 0, \theta = \bar{t}, \bar{C} = \bar{t}, \text{ at } \bar{z} = 0, \\ \bar{u} \rightarrow 0, \bar{v} \rightarrow 0, \theta \rightarrow 0, \bar{C} \rightarrow 0, \text{ as } \bar{z} \rightarrow \infty. \end{aligned} \right\} \quad (11)$$

Dropping bars in the above equations, we get:

$$\frac{\partial u}{\partial t} = \frac{\partial^2 u}{\partial z^2} + G_r \cos \alpha \theta + G_m \cos \alpha C - \frac{M(u + mv)}{(1+m^2)} \quad (12)$$

$$\frac{\partial v}{\partial t} = \frac{\partial^2 v}{\partial z^2} + \frac{M(mu - v)}{(1+m^2)} \quad (13)$$

$$\frac{\partial C}{\partial t} = \frac{1}{S_c} \frac{\partial^2 C}{\partial z^2} - K_0 C \quad (14)$$

$$\frac{\partial \theta}{\partial t} = \frac{1}{P_r} \frac{\partial^2 \theta}{\partial z^2} \quad (15)$$

The boundary conditions become

$$\left. \begin{aligned} t \leq 0 : u = 0, v = 0, \theta = 0, C = 0, \text{ for all } z, \\ t > 0 : u = 1, v = 0, \theta = t, C = t, \text{ at } z = 0, \\ u \rightarrow 0, v \rightarrow 0, \theta \rightarrow 0, C \rightarrow 0, \text{ as } z \rightarrow \infty. \end{aligned} \right\} \quad (16)$$

Writing the equations (12) and (13) in combined form

$$\frac{\partial q}{\partial t} = \frac{\partial^2 q}{\partial z^2} + G_r \cos \alpha \theta + G_m \cos \alpha C - qa \quad (17)$$

$$\frac{\partial C}{\partial t} = \frac{1}{S_c} \frac{\partial^2 C}{\partial z^2} - K_0 C \quad (18)$$

$$\frac{\partial \theta}{\partial t} = \frac{1}{P_r} \frac{\partial^2 \theta}{\partial z^2} \quad (19)$$

Finally, the boundary conditions become

$$\left. \begin{aligned} t \leq 0 : q = 0, \theta = 0, C = 0, \text{ for every } z, \\ t > 0 : q = 1, \theta = t, C = t, \text{ at } z = 0, \\ q \rightarrow 0, \theta \rightarrow 0, C \rightarrow 0, \text{ as } z \rightarrow \infty. \end{aligned} \right\} \quad (20)$$

Here $q = u + i v, a = \frac{M(1-im)}{1+m^2}$

The dimensionless governing equations (17) to (19) subject to the boundary conditions (20) are solved by the usual Laplace transform technique. The solution obtained is as under:

$$\theta = t \left\{ \left(1 + \frac{z^2 P_r}{2t} \right) \operatorname{erfc} \left[\frac{\sqrt{P_r}}{2\sqrt{t}} \right] - \frac{z\sqrt{P_r}}{\sqrt{\pi\sqrt{t}}} e^{-\frac{z^2}{4t}} P_r \right\},$$

$$C = \frac{e^{-z\sqrt{S_c K_0}}}{4\sqrt{K_0}} \left\{ \operatorname{erfc} \left[\frac{z\sqrt{S_c} - 2t\sqrt{K_0}}{2\sqrt{t}} \right] (-z\sqrt{S_c} + 2t\sqrt{K_0}) + e^{2z\sqrt{S_c K_0}} \operatorname{erfc} \left[\frac{z\sqrt{S_c} + 2t\sqrt{K_0}}{2\sqrt{t}} \right] (z\sqrt{S_c} + 2t\sqrt{K_0}) \right\}$$

$$q = \frac{e^{-\sqrt{a}z} A_{15}}{2} + \frac{G_r \cos \alpha}{4a^2} \{ z A_{11} + 2e^{-\sqrt{a}z} A_2 P_r + 2A_{14} A_4 (1 - P_r) \} + \frac{G_m \cos \alpha}{4(a - K_0 S_c)^2} [z A_{11} + 2A_{13} A_5 (1 - S_c) + 2e^{-\sqrt{a}z} A_2 S_c (1 - t K_0) - \frac{ze^{-\sqrt{a}z} A_3 K_0 S_c}{\sqrt{a}}] + \frac{G_r \cos \alpha}{2a^2 \sqrt{\pi}} [2zae^{-\frac{z^2}{4t}} \sqrt{t P_r} + \sqrt{\pi} A_{14} (A_6 + A_7 P_r) + \sqrt{\pi} A_{12} (az^2 P_r - 2 + 2at + 2P_r)] + \frac{G_m \cos \alpha}{4\sqrt{\pi} (a - K_0 S_c)^2} \left[\frac{e^{-\sqrt{K_0 S_c}} \sqrt{\pi} A_9 \sqrt{S_c}}{2\sqrt{K_0}} (S_c K_0 - az) + A_{13} \sqrt{\pi} A_{10} (S_c - 1) + e^{-\sqrt{K_0 S_c}} \sqrt{\pi} A_8 (1 - at - S_c + t K_0 S_c) \right]$$

The expressions for the symbols involved in the above equations are given in the appendix.

4. Skin Friction

The dimensionless skin friction at the plate is

$$\left(\frac{dq}{dz} \right)_{z=0} = \tau_x + i \tau_y.$$

The numerical values of τ_x and τ_y , for different parameters are given in table-1.

5. Results and Discussion

In the present paper, we studied the effects of Hall current and chemical reaction on unsteady MHD flow. The velocity profile for different parameters, like thermal Grashof number Gr , magnetic field M , Hall parameter m , chemical reaction K_0 , Prandtl number Pr , Schmidt number Sc and time t are shown in figures from 1.1 to 2.9. The concentration profile for different parameters, like chemical reaction, Schmidt number and time are shown in figures from 3.1 to 3.3. The numerical values of skin-friction are presented in Table-1. Due to gravity component $g\cos\alpha$, the fluid flows with higher velocity when plate is vertical as compared to flow when plate is horizontal. It is observed in figures 1.1 and 2.1 that the primary and secondary velocities of fluid decrease when the angle of inclination (α) is increased. From figures 1.2 and 2.2, we observe that if mass Grashof number is increased then the velocities got increased. From figures 1.3 and 2.3 it is deduced that when thermal Grashof number Gr is increased then the velocities are increased. If Hall current parameter m is increased then u is increased and v is decreased (figures 1.4 and 2.4). The influence of magnetic field on flow is observed from figures 1.5 and 2.5. It is seen that the effect of increasing values of the parameter (M) results in decreasing u and increasing v . It is in agreement since the magnetic field establishes a force which acts against the main flow resulting in slowing down the velocity of fluid. If K_0 the chemical reaction parameter is increased then the velocities are increased throughout the boundary layer region (figures 1.6 and 2.6). Further, it is observed that velocities decrease when Prandtl number is increased (figures 1.7 and 2.7). When the Schmidt number is increased then the velocities get decreased (figures 1.8 and 2.8). Further, from figures 1.9 and 2.9 it is observed that velocities increase with time. If reaction parameter and Schmidt number are increased then concentration is decreased (figures 3.1 and 3.2). Physically, the increase of Sc means decrease of molecular diffusivity (D). That is the process of diffusion will decrease. It is observed that velocities increase with time (figures 3.3).

Skin friction is given in table1. The value of τ_x increases with the increase in angle of inclination of plate, thermal Grashof number, and Hall currents parameter; and it decreases with angle of inclination of plate, mass Grashof Number, magnetic field, chemical reaction parameter, Prandtl number, Schmidt number and time. The value of τ_y increases with the increase in angle of inclination of plate, thermal Grashof number and the magnetic field; and it decreases with mass Grashof number, Hall current parameter, the chemical reaction parameter, Prandtl number, Schmidt number and time.

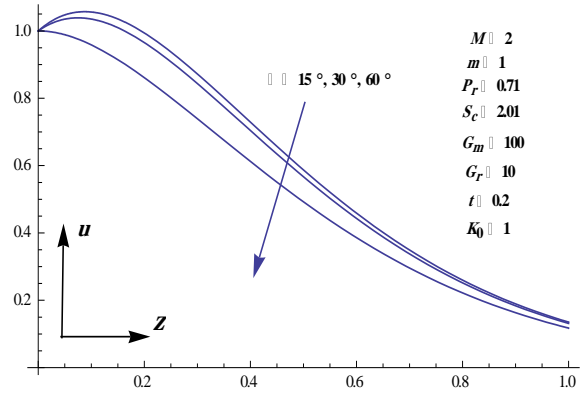


Figure 1.1: velocity u for different values of α

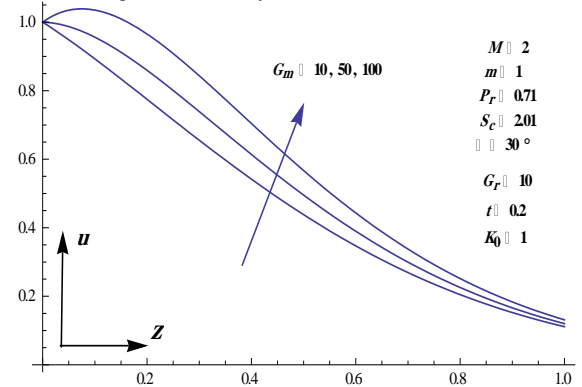


Figure 1.2: velocity u for different values of G_m

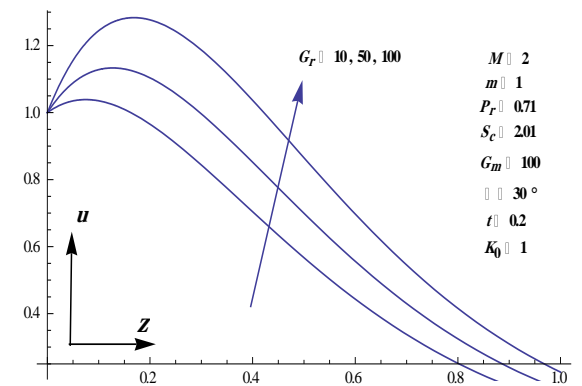


Figure 1.3: velocity u for different values of Gr

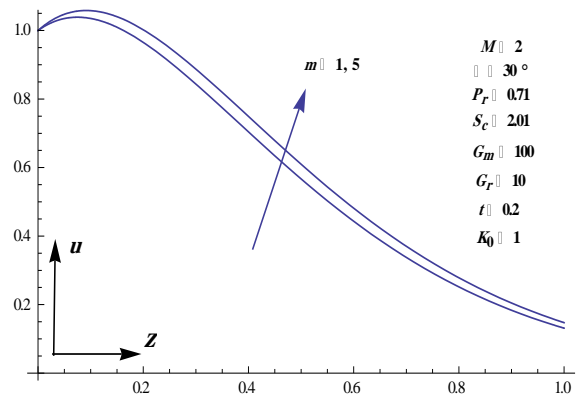


Figure 1.4: velocity u for different values of m

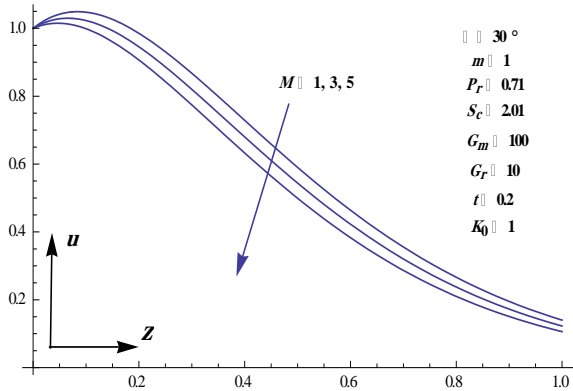


Figure 1.5: velocity u for different values of M

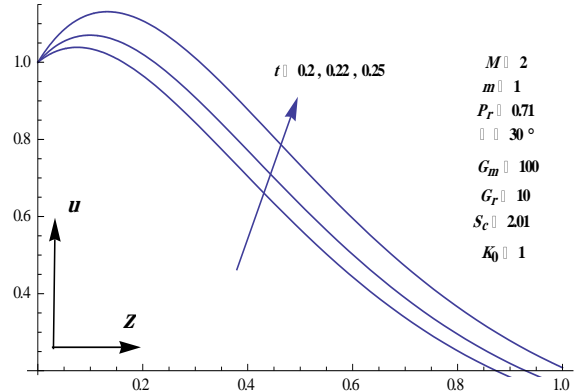


Figure 1.9: velocity u for different values of t

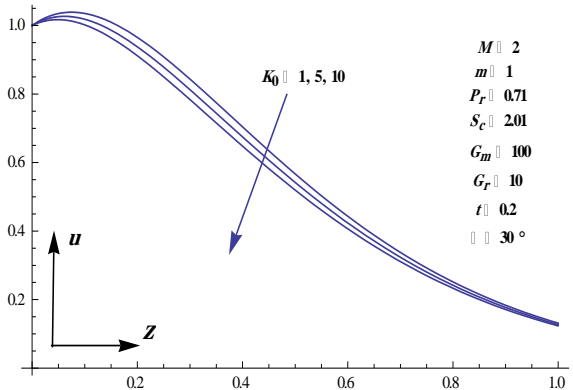


Figure 1.6: velocity u for different values of K_0

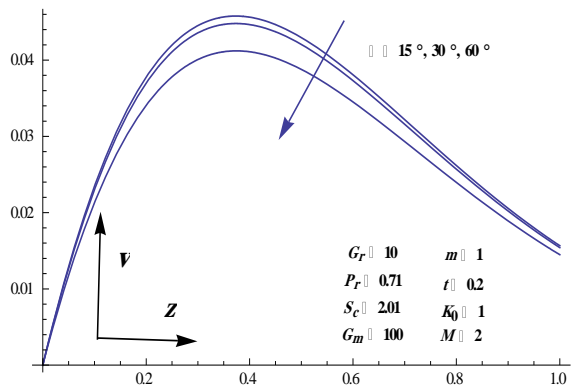


Figure 2.1: velocity v for different values of α

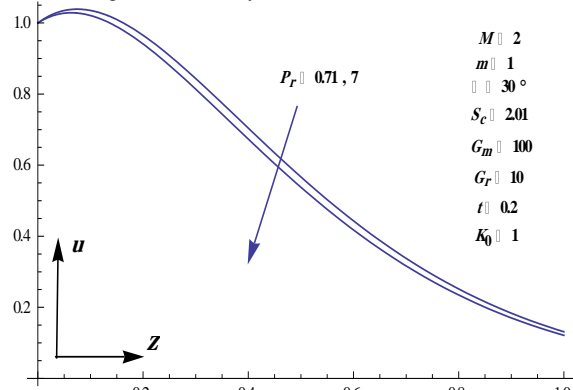


Figure 1.7: velocity u for different values of P_r

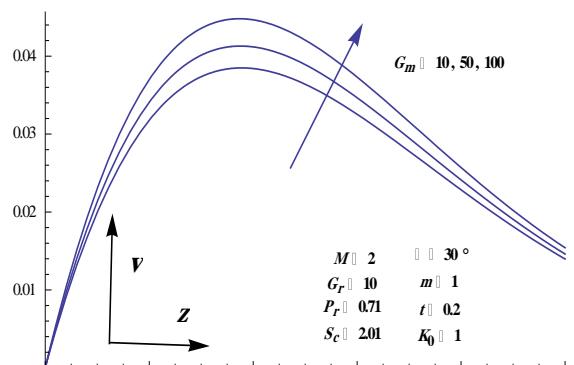


Figure 2.2: velocity v for different values of G_m

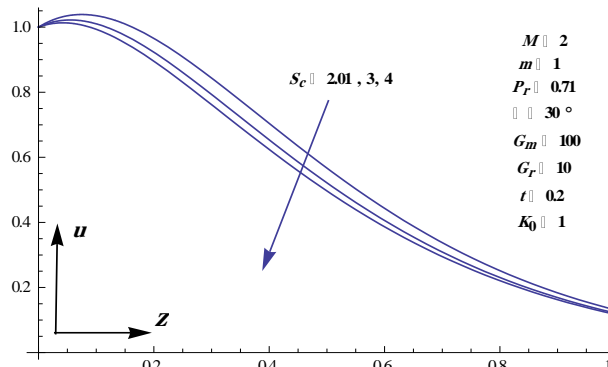


Figure 1.8: velocity u for different values of S_c

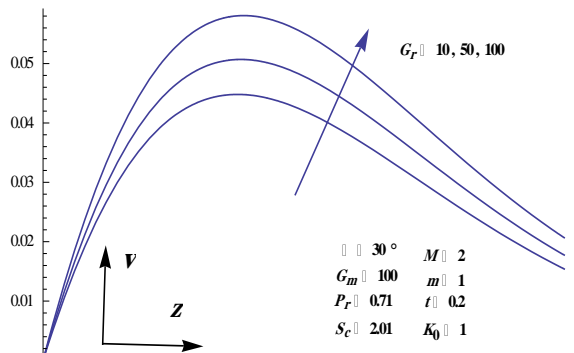


Figure 2.3: velocity v for different values of G_r

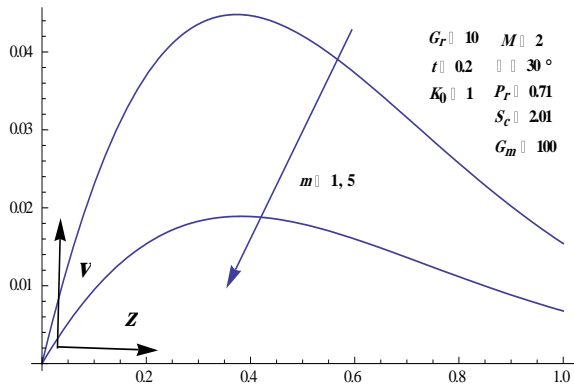


Figure 2.4: velocity v for different values of m

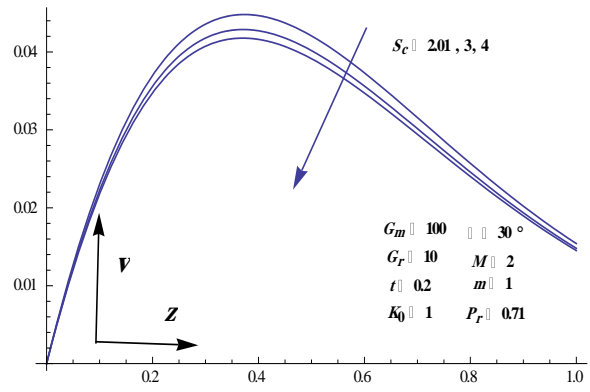


Figure 2.8: velocity v for different values of Sc

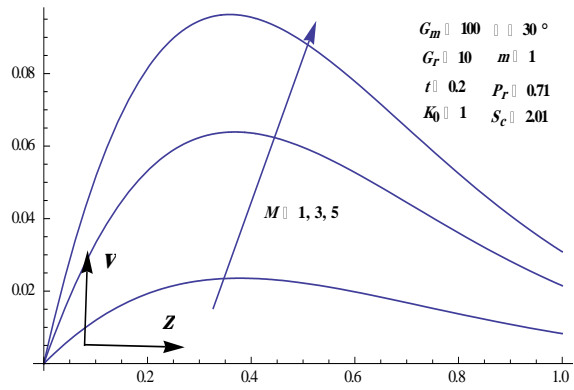


Figure 2.5: velocity v for different values of M

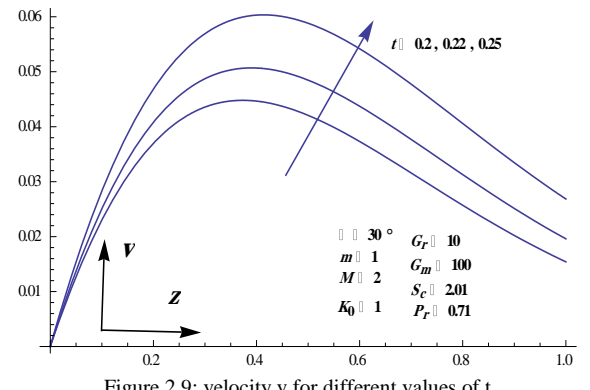


Figure 2.9: velocity v for different values of t

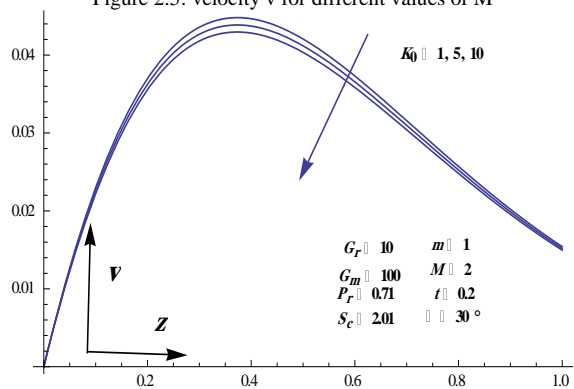


Figure 2.6: velocity v for different values of K0

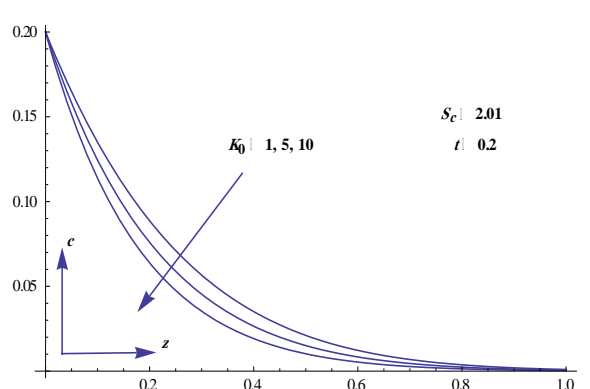


Figure 3.1: c for different values of K0

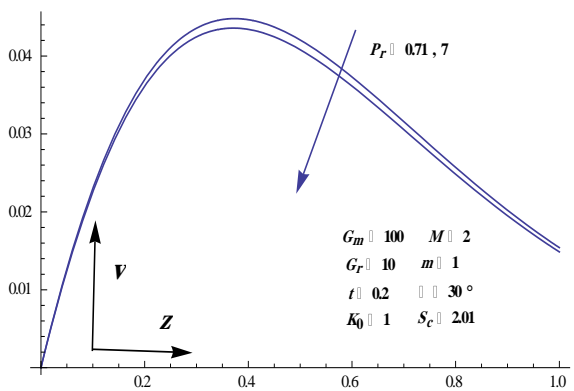


Figure 2.7: velocity v different values of Pr

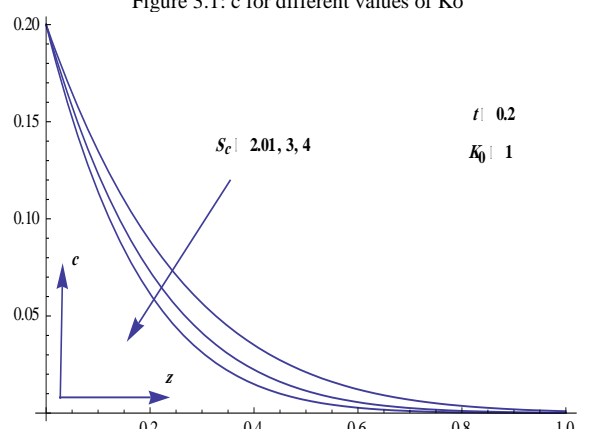


Figure 3.2: c for different values of Sc

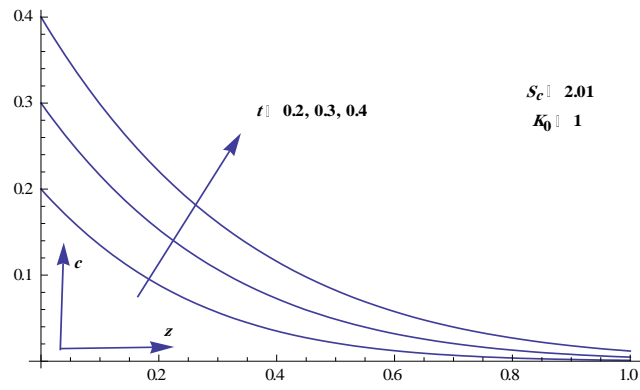


Figure 3.3: c for different values of t

Table1: Skin friction for different Parameters.
(α in degree)

α	M	m	Pr	Sc	Gm	Gr	K_0	t	τ_x	τ_y
15	02	0.5	0.71	2.01	100	10	01	0.2	-18.8529	-6.69686
30	02	0.5	0.71	2.01	100	10	01	0.2	-17.0596	-5.97981
45	02	0.5	0.71	2.01	100	10	01	0.2	-14.2068	-4.83916
60	02	0.5	0.71	2.01	100	10	01	0.2	-10.4889	-3.35263
30	01	0.5	0.71	2.01	100	10	01	0.2	-11.3213	-8.64095
30	03	0.5	0.71	2.01	100	10	01	0.2	-19.0148	7.66727
30	02	2.0	0.71	2.01	100	10	01	0.2	-10.0720	-7.42215
30	02	3.0	0.71	2.01	100	10	01	0.2	-8.74910	-9.98736
30	02	0.5	7.00	2.01	100	10	01	0.2	-17.2109	-5.98460
30	02	0.5	0.71	3.00	100	10	01	0.2	-4.55355	-7.52869
30	02	0.5	0.71	4.00	100	10	01	0.2	-1.06865	-4.92974
30	02	0.5	0.71	2.01	010	10	01	0.2	-2.78945	-0.37961
30	02	0.5	0.71	2.01	050	10	01	0.2	-9.13173	-2.86859
30	02	0.5	0.71	2.01	100	50	01	0.2	-15.8221	-5.95394
30	02	0.5	0.71	2.01	100	100	01	0.2	-14.2752	-5.92160
30	02	0.5	0.71	2.01	100	10	02	0.2	-0.63278	-4.87585
30	02	0.5	0.71	2.01	100	10	0.5	0.3	-23.8595	-8.99461
30	02	0.5	0.71	2.01	100	10	1	0.4	-30.4292	-11.9803

6. Conclusion

The conclusions of the present study are as follows:

- Primary velocity increases with the increase in thermal Grashof number, mass Grashof Number, Hall current parameter and time.
- Primary velocity decreases with the angle of inclination of plate, the magnetic field, chemical reaction parameter, Prandtl number and Schmidt number.
- Secondary velocity increases with the increase in thermal Grashof number, mass Grashof Number, the magnetic field and time.
- Secondary velocity decreases with the angle of inclination of plate, Hall currents, chemical reaction parameter, Prandtl number and Schmidt number.
- τ_x increases with the increase in angle of inclination of plate, Gr, and m; and it decreases with angle of inclination of plate, Gm, M, K_0 , Pr, Sc and t.
- τ_y increases with the increase in angle of inclination of plate, Gr and M, and it decreases with Gm, m, K_0 , Pr, Sc and t.
- Concentration of the fluid near the plate increases with time and it decreases with K_0 , and Sc.

References

- [1] Attia Hazem Ali and Ahmed Mohamed Eissa Sayed, "The Hall effect on unsteady MHD Couette flow with heat transfer of a Bingham fluid with suction and injection", Applied Mathematical Modelling 28, pp.1027-1045, (2004).
- [2] Attia H A, "The effect of variable properties on the unsteady Hartmann flow with heat transfer considering the Hall effect", Appl. Math. Model. 27, (7), pp. 551-563, (2003).
- [3] Das U N, Deka R K and Soundalgekar V M, "Effects of mass transfer on flow past an impulsively started infinite vertical plate with constant heat flux and chemical reaction". Forsch. Ingenieurwes 60, pp.284-287, (1994).
- [4] Ibrahim S Y and Makinde O D, "Chemically reacting MHD boundary layer flow of heat and mass transfer over a moving vertical plate with suction", Scientific Research and Essays, 5(19), pp. 2875-2882, (2010).
- [5] Katagiri M, "The effect of Hall current on the magneto hydrodynamic boundary layer flow past a semi-infinite fast plate". Journal of the Physical Society of Japan, Vol. 27(4), pp. 1051-1059, (1969).
- [6] Muthucumarswamy R, "Effects of chemical reaction on a moving isothermal vertical surface with suction", Acta Mech.155, pp. 65-70,(2002).
- [7] Muthucumarswamy R and Ganesan P, "First order chemical reaction on flow past an Impulsively started vertical plate with uniform Heat and Mass Flux." Acta Mechanica, Vol. 147, No. 1-4, pp. 45-57, (2001).
- [8] Maripala Srinivas and Naikoti Kishan "Hall effects on unsteady MHD free convection flow over a stretching sheet with variable viscosity and viscous dissipation" World Applied Sciences Journal 33 (6), pp. 1032-1041, (2015).
- [9] Misra J C, Adhikary S D, "MHD oscillatory channel flow, heat and mass transfer in a physiological fluid in presence of chemical reaction" Alexandria Engineering Journal,55, pp. 287-297, (2016).
- [10] Pop I. "The effect of Hall currents on hydromagnetic flow near an accelerated plate", J. Math. Phys. Sci. 5, pp. 375-379, (1971).
- [11] Pop I and Watanabe T, "Hall effects on magnetohydrodynamic boundary layer flow over a continuous moving flat plate", Acta Mech., Vol. 108, pp. 35-47, (1995).
- [12] Raptis A and Perdikis C, "Viscous flow over a non-linearly stretching sheet in the presence of a chemical reaction and magnetic field". International Journal of Non- Linear Mechanics 41, pp. 527-529, (2006).
- [13] Raptis A and Perdikis C, "Flow of a viscous fluid through a porous medium bounded by a vertical surface", Int. J. Eng. Sci. 21, pp. 1327-1330, (1983).
- [14] Rajput U S and Kumar Surendra, "MHD flow past an impulsively started vertical plate with variable temperature and mass diffusion", Applied Mathematical Sciences, Vol. 5, no. 3, pp. 149 - 157,(2011)
- [15] Rajput U S and Kumar Surendra, "Effect of chemical reaction on free convection MHD flow through a porous medium bounded by vertical surface", Elixir Appl. Math 41, pp. 5957-5962, (2011).
- [16] Ziyauddin and Kumar Manoj, "MHD heat and mass transfer free convection flow near the lower stagnation point of an isothermal cylinder imbedded in porous domain with the presence of radiation" Jordan Journal of Mechanical and Industrial Engineering(JJMIE), Volume 5, Issue 2, pp. 133 - 138 , (2011).
- [17] Thamizhsudar M and Pandurangan J, "Combined effects of radiation and Hall current on MHD flow past an exponentially accelerated vertical plate in the presence of rotation" International Journal of Innovative Research in Computer and Communication Engineering Vol. 2, Issue 12, December (2014).
- [18] Tripathy R S, Dash G C, Mishra S R and Baag S, "Chemical reaction effect on MHD free convective surface over a moving vertical plate through porous medium" Alexandria Engineering Journal (2015) 54, pp. 673-679, (2015).
- [19] Rajput U S and Kumar Gaurav, " Unsteady MHD Flow Past an Impulsively Started Inclined Plate with Variable Temperature and Mass Diffusion in the presence of Hall current" Applications and Applied Mathematics, Vol. 11, Issue 2, pp. 693 - 703, (2016).

Appendix

$$\begin{aligned}
 A_1 &= 1 + A_{16} + e^{2\sqrt{a}z}(1 - A_{17}), A_2 = -A_1, \\
 A_3 &= A_{16} - A_1, A_4 = -1 + A_{22} + A_{18}(A_{23} - 1), \\
 A_5 &= -1 + A_{24} + A_{19}(A_{25} - 1), \\
 A_6 &= -1 - A_{26} + A_{18}(A_{27} - 1), A_7 = -A_6, \\
 A_8 &= -1 - A_{20} + A_{30}(A_{21} - 1), \\
 A_9 &= A_8 + 2(A_{20} + 1), \\
 A_{10} &= -1 - A_{28} + A_{19}(A_{29} - 1), \\
 A_{11} &= \frac{e^{-\sqrt{a}z}}{z} (2A_1 + 2atA_2 + \sqrt{a}A_3), \\
 A_{12} &= -1 + \operatorname{erf} \left[\frac{z\sqrt{P_r}}{2\sqrt{t}} \right], \\
 A_{13} &= e^{-\frac{at}{-1+S_c} - z\sqrt{\frac{(a-K_0)S_c}{-1+S_c} - \frac{tK_0S_c}{-1+S_c}}}, \\
 A_{14} &= e^{-\frac{at}{-1+P_r} - z\sqrt{\frac{(a)P_r}{-1+P_r}}}, A_{15} = 1 + A_{16} + e^{2\sqrt{a}z} A_{17}, \\
 A_{16} &= \operatorname{erf} \left[\frac{2\sqrt{at} - z}{2\sqrt{t}} \right], A_{17} = \operatorname{erf} \left[\frac{2\sqrt{at} + z}{2\sqrt{t}} \right],
 \end{aligned}$$

$$A_{18} = e^{-2z\sqrt{\frac{aP_r}{-1+P_r}}}, A_{19} = e^{-2z\sqrt{\frac{(a-K_0)S_c}{-1+S_c}}},$$

$$A_{20} = \operatorname{erf}\left[\sqrt{t}K_0 - \frac{z\sqrt{S_c}}{2\sqrt{t}}\right],$$

$$A_{21} = \operatorname{erf}\left[\sqrt{t}K_0 + \frac{z\sqrt{S_c}}{2\sqrt{t}}\right],$$

$$A_{22} = \operatorname{erf}\left[\frac{z - 2t\sqrt{\frac{aP_r}{-1+P_r}}}{2t}\right],$$

$$A_{23} = \operatorname{erf}\left[\frac{z + 2t\sqrt{\frac{aP_r}{-1+P_r}}}{2t}\right],$$

$$A_{24} = \operatorname{erf}\left[\frac{z - 2t\sqrt{\frac{(a-K_0)S_c}{-1+S_c}}}{2t}\right],$$

$$A_{25} = \operatorname{erf}\left[\frac{z + 2t\sqrt{\frac{(a-K_0)S_c}{-1+S_c}}}{2t}\right],$$

$$A_{26} = \operatorname{erf}\left[\frac{2t\sqrt{\frac{a}{-1+P_r}} - z\sqrt{P_r}}{2\sqrt{t}}\right],$$

$$A_{27} = \operatorname{erf}\left[\frac{2t\sqrt{\frac{a}{-1+P_r}} + z\sqrt{P_r}}{2\sqrt{t}}\right],$$

$$A_{28} = \operatorname{erf}\left[\sqrt{t}\sqrt{\frac{(a-K_0)}{-1+S_c}} - \frac{zS_c}{2\sqrt{t}}\right],$$

$$A_{29} = \operatorname{erf}\left[\sqrt{t}\sqrt{\frac{(a-K_0)}{-1+S_c}} + \frac{zS_c}{2\sqrt{t}}\right],$$

$$A_{30} = \operatorname{erf}\left[e^{2z\sqrt{K_0}\sqrt{S_c}}\right],$$

Energy Savings in the Jordanian Residential Sector

Hasan Jarad^a, “Moh’d Sami” Ashhab^{a,b}

^a Department of Mechanical Engineering, The Hashemite University, Zarqa, 13115, Jordan

^b Department of Mechanical and Industrial Engineering, American University of Ras Al Khaimah, UAE

Received DEC, 15, 2016

Accepted APRIL, 15, 2016

Abstract

The aim of the present study is to evaluate the reduction in energy use in terms of consumption and cost in the Jordanian residential sector resulting from applying energy efficiency measures. A baseline model for houses in Jordan has been developed to represent the average dwelling unit in terms of construction and energy consumption using the outcome of governmental surveys. Three energy efficiency measures were introduced individually and simultaneously in five scenarios. The energy savings from each scenario were simulated using Hourly Analysis Program (HAP) software and then quantified by comparison with the energy consumption in the baseline. It was found that using enhanced building envelop material can save 24% in energy consumption and 22% in energy cost. Replacing conventional lighting fixtures with efficient fixtures can save 7% of consumption and 10% of cost while the savings from replacing electric water heaters with solar heaters can be 8% in consumption and 13% in cost. If all measures are applied simultaneously, the realized savings were estimated to be 39% in consumption and 41% in cost. Finally, applying the practically viable measures (efficient lighting and solar heaters) can achieve 15% savings in consumption and 22% in cost.

© 2017 Jordan Journal of Mechanical and Industrial Engineering. All rights reserved

Keywords: Energy; Jordan; Residential Sector; Simulation..

1. Introduction

Jordan is considered one of the poorest countries in the primary energy sources not only in the region but also in the world, unlike its neighboring countries in the Arabic Gulf area. This makes the search for clean, sustainable, and cheap energy sources a serious need. Another objective of engineers and researchers is to find the optimum way of energy utilization in terms of production and efficiency.

One of the measures that indicate the bad energy situation in Jordan is the huge amount of imported energy sources which represents 97% of the country's needs. In 2013, the electrical consumption in the residential sector was 5666 GWh which represents 40% of the total electrical consumption for all sectors (industrial, street lighting, water pumping, commercial buildings) [1]. In 2014, this ratio increased to 43 % and can be increased to 51% if water pumping and street lighting are excluded. Residential sector energy consumption share in addition to electrical energy represents 23 % of all energy consumption with different sectors in Jordan [2].

Since the residential sector consumes more than third of the total electrical consumption of the country and quarter of all energy sources, the potential of energy saving in this sector sounds to be significant and

promising. This fact fueled the enthusiasm of researchers to start seeking for energy saving in the residential buildings by means of buildings simulation and considering building envelope smart designs, and other engineering approaches which would allow for satisfying the utilities needs and maintaining the energy consumption at its least.

Jordanian researchers described the energy situation in Jordan in terms of available sources, renewable energy sources, consumption attitudes, and potential of saving, such as the study which was carried out in [3] where the researchers developed two empirical models based on multivariate linear regression analysis as well as the impact of adopting some of the energy efficiency measures (solar heating, efficient lighting) were analyzed. It was found in [4] that the energy and exergy efficiencies in Jordan are equal to 48.2 and 23.2%, respectively. In addition, the study provided an insight to energy analysts and decision makers in Jordan when considering the process of implementing energy policy measures, such as energy efficiency standards in Jordan.

Some of the research focused on specific type of energy source where it has been shown that on percentage basis, the cost to benefit ratio of wind heating system is 4.3% and 3.9% as obtained by fuzzy sets and by AHP method, respectively, compared to 28.5% and 18.6% for electric heating devices, under identical operating

* Corresponding author e-mail: mohdsami.ashhab@aurak.ac.ae

conditions [5]. The results of [6] showed that 18% of country total energy was consumed by residential sector, while urban residential sector consumes 84% of the total residential energy consumption. Also, 27% of urban houses were using solar water heaters. According to [7], space heating in Jordan accounts for 61% of the total residential energy consumption with Kerosene being the most popular fuel used and followed by Liquefied Petroleum Gas (LPG). At the time of published results, 5% of houses wall constructions have thermal insulation and it was found that space heating load can be reduced by about 50%, when using thermal insulation materials in the building envelope.

While using passive and climatic design (like building orientation, optimum size of windows and shading devices and optimum insulation thickness), studying a typical residential building in Jordan shows that the reduction in annual energy consumption of 27.59% using TRNYSIS software and life cycle cost is reduced by 11.94% [8]. A villa in Tunisia is studied and analyzed including the following feature: orientation, window location and size, glazing type, wall and roof construction, lighting fixtures, appliances and efficiencies of heating and cooling systems [9]. It was found out that implementing energy measures can cost-effectively reduce the annual energy use by 50% compared to the current design practices in Tunisia.

Solar energy systems have attracted a lot of attention in Jordan in recent years due to the promising energy savings both in residential and solar sectors. The decreasing solar systems prices are setting the grounds for increased usage of solar energy in Jordan where the solar intensity is high. An adaptive solar tracking system was designed in [10] where simulation results showed accurate system performance. The feasibility of a PV solar system in Jordan was studied in [11]. An experimental solar system including water heater collectors with the circulating pump operated by a PV module was studied towards achieving optimum efficiency of the system [12]. The results relied on the prediction of the system performance done in [13] using the system neural network model developed in [14]. A single-axis tracking parabolic collector for moderate temperature applications was designed and constructed in Jordan [15]. Adaptive neural networks were successfully applied to solar tracking [16]. Similar neural networks techniques have been previously applied to camless engines [17-18] where they showed excellent capabilities.

The aim of the present study is to evaluate the energy use reduction in terms of consumption and cost in the Jordanian residential sector resulting from applying energy efficiency measures. A baseline model for houses in

Jordan has been developed to represent the average dwelling unit in terms of construction and energy consumption using the outcome of governmental surveys. Three energy efficiency measures were introduced individually and simultaneously in five scenarios. The energy savings from each scenario are simulated using Hourly Analysis Program (HAP) software and then quantified by comparison with the energy consumption in the baseline.

2. Residential Model

A comprehensive survey and study was carried out in 2013 by the Jordanian Ministry of Energy and Mineral Resources (JMEMR) to investigate energy consumption in residential sector in Jordan [1]. The results of the present study are utilized to construct a baseline model that represents the current construction and energy consumption of a typical dwelling unit in Jordan which is used to assess energy savings resulting from applying different energy efficiency measures on the residential sector.

The dwellings in Jordan are basically divided into three categories: villa, house and apartment. According to the study, the percentages of the categories for Jordan of twelve governorates are 40.5% apartments, 54.1% houses and 4.8% villas. Therefore, the model takes the form of the category with highest percentage which is the detached house [1].

In order to evaluate the performance of energy efficiency measures in the house model, the parameters of the dwelling that affect energy consumption are defined. These parameters are:

1. A. House characteristics.
2. B. Building envelope.
3. C. Cooling and heating systems.
4. D. Electric appliances.
5. E. Hot water consumption.
6. F. Weather data.
7. G. Electric bill
8. H. Lighting
9. I. Energy Prices

The house layout which represents the baseline model is shown in Figure 1 and is adopted to reflect the construction and energy consumption parameters of the house model. Table 1 provides area breakdown for the individual spaces. The parameters that are used in the calculations of the model under consideration are summarized in Table 2.

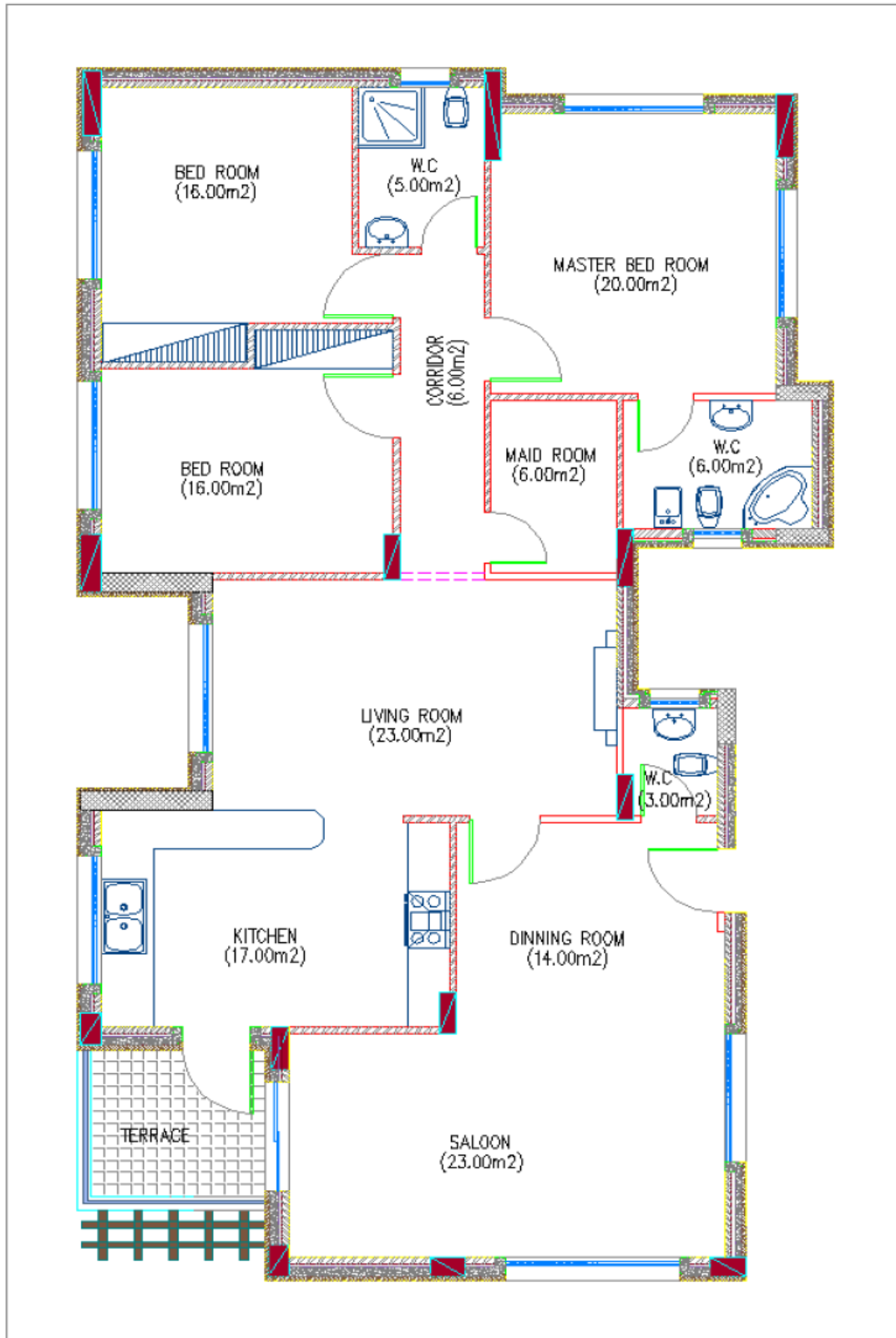


Figure 1. House layout (Baseline model)

Table 1. Area of spaces in the house model

Room	Gross Area (m ²)
Master Bedroom	20
Bedroom 1	16
Bedroom 2	16
Living Room	23
Kitchen	17
Dining Room	14
Living Room	23
Corridor	6
Maid Room	6
Master Bathroom	6
Child Bathroom	5
Guest Bathroom	3
Total	155

Table 2. Summary of all house model parameters and characteristics

House Characteristics	Type	House model
	Area (m ²)	155
	Size of family	6
Building Envelope	Wall	
	U-Value (Overall Heat Transfer Coefficient)	1.74 W/m ² .K
	Roof	
	U-Value	1.372 W/m ² .K
	Ratio %	46
	Floor	
	U-Value	1.055 W/m ² .K
	Ratio %	46
	Glass	
	U-Value	5.52 W/m ² .K
	SHGC (Solar Heat Gain Coefficient)	0.73
	Ratio %	30
	Infiltration	
ACH (Air Change per Hour)	0.25	
Cooling and Heating Systems	Systems	
	DX (Direct Expansion)	2 spaces
	LPG (Liquefied Petroleum Gas)	5 spaces
	Seasons	
	Heating	6 months
	Months	November-April
	Cooling	4 months
	Months	June-September
	Operating Time	
	Cooling	6 hours
	Heating	5 hours
	Set Temperature	
	Summer	23 °C
Winter	19 °C	
Hot Water	Type	Electric
	Coil Load	9.7 kWh
	Operating Time	5.87 h/day
Design Weather Data	Summer Temperature	37 °C
	Winter Temperature	0 °C
	Location	Amman - Jordan
Electric Bill	Summer Consumption	466 kWh
	Winter Consumption	504 kWh
	Annual Cost	433 JD
Lighting	Intensity	W/m ²
	Master Bedroom	4.61
	Bedroom 1	5.53
	Bedroom 2	5.72
	Living Room	3.86
	Kitchen	5.19
	Dining Room	6.69
	Guest Room	7.55
	Corridor	6.86
	Maid Room	8.4
	Master Bathroom	11.11
	Child Bathroom	13.33
	Guest Bathroom	26.09
	Operating Time	6 hours
	Energy Prices	Electric
LPG		8.2 JD/cylinder

3. Methodology and Simulation

This section describes the methodology of evaluating the amount of energy saving that results from applying different energy efficiency measures on the house model given in the previous section which represents the average dwelling unit in Jordan in terms of construction and energy consumption. The house model is the baseline against which different scenarios are compared. In each scenario, pre-defined energy efficiency measures in residential buildings are applied to the house model. Hourly energy simulation is carried out for the baseline and five scenarios which results in certain energy consumption and cost amounts. The consumption and cost of each scenario is then compared with that of the baseline to have a quantified assessment for each scenario.

There are various methods for the estimating energy use in buildings which can be classified according to the purpose of the simulation [19] as follows:

1. Forward modeling: modeling for energy consuming systems design and design optimization.
2. Data-driven modeling: modeling energy use of existing buildings for establishing baselines and calculating retrofit savings.

Energy simulation, in the present study, uses the data-driven modeling to identify and complete the simulation input in order to match the simulation results with the energy use in the house model (baseline) described in section 2. On the other hand, the forward modeling is used to estimate the energy consumption for different scenarios explained in this section. This approach is called the calibrated simulation approach where simulation program is used to tune or calibrate the various inputs to the program so the actual energy consumption matches with the simulation results. The simulation program can be used then to predict savings from individual retrofits.

The Hourly Analysis Program (HAP) is used to carry out the energy simulation of the different scenarios. It is one of the simulation software recognized by the US Green Building Council (USGBC) for proving the achievements of green building energy credits for Leadership in Energy Environmental Design and it is widely used in the cooling and heating load calculations all over the world.

HAP estimates annual energy use and energy costs for HVAC and non-HVAC energy consuming systems in a building by simulating building operation for each of the 8,760 hours in a year. Results of the energy analysis are used to compare the energy use and energy costs of alternate HVAC system designs so that best design can be chosen. Specifically, HAP performs the following tasks during an energy analysis:

1. Simulates hour-by-hour operation of all heating and air conditioning systems in the building.
2. Simulates hour-by-hour operation of non-HVAC systems including lighting and appliances.
3. Uses results of the hour-by-hour simulations to calculate total annual energy use and energy costs. Costs are calculated using actual utility rate features, such as stepped, time-of-day and demand charges, if specified.
4. Generates tabular and graphical reports of hourly, daily, monthly and annual data.

Five energy efficiency scenarios recruiting three energy efficiency measures are simulated and compared with the baseline. The scenarios and the associated energy efficiency measures are summarized as follows:

1. Scenario 1: Enhanced building envelope characteristics.
2. Scenario 2: Efficient Lighting fixtures.
3. Scenario 3: Solar water heaters.
4. Scenario 4: Total measures.
5. Scenario 5: Solar water heaters and efficient lighting fixtures.

4. Results and Discussion

The results of the energy simulation for the house model (baseline scenario) and the enhanced scenarios are illustrated and discussed. Then a comparison in terms of annual energy consumption and annual cost for each scenario is conducted. For each scenario, the following results are illustrated:

1. The house components share in the annual energy consumption (kWh).
2. House model annual energy cost (JD).

After discussing each scenario results, comparisons between the different scenarios are conducted in terms of their annual energy consumption and the annual energy cost.

The house model components share in the annual energy consumption (kWh) and the annual energy costs for the baseline scenario are shown in Figures 2 and 3, respectively. The annual energy consumption for the house model (baseline) equals 7783 kWh, and the heating system represents maximum system energy consumption which is equal to 2245 kWh. Cooling equipment, lighting fixtures, and fans in the air conditioning equipment, are not considered major energy consumption systems since they consume 795, 690, and 184 kWh, respectively. The miscellaneous electrical equipment consumes approximately the same amount of energy which is consumed by the heating system and equals 2234 kWh. Amongst all systems, it is anticipated that the heating system will have the maximum potential for energy saving when considering the enhanced scenarios.

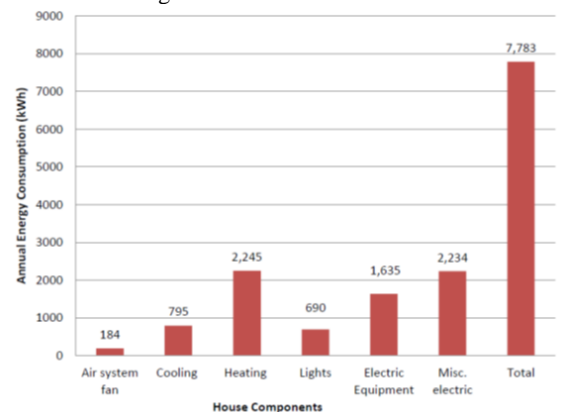


Figure 2. House model components share in annual energy consumption (kWh) for the baseline scenario.

As shown in Figure 3, the annual energy cost for the house model (baseline) equals 542 JD. The heating system represents the maximum energy consumption system which costs 120 JD. Since the cooling equipment, lighting fixtures, and fans in the air conditioning equipment are not

considered major energy consumption systems, they cost 65, 52, and 14 JD, respectively. It is observed that, the heating system and the miscellaneous appliances have similar energy consumption in kWh, yet different energy cost which is justified by the fact that the heating system is operated by two sources of energy which are the electricity and the LPG. Hence, the use of LPG in operating the heating system lead to a reduced energy cost, which means that converting the heating energy source from electricity to LPG is considered one of the areas of enhancement. This should be considered by energy analysts and decision makers.

In the enhanced building envelope characteristics scenario 1, annual house energy consumption and cost are shown in Figures 4 and 5, respectively. The annual energy consumption equals 5,931 kWh, and the heating system consumes 623 kWh which was an anticipated result when the building envelope was enhanced in terms of its design parameters. It is obvious that none of the electrical appliances, electrical equipment, lighting fixtures, and fans, is affected by enhancing the building envelope, hence no energy savings were observed in any of these systems.

As shown in Figure 5, the annual energy cost for the model scenario 1 equals 423 JD and the heating system was the most governing factor in the cost reduction between scenario 1 and the house model. Since the cooling system is considered dependent on the building envelope, its annual cost was decreased from 65 JD to 44 JD when the building envelope was enhanced. The cost of the rest of energy consumption systems which were not affected by enhancing the building envelope was not reduced.

In the efficient lighting fixtures scenario 2, annual house energy consumption and cost are plotted in Figures 6 and 7, respectively. As shown in Figure 6, it is obvious that the annual energy consumption was decreased due to the enhancement in the lighting efficiency by 500 kWh, in addition to the decrease in the lighting energy consumption. Heating system energy consumption was not reduced as a result of enhancing the lighting efficiency because the simulation software does not incorporate the heat emitted by solar sun and by any electrical lighting or appliances in the heating load calculation.

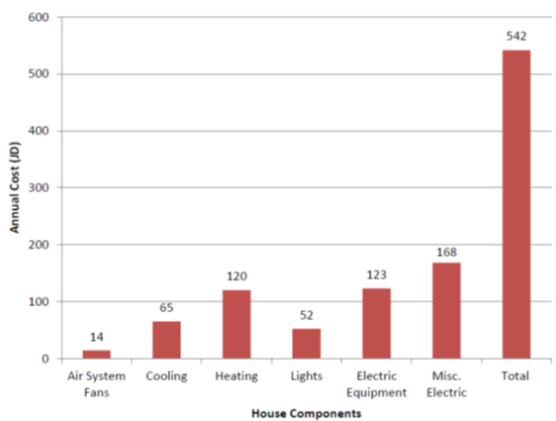


Figure 3. House model (baseline) annual energy cost

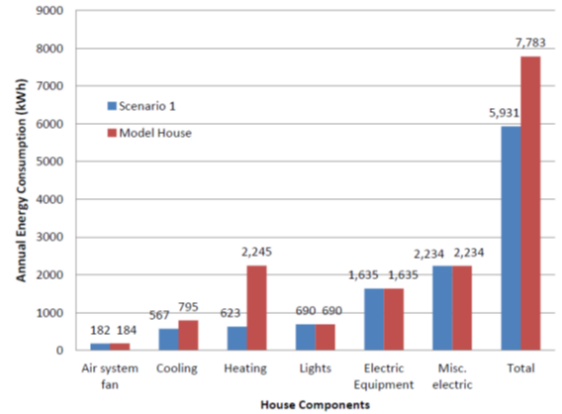


Figure 4. House model components share in annual energy consumption (kWh) for scenario 1

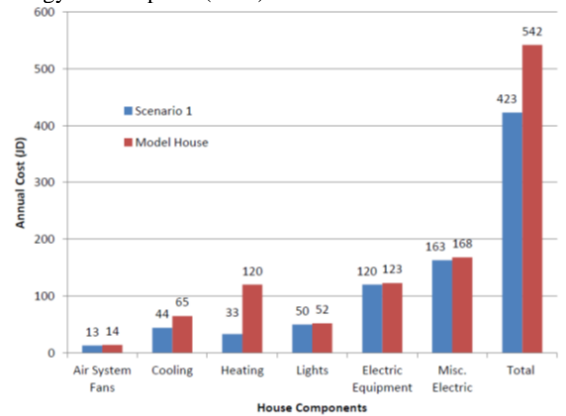


Figure 5. House model's annual energy cost for scenario 1

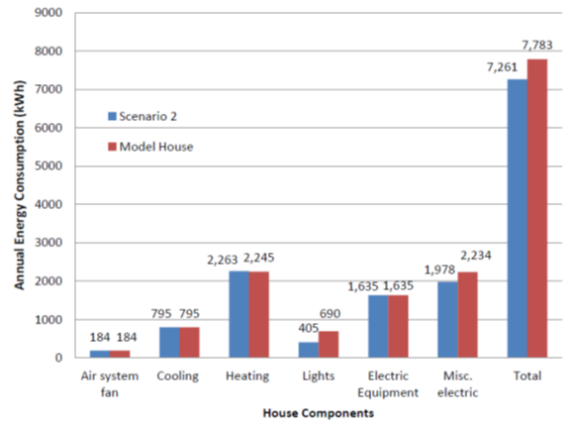


Figure 6. House model components share in annual energy consumption (kWh) for scenario 2

In Figure 7, the annual energy cost for scenario 2 and how it is distributed between the house energy consumption systems are shown. The annual energy cost for scenario 2 equals 486 JD, and since the heating system was not affected by enhancing the lighting efficiency, its annual cost remains 120 JD. The same result is observed for the rest of systems which were not affected in terms of their annual energy cost except the lighting which was reduced from 52 JD to 29 JD and this is considered a major energy cost saving.

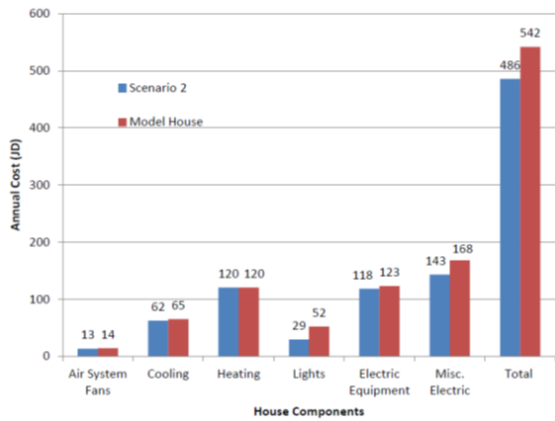


Figure 7. House model's annual energy cost for scenario 2

In the solar water heater scenario 3, annual house energy consumption and cost are represented in Figures 8 and 9, respectively. The annual energy consumption for scenario 3 equals 7151 kWh, and the effect of installing a solar water heater is obvious when observing the reduction in the annual energy consumption in the miscellaneous electrical items, which include the electrical water heater. Adding the solar water heater reduces the need for operating the electrical water heater. Therefore none of the energy consumption systems such as air conditioning systems and lighting fixtures was affected by this enhancement.

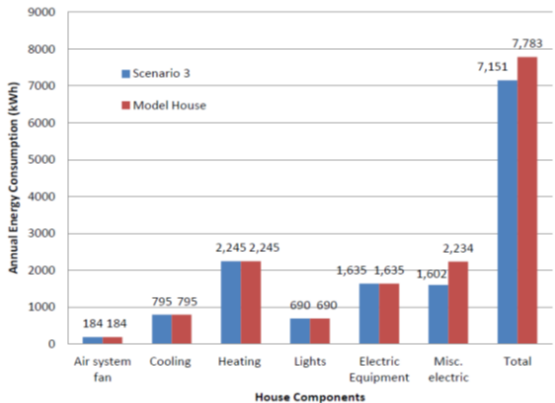


Figure 8. House model components share in annual energy consumption (kWh) for scenario 3

In Figure 9, the annual energy cost for scenario 3 and how it is distributed between the house energy consumption systems are shown. The annual energy cost for scenario 3 equals 472 JD, and since the energy saving was due to the adoption of a solar water heater, the saving in the annual energy cost was observed in the miscellaneous electrical appliances which include the solar water heater as the governing factor in the total cost saving. Minimal saving in the cost of operating the cooling system was observed to be 7 JD annually.

The annual house energy consumption and cost for the total measures scenario 4 are shown in Figures 10 and 11, respectively. Adopting scenario 4 (which implies combining all different scenarios in enhancing the house model) was anticipated to result in significant annual energy consumption reduction, and the results shown in Figure 10 are consistent with this anticipation. The total annual energy consumption was decreased from 7783 to 4778 kWh, as well as each individual system was decreased in terms of its energy consumption expect the

air fans and the electrical equipment systems which were not enhanced in any of the scenarios.

As shown in Figure 11, the annual energy cost for scenario 4 equals 321 JD, and the cost saving represents 40%. This major saving was from combining all scenarios simultaneously. As mentioned earlier, air fans and electrical equipment were not taken into consideration while proposing systems enhancement. Therefore, none of them have participated in the total cost savings.

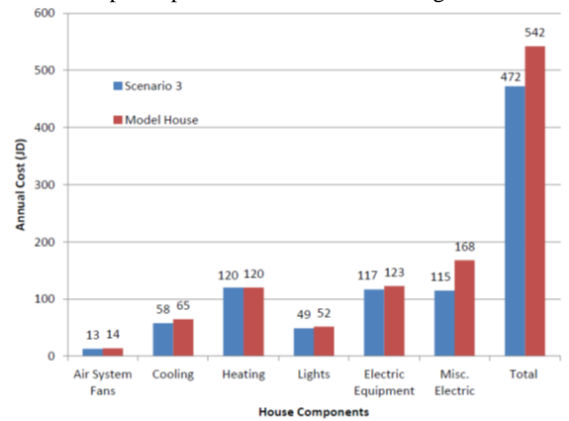


Figure 9. House model's annual energy cost for scenario 3

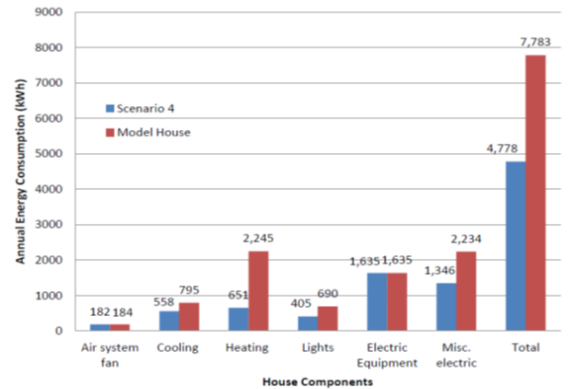


Figure 10. House model components share in annual energy consumption (kWh) for Scenario 4

In scenario 5, namely the solar water heaters and efficient lighting fixtures scenario, the corresponding annual house energy consumption and cost are shown in Figures 12 and 13, respectively. As shown in Figure 12, the annual energy consumption for scenario 5 equals 6629 kWh. As described in section 3, this scenario was proposed for the existing buildings since it is applicable in both new constructed and existing buildings. Combining the lighting efficiency enhancement measure in addition to adopting solar water heaters resulted in a significant energy saving which represents 15% of the annual energy consumption. The non-enhanced systems such as the electrical equipment and the heating system (which are not affected by the lighting and the solar water heater) were not affected here as well.

As shown in Figure 13, the annual energy cost was decreased from 542 JD to 425 JD which represents 22% reduction. Lighting energy cost decreased from 52 JD to 28 JD, and the electrical appliances energy cost decreased from 168 JD to 98 JD which represent 46% and 41%, respectively. Other systems did not participate in the annual energy cost since none of them was enhanced in this scenario.

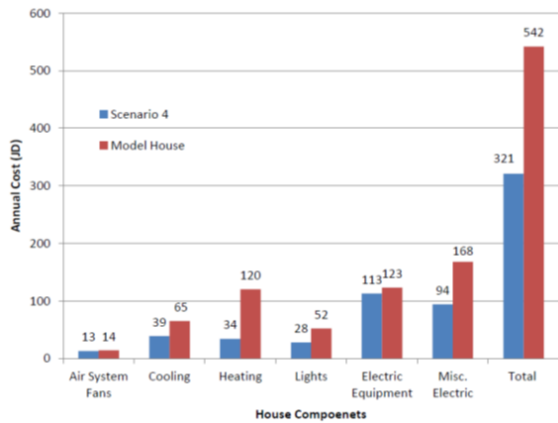


Figure 11. House model's annual energy cost for scenario 4

The illustrated results above are summarized to enable a comparison between different scenarios as well as to assess each scenario share as an energy saving approach. Annual house energy consumption for all scenarios is shown in Figure 14. The highest energy consumption is for the baseline model and equals 7,783 kWh. The scenario with lowest energy consumption is scenario 4 and its consumption is equal to 4,778 kWh. Scenario 2 has the highest consumption of 7,261 kWh. For reduction ratios from baseline model, best scenario is 4 with 38.6% reduction followed by scenario 1 with 23.8% reduction, whereas scenario 5 scored 14.8% reduction and the remaining two scenarios, namely scenarios 2 and 3 with reductions of 6.7% and 8.1%, respectively.

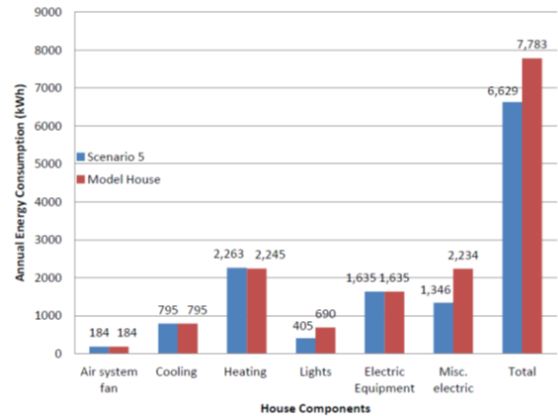


Figure 12. House model components share in annual energy consumption (kWh) for scenario 5.

The results for annual cost comparison of all scenarios are shown in Figure 15. The scenario with highest annual cost is scenario 2 with 486 JD annual cost and corresponding reduction of 10.3%. Scenario 3 annual cost and reduction are 472 JD and 13%, respectively. The scenario with the least annual cost is scenario 4 with 321 JD annual cost and an associated reduction percentage of around 41%. Scenario 5 has annual cost of 425 JD and savings on annual cost from baseline model of 21.6%. Similarly, scenario 1 annual cost and reduction are 423 JD and 22%, respectively. Thus, using solar water heaters and efficient lighting give similar results as using enhanced building envelope.

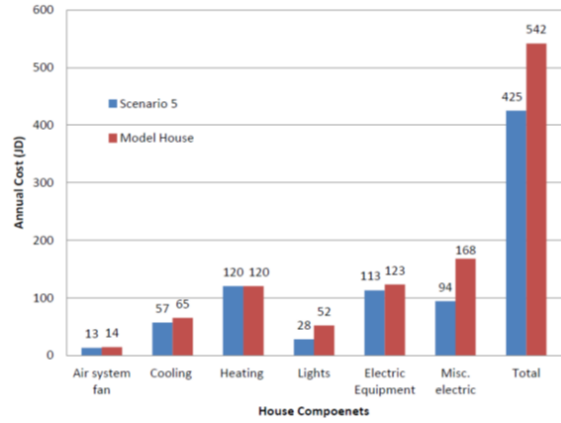


Figure 13. House model's annual energy cost for scenario 5

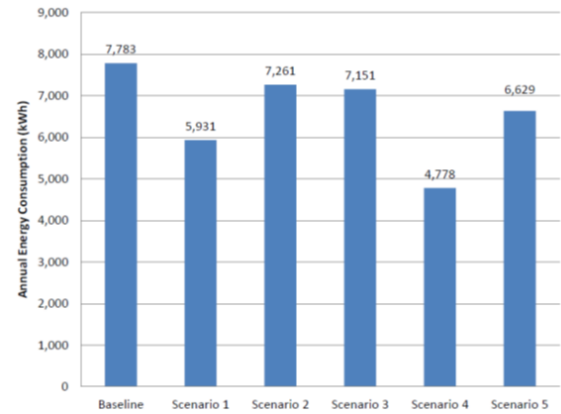


Figure 14. Annual house energy consumption comparison

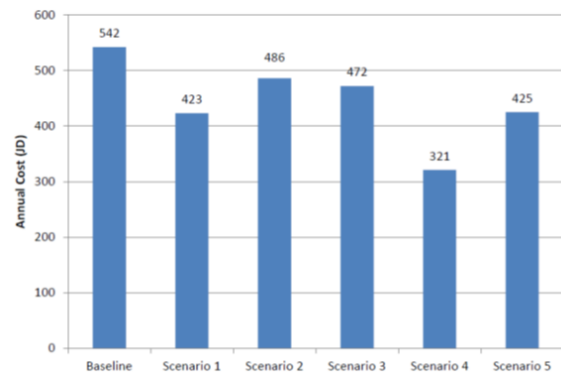


Figure 15. Annual cost comparison for all scenarios

5. Conclusions

A baseline model was defined using statistics, calculations and assumptions to represent the current energy use of the residential sector in Jordan. Three energy saving measures were introduced in five scenarios to assess their individual and collective impact on energy consumption. Hourly energy simulation was performed for the baseline and the five scenarios using HAP software. The savings were introduced and discussed for each scenario and a thorough comparison with the baseline was conducted. The best scenario for new houses before construction is the total measures scenario with 39% reduction in energy consumption and 41% reduction in annual energy cost. On the other hand the best scenario for existing houses is the solar water heaters and efficient lighting fixtures scenario with reduction percentages of

15% and 22 % for energy consumption and annual energy cost, respectively.

References

- [1] Survey for energy use in residential sector, Ministry of Energy and Mineral Resources, 2013, Amman, Jordan.
- [2] Energy2014- Facts & Figures, Ministry of Energy and Mineral Resources, 2014, Amman, Jordan.
- [3] Al-Ghandoor A., Jaber J.O., Al-Hinti I. and Mansour I.M., "Residential past and future energy consumption: Potential savings and environmental impact", *Renewable and Sustainable Energy Reviews*, Vol. 13, 2009, 1262–1274.
- [4] Al-Ghandoor A., "Evaluation of energy use in Jordan using energy and exergy analyses", *Energy and Buildings*, Vol. 59, 2013, 1–10.
- [5] Jaber J.O., Jaber Q.M., Sawalha S.A. and Mohsen M.S., "Evaluation of conventional and renewable energy sources for space heating in the household sector", *Renewable and Sustainable Energy Reviews*, Vol. 12, 2008, 278–289.
- [6] Akash B. and Mohsen M., "Energy analysis of Jordan's urban residential sector", *Energy*, Vol. 24, 1999, 823–831.
- [7] Jaber J., "Prospects of energy savings in residential space heating", *Energy and Buildings*, Vol. 34, 2002, 311–319.
- [8] Jaber S. and Ajib S., "Optimum, technical and energy efficiency design of residential building in Mediterranean region", *Energy and Buildings*, Vol. 43, 2011, 1829–1834.
- [9] Ihm P. and Krarti M., "Design optimization of energy efficient residential buildings in Tunisia", *Building and Environment*, Vol. 58, 2012, 81–90.
- [10] B. K. Hammad, R. H. Fouad, M. S. Ashhab, S. D. Nijmeh, M. Mohsen, A. Tamimi, Adaptive Control of Solar Tracking System, *IET Science, Measurement and Technology*, doi: 10.1049/iet-smt.2013.0293, 2014.
- [11] M. S. Ashhab, H. Kaylani and A. Abdallah, PV Solar System Feasibility Study, *Energy Conversion and Management*, Vol 65, 2013, pp. 777 - 782.
- [12] R.H. Fouad, M.S. Ashhab, A. Mukattash and S. Idwan, Simulation and Energy Management of an Experimental Solar System through Adaptive Neural Networks, *IET Science, Measurement and Technology*, Vol. 6, No. 6, 2012, pp. 427-431.
- [13] M.S. Ashhab, Adaptive Prediction of the Performance of a Photovoltaic Solar Integrated System, *International Journal of Thermal & Environmental Engineering*, Vol. 3, 2011, pp. 43–46.
- [14] M .S. Ashhab, Optimization and Modeling of A Photovoltaic Solar Integrated System by Neural Networks, *Energy Conversion and Management*, Vol 49, 2008, pp. 3349 - 3355.
- [15] S. Odeh, S. Nijmeh, M. S. Ashhab, Y. Zakaria and A. Amra, Design of a Single-Axis Tracking Parabolic Collector for Moderate Temperature Applications, *ISES Conference, EuroSun 2004*, Vol. 1, pp. 527-532, Freiburg- Germany.
- [16] M. S. Ashhab, Solar Tracking by Neural Network Adaptive Techniques, *The Second Annual Int. Conference on Advanced Topics in Artificial Intelligence*, November 2011, Singapore.
- [17] M. S. Ashhab, Intelligent Neural Network Control of an 8-Cylinder Camless Engine, *The Second International Conference on Kansei Engineering & Affective Systems*, November 2008, Nagaoka-Japan.
- [18] M. S. Ashhab, Modeling and Adaptive Control of A Camless Engine Using Neural Networks and Estimation Techniques, *The IASTED International Conference on Applied Simulation and Modeling*, August 2007, pp. 262-266, Palma de Mallorca-Spain.
- [19] Energy estimating and modeling methods, *ASHRAE Handbook*, American Society of Heating, Refrigerating, and Air-Conditioning Engineers, 2013, Atlanta-USA.

Performance and Effective Method of Experimenting Micromixer Using Finished smooth glasses and Cohesive Tape

C. T. Lee *^a, C. C. Lee^b, M. L. Liu^c

^a Bryant Zhuhai College, Beijing Institute of Technology Zhuhai, Guangdong, China

^b Dept. of Chemistry, Simon Fraser University, Vancouver, BC., Canada

^c Institute of Artificial Intelligence, Corporate Research Center, Midea Group Co., Ltd., Guangdong, China

Received ...

Accepted ...

Abstract

Micromixer has been drawing upon various branches of engineering science and allied areas within biology and biomedicine. In the present study, an easy and fast fabrication method on hydrophilic micromixer using Optically Clear Adhesive (OCA) double-sided tape together with glass is proposed. Different experiments on types of planar hydrophilic micromixers with baffle structures are designed for hydrophilic microchannel. Flow is driven by capillary action using surface tension and flow tests are carried out to show that the double-sided OCA tape-glass micromixer can achieve the mixing result of 71% in gray level image analysis.

© 2017 Jordan Journal of Mechanical and Industrial Engineering. All rights reserved

Keywords: Capillary, chip, hydrophilic, microfluidic, micromixer, mixing, OCA.

1. Introduction

Microfluidic systems have shown a wide application to biomedical science and are well-received in medical examination. In some special cases, micromixers have demonstrated promising practices to the area of biotechnology field such as application of RNA/DNA and PCR amplification [1, 2]. In general, micromixers can be featured in two categories, namely the active micromixers and passive micromixers. An active mixer required external powers to effect the mixing of fluids [3, 4], while a passive mixer can only handle the fluid by splitting and recombining the stream in the device [5, 6, 7, 8].

There are many ways to produce the microchannels in the experiment and it is by virtue of the use of MEMS devices. For example, the mechanism of pumping the fluids in MEMS devices is developed and shown in [9] where the authors undertake the work to provide the best solution in the application of micropumping. Other progress has made the use the chemical and biological knowledge [10] which is focused on the development of the pumping technique and controlling of fluid delivery. The establishments of the pumping technique are very important in applications such as thermal, light, magnetic and electrical mechanisms, and micropumps such as electroosmotic, electrophoretic, opto-electrowetting, electrochemical, optically-driven, and gravity-driven pumps all use the mechanism of electro- or kinetically-driven continuous flow to drive fluids in the MEMS where three different kinds of miscible solutions (phosphate-

buffered solution, gold nanocolloids and 20% glycerol), with Rhodamine 6G aqueous solution, were used as sample fluids [11]. In addition, there is a fabrication method for single glass microchannels which uses conventional photolithographic and chemical etching process [12], and the fabrication of glass chips by using electrophoresis mechanism with capillary phenomenon is shown in [13]. It is well known that the device is produced by glass substrates using thermal bonding method. Moreover, for the PDMS microchannels using SU-8/PMMA moldings and polystyrene substrate, the microfabrication method was reported in [14]. In addition, the method of using O₂ plasma to change the PDMS characteristics and creating different profiles of microchannels was shown in [15]. In recent years, the use of negative photoresist JSR and PMMA polymer as a substrate is employed for the formation of microchannel structures [16] and an interesting approach that integrates the method of photoresist and soft lithography with circular microchannels was proposed in [17].

The present study introduces an fast yet easy experiment in fabricating hydrophilic micromixers. We do the fabrication by using the double-sided optically clear cohesive tape together with glass substrates and laser machining technique. The double-sided cohesive tape is of OCA8187 from 3M Company, which has high strength of adhesion to different glass surfaces with weatherable and water-resistant ability. We would like to combine the finished hydrophilic glass substrates and engrave microchannels to drive the fluid streams using surface tension. The finished micromixer is designed as Y-shaped

* Corresponding author e-mail: scat1440@yahoo.com.

with baffled structures extended for 18 mm long, and the width of channel is 600 μm with the width of the baffle to the channel wall as 150 μm . Water-assisted CO₂ laser machining is applied to cool down the glasses during the manufacturing process and cohesive tape-glass microchannel pattern was carved out with bounded glasses.

It is shown in literature that microchannel with PDMS requires a length of 15-20 mm to achieve an uniform mixing [18, 19], but it is found the channel suffers low transport velocity for liquids and poor hydrophobic recovery for substrates [20, 21]. To fix the situation, a Liquid Crystal Polymer (LCP) with glass chip was introduced to improve the hydrophobic recovery property but still shows difficulty in fabrication when using CO₂ laser machining [22]. As far as we understand, most microchannels can be done with glass or PDMS materials for mixing purpose, but it still shows the fact that the PDMS with glass is unstable and can suffers poor thermal bonding. Out main idea of using tape-glass microchannel materials stays with the advantage properties of the hydrophilic, and thermal bonding of the material. The cohesive tape-glass features good hydrophilic characteristic and require less complexity of fabrication process. The present paper aims to introduce a novel process of fabrication tape-glass mixromixer with hydrophilicity.

We aimed to place a number of baffles periodically in the microchannels in an alternating fashion. The chip for baffle structures and that without baffles are shown in Fig. 4 and Fig. 5. The baffle structures in microchannel can be seen in Fig. 7 and Fig. 8. Notice that the baffle gap is fixed at 90 μm while baffle space was fixed at 150 μm . Fig. 8 shows the details of the chip with baffle space and gap. The baffles in microchannel will allow interfacial contacts for liquids at low Reynolds number and we conducted a series of flow tests to study the mixing performance. The Reynolds number in the capillary channel is less than around 0.2 and the tape-glasses structure has the property of hydrophilic stability. It is not only an easy manufacturing process but also avoids annoying etching and depositing process.

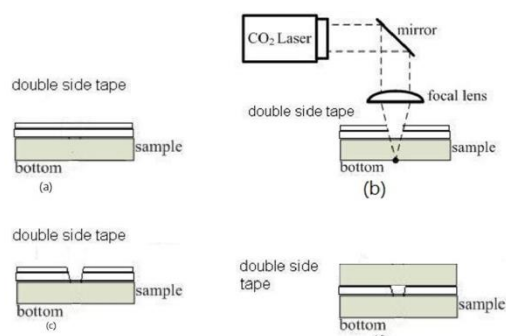


Figure1. Fabrication procedure for Optically Clear Adhesive (OCA) double-sided tape-glass microchannel

2. Experimental Procedures

Our experiment adopted tape of 3M, OCA8187, with high strength of adhesion and water resistance. It is also humidity- and UV light-resistant when applied on optical device material.

We use laser machine to fabricate the microchannel with cohesive tape and glasses. The glass is a microscope slide (FEA) with size of 1"× 3" and thickness of 1-1.2 mm. By cleansing with isopropyl alcohol, we are able to wash substrate with Deionized (DI) water and dried it with compressed-air gun. Then we can attach the double-sided OCA cohesive tape onto the microscope slide and tear off the protective layer during the process (Fig. 1(a)). The double-sided OCA tape has high cohesion and durability and easy application to different surfaces. Moreover, the laser power of 5 Watts and scan speed of 11.4 cm/s were used to drill holes with carved channel pattern (Fig. 1(b)). The water-assisted CO₂ laser is used to cool down the glass during the carving process. Finally, we bond the cohesive tape-glass pattern with another substrate by matching the inlet and outlet (Fig. 1(c), Fig. 1(d)).

As from Fig. 1(d), the glass slides were bonded on top and bottom sides of surfaces with cohesive tape for carving microchannels. Therefore the bonding and contacting surfaces of microchannel are on the glass with OCA cohesive tape attached on the left and right contacting phase. Notice that the double-sided cohesive tape has high durability and water resistance, which make tape-glass microchannel hydrophilic to be able to drive fluids on the substrate. Fig. 2(a) shows the contact angle of DI water on PDMS for comparison, and Fig. 2(b) shows the contact angle of DI water on OCA-glass slide. The flow chart of fabrication procedure is shown in Fig. 3.

As the baffled structure in microchannel is considered, we use the software CorelDRAW(R) 12 to draw the channel pattern and laser machining to carve the channel in micro-scale size. In our experiments, the baffled structure and microchannel was set with length of 1800 μm and width of 600 μm . Moreover, the space between the baffled channel wall was 150 μm and the depth was set as 175 μm . Fig. 4 shows the graph of micromixer without baffle structure, while Fig. 5 demonstrates the graph of micromixer with baffle structure. The finished work of double-sided cohesive tape-glass micromixer is shown in Fig. 6.

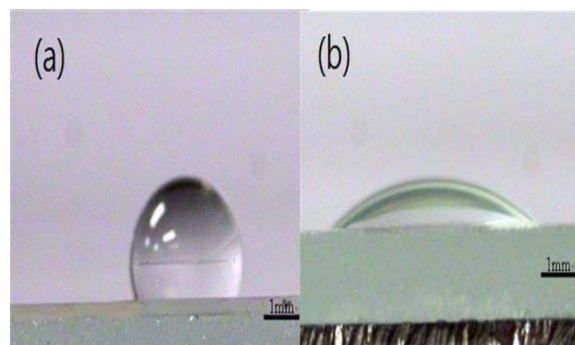


Figure2. Contact angle of DI water (5 μl) on material surface; (a) PDMS substrate; (b) OCA-glass slide..

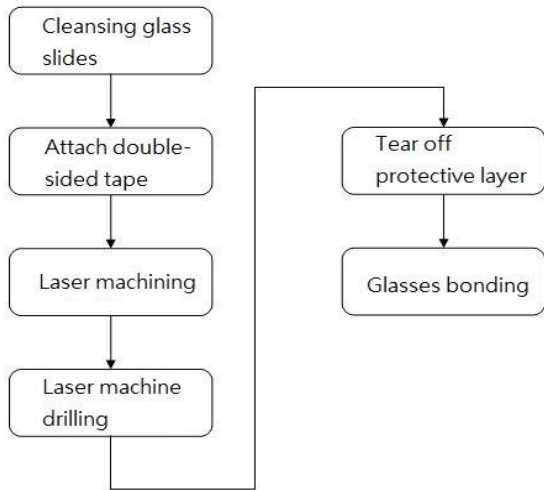


Figure 3. Flow chart of fabrication procedure for double-sided tape and glass microchannel.

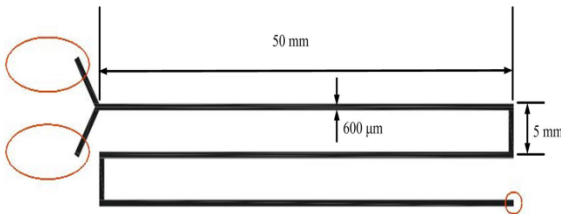


Figure 4. Schematic diagram of CorelDRAW graph for OCA tape-glass micromixer without baffle structure..

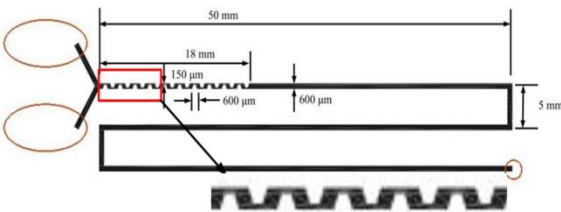


Figure 5. Schematic diagram of CorelDRAW graph for OCA tape-glass micromixer with baffle structure.

3. Governing Equations and Theory

The physics for capillary-driven flow in the microchannel relies on the driving force Δp , and the Laplace-Young equation as follows [23]:

$$\Delta p = \frac{2\sigma(h+w)\cos\theta}{wh}, \quad (1)$$

where Δp is the pressure drop across the interface, σ the surface tension of the fluid, θ is the contact angle, w the width of the microchannel, and h is the height of the microchannel. Notice that if the contact angle is less than 90° , then the driving force across the interface will be positive and the fluid will be driven along the channel. As the width of channel is much larger than its height, the driving force will be expressed as the following form:

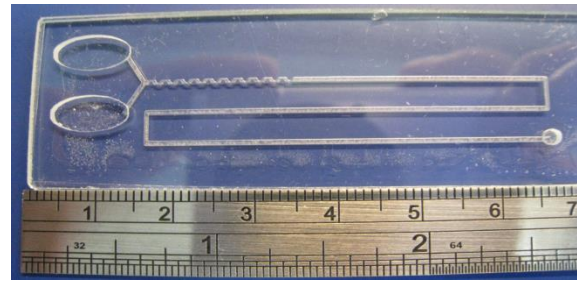


Figure 6. The finished work of double-sided OCA tape-glass baffled micromixer..

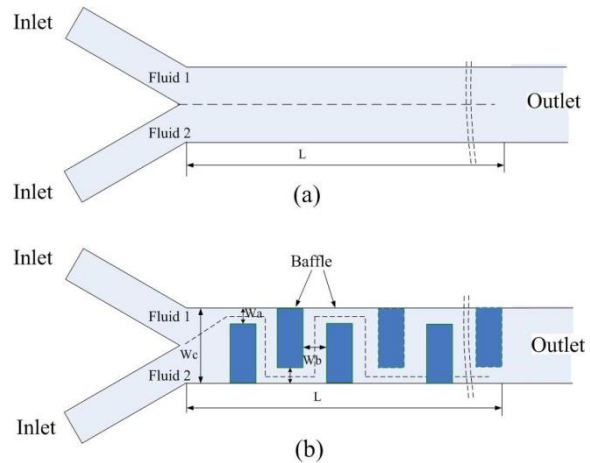


Figure 7. Detailed schematic diagram of microchannel with baffles..

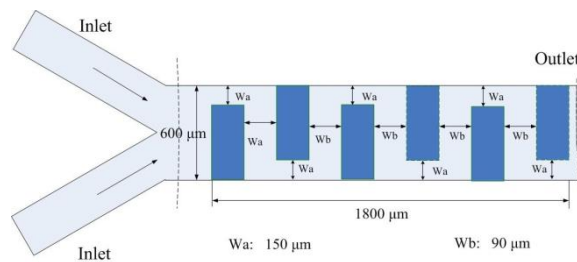


Figure 8. Flow direction and design of baffles for microchannel.

$$\Delta p = \frac{2\sigma \cos\theta}{h}. \quad (2)$$

Our work focuses on the rectangular microchannel with its geometric dimension $w \gg d$, which it will make the surface and the capability of capillary action to be activated to drive the fluids in the microchannel. We also note that in such a small dimension, the capillary action will drag the liquid where the adhesion of liquid molecules will attach onto the surface of glass substrates.

In our idea, the use of the OCA cohesive tape on glasses provides the wetting stability in microchannels. In theoretical analysis, since the OCA tape- microchannels is small in dimension to allow the pressure drop across the air/liquid meniscus and will be assumed to have the following expression [24]:

$$\Delta p = \frac{2\sigma w \cos \theta_1 + 2\sigma h \cos \theta_2}{wh}, \quad (3)$$

where θ_1 is the contact angle of both the upper and bottom walls, θ_2 is the contact angle for left and right walls and h the height of the microchannel. Moreover, by taking the depth of the channel into account, the factor to control the fluid behaviour in the microchannel can be expressed as follows [25]:

$$Q = \frac{1}{\eta} \frac{\Delta p}{R_F}, \quad (4)$$

where η is the viscosity of the liquid, Δp the difference in pressure inside and in front of the liquid, Q the flow rate and R_F is the flow resistance of geometry with the following [25]

$$R_F = \frac{1}{12 \left(1 + \frac{5h}{6w}\right) \frac{hwR_H^2}{L}}. \quad (5)$$

Here w is the width of channel, h is the depth of channel, L is the length of channel, $R_H = hw/(h+w)$ is the hydraulic radius for rectangular channel. By Eq. (5), we also notice that the longer the channel length, the bigger the flow resistance. Detailed mechanism of the physics and dynamics of capillary flow, including the governing equations of the capillary flow are represented as follows:

$$\nabla \cdot \mathbf{V} = 0, \quad (6)$$

$$\rho \mathbf{V} \cdot (\nabla \cdot \mathbf{V}) = -\nabla P + \mu \nabla^2 \mathbf{V}, \quad (7)$$

$$\frac{\partial F}{\partial t} + \nabla \cdot \mathbf{V} F = 0, \quad (8)$$

where V is the velocity, ρ the density of fluid, P the pressure, μ the viscosity and F is the liquid volume fraction. The above equations will give the physics and movement of meniscus of capillary flow in a microchannel and numerical calculation will require the nonlinear coupling equations (6)-(8).

4. Results and Discussions

The present study addresses a special method of fabrication for hydrophilic microchannel using the double-sided cohesive tape with glasses. We carried out the procedure for microchannels with baffle structures. The fabrication procedure is performed through the laser machining and image capture device and the flow behaviour is captured by digital CCD optical microscope (MORITEX MLZ-07545). The mixing results of the cohesive tape-glass mixer without baffles are shown in Fig. 9, while the mixing behaviour for micromixer with baffle structure is illustrated in Fig. 10. It is seen that the mixing performance can be significantly improved if one adds the baffle structure in the channel.

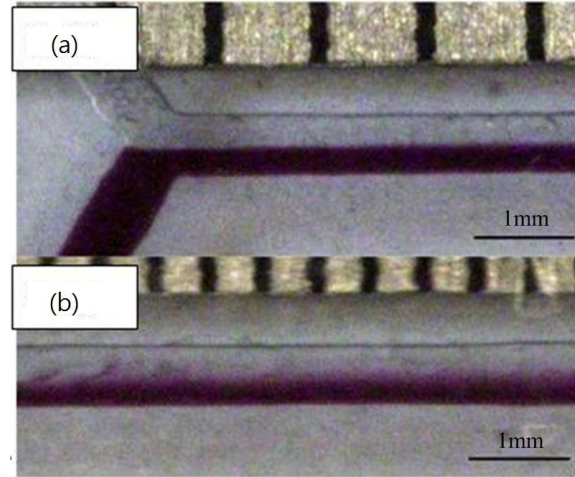


Figure 9. Mixing tests for OCA double-sided tape-glass straight microchannel; (a) upstream area; (b) downstream area.

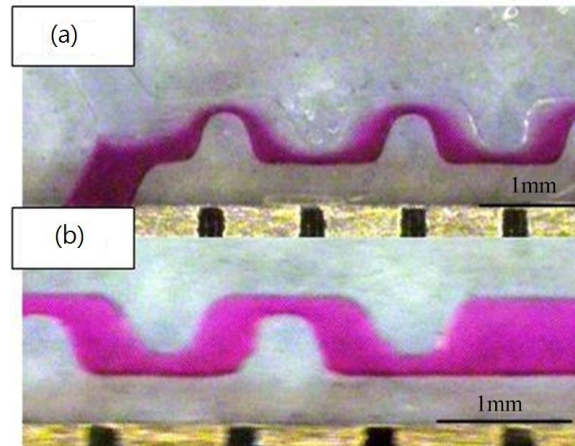


Figure 10. Mixing tests for OCA double-sided tape-glass baffled microchannel; (a) upstream area; (b) downstream area.

In order to quantify the degree of mixing, the mixing efficiency is calculated by the following formula:

$$M = 1 - \sqrt{\frac{1}{n} \sum_{i=1}^n \left(\frac{n_i - \bar{n}}{n} \right)^2}, \quad (9)$$

where M is the mixing efficiency, n is the total number of sampling points, n_i the mole fraction over the whole cross section at the outlet of the micromixer and \bar{n} the average mole fraction. Mixing efficiency is calculated from 0.00 (0% mixing) to 1.00 (100% mixing).

We calculate the mixing results at the inlet-structure (entrance) and outlet-structure (exit) of the baffled channel of Y-shaped chip. Our idea was focused on the mixing behaviour at in- and out- of the baffled structure as well as its mixing results.

The mixing efficiency for OCA double-sided tape-glass micromixer without baffle is recorded as 19% at the entrance and 30% along the length of 18mm downstream, while the mixing efficiency for micromixer with baffles at the same condition is recorded as 21% in the inlet-structure, and 71% at the outlet (Fig. 9, Fig. 10 and Table 1).

It is seen that the mixing is improved because the baffles help increase the contacting areas for fluid streams. Moreover from Fig. 11, we see that it is likely to generate a bubble at the corner of the channel during the mixing experiment. Such a rare phenomenon is found due to the use of special material and fabrication process. However, we still point out that the most advantage for tape-glass microchannel is that it is easy to fabricate, fast-adapting and cost-saving for lab procedure, and convenient for quick integration of chip.

With careful investigation in the process, the tape-glass microchannel is as hydrophilic stable as the JSR-glass, PMMA or PDMS microchannels. This shows that the tape-glass structure can easily achieve a long term capillary-driven characteristic as other materials.

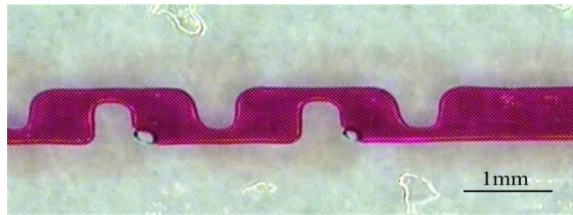


Figure 11. The air bubble in the OCA tape-glass microchannel.

We also test and compare the capillary flow in straight PDMS microchannels using conventional photolithography, molding and oxygen plasma bonding. These PDMS materials were stored at different storing times after fabrication, namely 12 min, 25min and 50min and flow were tested out with DI water and is shown in Fig. 12. It is seen that PDMS microchannel of storing time of 12 min can have the meniscus interface move down the channel at an elapsed time of 4.6 sec. For PDMS of storing time of 25 min, the flow time will increase with decreasing moving velocity. The lowest moving velocity of meniscus interface was observed at the storing time of 50 min, which takes around 18 sec to run through the channel. Experimental results show that traditional PDMS chip is easily affected by the storing time of the finished work, which not only destroys the hydrophilic feature but also suffers inefficient fabrication process.

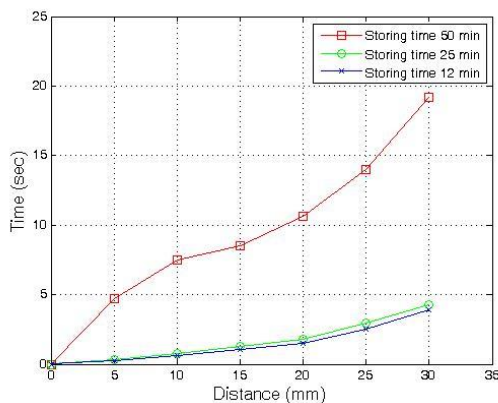


Figure 12. Relationship between the fluid traveling time and distance of PDMS channel at different storing time.

By comparison, the same capillary-driven tests of fluids were carried out on straight tape-glass channels. Fig. 13 recorded the test results of the OCA tape-glass microchannels at different storing time. It is shown that at storing time of 0 day, the meniscus interface moves downstream to the channel at an elapsed time of 3.6 sec, while for the tape-glass of storing time of 45 days takes the elapsed time as same as those above. This shows that our finished work is made from intrinsic hydrophilic materials.

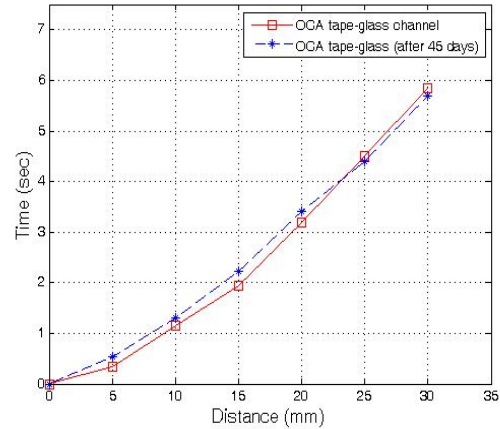


Figure 13. Relationship between the fluid traveling time and distance of OCA tape-glass channel at different storing time.

the present paper addresses the fabrication method of glass-tape chip with baffle structures installed so as to bring an interesting experiment for the capillary-driven micromixer. Here two fluids of ethanol marked by 5 wt% deep blue ink (Quink Co.) and DI water were used to demonstrate the fluid mixing results. The baffle structure indeed helps improve the mixing results at the exit of the downstream area.

The related data regarding the mixing performance are recorded in Table 1 where we have listed the mixing efficiency for tape-glass micromixer. From the results we see the mixing efficiency at entrance of baffled structure is only 21% while 71% is obtained at exit of the baffled structure. We conclude that the mixing results of tape-glass microchannel is improved due to its implemented baffle structure and easy fabrication, cost-saving process compared to the PMMA chips [14, 15, 16, 17] and PDMS chips [18, 19]. Here we point out that smaller baffle spaces will also increase the interfacial contact areas and decrease the diffusive distances in length.

Table 1. Mixing efficiency test for OCA double-sided adhesive tape at inlet- and outlet-structures

Baffle/Mixing	Inlet-structure	Outlet-structure
No Baffles	19%	30%
Baffle structures	21%	71%

5. Conclusion

The tape-glass microchannel is simple and easy in fabrication and takes the advantages of cost-saving feature in the procedure. The mixing result (71%) is acceptable when considering the efficiency of chip manufacturing.

We also compare the capillary tape-glass chip with conventional PDMS microchannel to obtain a relatively acceptable mixing efficiency and performance. We note that there are some reports for the applications of PDMS microchannels but the introduction of double-sided cohesive tape microchannel on glass is still of interest in the applications. In particular, we implemented a number of baffle structures in the channels and studied the mixing performance. Our experiment shows the idea of tape-glass hydrophilic structure not only simple in fabrication but also the cost-saving in product manufacturing. Our design of the chip with baffle gap of 90 μm and baffle space of 150 μm shows a well-established structure for effective mixing to reach 71% in gray level image analysis. The advantage of hydrophilic micromixer design in terms of the use of double-sided cohesive tape has its values in not only providing with an interesting idea of capillary micromixer but also emphasizing an important fabrication method in Engineering apart from the widely-adopted PDMS hydrophilic chips. Our experiment shows that the double-sided tape-glass micromixer with baffle structure is very suitable in generating capillary flows and for achieving good mixing results.

References

- [1] N. Giordano, J.T. Cheng, "Microfluid mechanics: progress and opportunities". *J. Phys. Condens. Matter*, Vol. 13 (2001) No. 2, pp. 271-295.
- [2] N.T. Nguyen, Z. Wu, "Micromixers-a review". *J. Micromech. Microeng.*, Vol. 15 (2005) No. 3, pp. 1-16.
- [3] V. Vivek, Y. Zeng, E.S. Kim, "Novel acoustic-wave micromixer". *Proceedings of the IEEE Micro Electro Mechanical Systems (MEMS)*, Vol. 2 (2000) No. 8, pp. 668-673, 2000.
- [4] H.H. Bau, J. Zhong, M. Yi, "A minute magneto hydro dynamic (MHD) mixer". *Sens. Actuators B: Chem.*, Vol. 79 (2001) No. 3, pp. 207-215.
- [5] A.D. Stroock, S.K.W. Dertinger, A. Ajdari, I. Mezic, H.A. Stone, G.M. Whitesides, "Chaotic mixer for microchannels". *Science*, Vol. 295 (2002) No. 3, pp. 647-651.
- [6] S.H. Wong, P. Bryant, M. Ward, C. Wharton, "Investigation of mixing in a cross-shaped micromixer with static mixing elements for reaction kinetics studies." *Sens Actuators B*, Vol. 95 (2003) No. 4, pp. 414-424.
- [7] N. Schwesinger, T. Frank, H. Wurmus, "A modular microfluid system with an integrated micromixer". *J. Micromech. Microeng.*, Vol. 6 (1996) No. 7, pp. 99-102.
- [8] J. Melin, G. Gimenez, N. Roxhed, W. van der Wijngaart, G. Stemme, "A fast passive and planar liquid sample micromixer." *Lab Chip*, Vol. 4 (2004), No. 4, pp. 214-219.
- [9] D.J. Laser, J.G. Santiago, "A review of micropumps." *J. Micromech. Microeng.*, Vol. 14 (2004) No. 5, pp. 35-64.
- [10] L.X. Chen, S.Y. Lee, J.B. Choo, E.K. Lee, "Continuous dynamic flow micropumps for microfluid manipulation." *J. Micromech. Microeng.*, Vol. 18 (2008) No. 7, pp. 013001.
- [11] L.X. Chen, G.Q. Wang, C.S. Lim, G.H. Seong, J.B. Choo, E.K. Lee, S.H. Kang, J.M. Song, "Evaluation of passive mixing behaviors in a pillar obstruction poly(dimethylsiloxane) microfluidic mixer using fluorescence microscopy". *Microfluidics and Nanofluidics*, Vol. 7 (2009) No. 6, pp. 267-273.
- [12] C. Choi, M.H. Kim, "The fabrication of a single glass microchannel to study the hydrophobicity effect on two-phase flow boiling of water." *J. Micromech. Microeng.*, Vol. 18 (2008) No. 13, pp. 105016-105034.
- [13] L.M. Strambini, M. Piotto, A. Nannini, "Glass microchannel technology for capillary electrophoresis." *International Journal of Environmental and Analytical Chemistry*, Vol. 85 (2005) No. 8, pp. 681-686.
- [14] Bubendorfer, X. Lui, A. Ellis, "Microfabrication of PDMS microchannels using SU-8/PMMA moldings and their sealing to polystyrene substrate." *Smart Mater. Struct.*, Vol. 16 (2007) No. 9, pp. 367-371.
- [15] M. Zimmermann, P. Hunziker, E. Delamarche, "Valves for autonomous capillary systems." *Microfluid. Nanofluid.*, Vol. 5 (2008) No. 6, pp. 395-402.
- [16] G.J. Wang, Y.F. Hsu, S.H. Hsu, R.H. Horng, "JSR photolithography based microvessel scaffold fabrication and cell seeding". *Biomed Microdevices*, Vol. 8 (2006) No. 9, pp. 17-23.
- [17] G.J. Wang, K.H. Ho, S.H. Hsu, K.P. Wang, "Microvessel scaffold with circular microchannels by photoresist melting." *Biomed Microdevices*, Vol. 9 (2007) No. 9, pp. 657-663.
- [18] A.A.S. Bhagat, E.T.K. Peterson, I. Papautsky, "A passive planar micromixer with obstructions for mixing at low Reynolds numbers." *J. Micromech. Microeng.*, Vol. 17 (2007) No. 7, pp. 1017-1024.
- [19] C.F. Chen, C.F. Kung, H.C. Chen, C.C. Chu, C.C. Chang and F.G. Tseng, "A microfluidic nanoliter mixer with optimized grooved structures driven by capillary pumping". *J. Micromech. Microeng.*, Vol. 16 (2006) No. 9, pp. 1358-1365.
- [20] I.D. Yang, Y.F. Chen, F.G. Tseng, H.T. Hsu, C.C. Chieng, "Surface tension driven and 3-D vortex enhanced rapid mixing microchamber". *J. Microelectromech. Syst.*, Vol. 15 (2006) No. 4, pp. 659-670.
- [21] S. Bouaidat, O. Hansen, H. Bruus, C. Berendsen, N.K.B. Madsen, P. Thomsen, A. Wolff, J. Jonsmann, "Surface-directed capillary system; theory, experiments and applications". *Lab Chip*, Vol. 5 (2005) No. 1, pp. 827-836.
- [22] D. Snakenborg, H. Klank and J.P. Kutter, "Microstructure fabrication with a CO₂ laser system". *J. Micromech. Microeng.*, Vol. 14 (2004) No. 3, pp. 182-187.
- [23] W.R. Jong, T.H. Kuo, S.W. Ho, H.H. Chiu, S.H. Peng, "Flows in rectangular microchannels driven by capillary force and gravity." *Int. Commun. Heat Mass Transf.*, Vol. 34 (2007) No. 7, pp. 186-196.
- [24] Y.C. Lin, Y.C. Chung, C.Y. Wu, "Mixing enhancement of the passive microfluidic mixer with J-shaped baffles in the tee channel". *Biomed. Microdev.*, Vol. 9 (2007) No. 7, pp. 215-221.
- [25] M. Zimmerman, H. Schmid, P. Hunziker, E. Delamarche, "Capillary pumps for autonomous capillary systems". *Lab Chip*, Vol. 7 (2007) No. 3, pp. 119-125.
- [26] S.W. Lee, D.S. Kim, S.S. Lee, T.H. Kwon, "A split and recombination micromixer fabricated in a PDMS three-dimensional structure". *J. Micromech. Microeng.*, Vol. 16 (2006) No. 5, pp. 1067-1072.



الجامعة الهاشمية



المملكة الأردنية الهاشمية

المجلة الأردنية
للمهندسة الميكانيكية والصناعية

JJIMOE

مجلة علمية عالمية محكمة
تصدر بدعم من صندوق البحث العلمي

<http://jjmie.hu.edu.jo/>

ISSN 1995-6665

المجلة الأردنية للهندسة الميكانيكية والصناعية

مجلة علمية عالمية محكمة

المجلة الأردنية للهندسة الميكانيكية والصناعية: مجلة علمية عالمية محكمة تصدر عن
الجامعة الهاشمية بالتعاون مع صندوق دعم البحث العلمي في الأردن

هيئة التحرير

رئيس التحرير

الأستاذ الدكتور أحمد الغندور.

قسم الهندسة الميكانيكية و الصناعية، الجامعة الهاشمية، الزرقاء، الأردن.

الأعضاء

الأستاذ الدكتور ناصر الحنيطي

الجامعة الاردنية

الأستاذ الدكتور محمد أحمد حمدان

الجامعة الاردنية

الأستاذ الدكتور محمد هياجنه.

جامعة العلوم والتكنولوجيا الاردنية

الاستاذ الدكتور نسيم سواقد.

جامعة مؤتة

الاستاذ الدكتور سهيل كيوان

جامعة العلوم والتكنولوجيا الاردنية

الاستاذ الدكتور أمين الريبيدي.

جامعة البلقاء التطبيقية

فريق الدعم

تنفيذ وإخراج

م . علي أبو سليمة

المحرر اللغوي

الدكتور قصي الذبيان

ترسل البحوث إلى العنوان التالي

رئيس تحرير المجلة الأردنية للهندسة الميكانيكية والصناعية

الجامعة الهاشمية

كلية الهندسة

قسم الهندسة الميكانيكية

الزرقاء - الأردن

هاتف : 00962 5 3903333 فرعي 4537

Email: jjmie@hu.edu.jo

Website: www.jjmie.hu.edu.jo